ISSN No. 0737-5352-14

MICROWAVE REMOTE SENSING OF LIQUID WATER AND SURFACE EMITTANCE OVER LAND REGIONS

Andrew S. Jones
Thomas H. Vonder Haar

Research Supported by U.S. Army Research Office under Grant No. DAAL03-86-G-0190

CIRA Cooperative Institute for Research in the Atmosphere

U.S. Army Center for Geosciences

Colorado State University

MICROWAVE REMOTE SENSING OF CLOUD LIQUID WATER AND SURFACE EMITTANCE OVER LAND REGIONS

by

Andrew S. Jones

Department of Atmospheric Sciences
Colorado State University
Fort Collins, Colorado 80525

This research was supported by ARO
under Grant No. DAAL03-86-G-0190 through the
U.S. Army Center for Geosciences and CIRA

January 1989

From a thesis submitted to the Academic Faculty of Colorado State University in partial fulfillment of the requirements for the degree of Master of Science.

ABSTRACT

MICROWAVE REMOTE SENSING OF CLOUD LIQUID WATER AND SURFACE EMITTANCE OVER LAND REGIONS

Microwave remote sensing of cloud liquid water has largely been limited to areas over ocean surfaces. This study uses data from a new microwave instrument, the SSM/I on a polar-orbiting DMSP satellite, and infrared and visible data from the VISSR instrument on the GOES satellite in geostationary orbit. The region selected for the study was an area of 500 km $\times$ 500 km centered on northeast Colorado during the first week of August 1987. The SSM/I instrument has new high frequency channels (85.5 GHz) which are more strongly attenuated by cloud liquid water than channels on previous instruments. This allows for the estimation of integrated cloud liquid water based on the microwave brightness temperature depression caused by attenuation and emission of microwave radiation at the colder cloud levels. Atmospheric attenuation due to oxygen and water vapor is determined using a millimeter-wave propagation model (MPM). The Rayleigh approximation is used for the calculation of cloud liquid water attenuation.

Surface emittance measurements at the SSM/I frequencies were made with the aid of co-located GOES infrared data during clear sky conditions. Images produced of the retrieved surface emittances suggest a strong influence by wet surfaces caused by precipitation and irrigation. Error analysis results indicate absolute errors of ± 0.012 for surface emittance retrievals for the 85.5 GHz channels.

Integrated cloud liquid water retrievals show good qualitative agreement with other available data sources. Numerical error sensitivity analysis and comparison of integrated cloud liquid water retrievals for the vertical and horizontal polarizations show error estimates of 0.15 kg$\cdot$m^{-2} including instrument noise. A bias between the horizontal and

vertical polarizations of the 85.5 GHz channels was noticed in the retrieved integrated cloud liquid water amounts. The bias appears to be due to a relative instrument error between channels of approximately 1.5 K. Absolute error estimates of the integrated cloud liquid water retrievals are unavailable but calibration of the method should be possible if quantitative integrated cloud liquid water amounts are known.

Andrew S. Jones
Department of Atmospheric Sciences
Colorado State University
Fort Collins, Colorado 80523
Fall 1988

ACKNOWLEDGEMENTS

I would like to thank my advisor, Dr. Thomas Vonder Haar, for his direction and support during this study. Thanks also go to committee members Dr. Stephen Cox and Dr. Chiao-Yao She for their involvement with this work.

This work was done during my stay as a Fellow at the CSU U.S. Army Center for Geosciences. I can not over state the pleasure it has been to work in such an environment. The Geoscience Center, CIRA, and the NOAA/RAMM Branch at CSU provided numerous interchanges with other students, faculty, and researchers who offered suggestions for this work. I hope that my future involvement with the Geoscience Center will continue to be as fruitful.

There are many people to whom I am deeply indebted to for their suggestions and help with this work. Don Hillger and Alan Lipton are what one could say were my mentors on the many applications of satellite data. Alan Lipton introduced me to the VAX computer systems here at CSU/CIRA and to my first encounter with VAS sounding data. Don Hillger and I worked on a project which involved VAS data which was presented at the Third Satellite Conference in Anahiem, California and was the source of many learning experiences. Bob Green, who is now affiliated with UCAR in Boulder, Colorado introduced me to the world of computer manipulation of satellite imagery. The help of Don Reinke and Ed Tomlinson from the Geoscience Center in finding the SSM/I data and other support was invaluable to this study. Discussions with Moti Segal and his help in providing the irrigation information were also of great help. Help with the FIRE data sets was provided by Kelly Dean and Garrett Campbell, among other programing help. The help of Dave Randel, Laura Smith, Nan McClurg, Frank Evans and many others for numerous problems I have encountered, software and otherwise, during this research is deeply appreciated.

Special thanks go to Dr. Hans Liebe at ITS in Boulder, Colorado who's Millimeter-wave Propagation Model was used extensively in this study, and to Dr. Richard Savage at Hughes Aircraft Company in Denver, Colorado for his help in supplying the essential SSM/I data for this study. The CINDE CLASS soundings used were provided by Charles Wade and Sandra Henry from NCAR in Boulder, Colorado.

Thanks go to Don Hillger for his helpful review of this paper and to Judy Dunn for her expert drawing of the many figures in this paper. Thanks also go to Loretta Wilson for her help in preparing this report. The computer calculations were performed using the CIRA LAN research facilities.

This work was supported by the U.S. Army Center for the Geosciences under ARO grant DAAL03-86-G-0190.

TABLE OF CONTENTS

LIST OF FIGURES

LIST OF TABLES

Chapter 1

INTRODUCTION

The retrieval of cloud liquid water using passive microwave radiometry is a useful meteorological tool. Present satellite liquid water retrieval capabilities are largely limited to areas over ocean surfaces, but with the new Special Sensor Microwave/Imager (SSM/I) instrument retrieval of liquid water in non-precipitating clouds over land surfaces is feasible. The high frequency SSM/I channels at 85.5 GHz are more sensitive to cloud liquid water than channels on previous instruments. The apparent variability of land surface effects is reduced due to the attenuating effects of the clouds, and by using co-located infrared data the surface emittance can be estimated for clear sky conditions before clouds appear.

This chapter provides an overview of cloud liquid water in the atmosphere and a brief discussion of the influence of cloud liquid water on general weather conditions. A short historical background on previous microwave remote sensing of cloud liquid water is also provided. A section at the end of this chapter summarizes the goals of this study in relation to previous work.

1.1 CLOUD LIQUID WATER

Particular cloud types have characteristic droplet size distributions which have a range of possible variations. Fair-weather cumulus clouds have a mean droplet radius ranging from 2 to 7 μm, and cumulonimbus have particle sizes from 1 to 100 μm. At 100 μm the distinction between cloud particles and suspended rain becomes less clear. Typical cloud liquid water contents range from 0.1 to 1.0 $g{\cdot}m^{-3}$. Higher liquid water contents up to 10 $g{\cdot}m^{-3}$ have been reported for cumulus type clouds with large vertical development (Valley, 1965). Vertical development of typical stratus and fair-weather clouds is about 0.5 to 2.0 km, while cumulus clouds with large vertical development can reach heights

Table 1.1

Table 1.1: Typical cloud characteristics (adapted from Rodgers, 1979; and Slobin, 1982).

Cloud type	Droplet number density (cm^{-3})	Mean droplet radius (μm)	Liquid water content* ($g{\cdot}m^{-3}$)
(from Rodgers, 1979)			
Hawaiian Orographic	10	20	0.50
Maritime Cumulus	50	15	0.50
Continental Cumulus	200	5	0.3-3.0
(from Slobin, 1982)			
Fair-weather cumulus	300	5	0.15
Stratocumulus	350	5	0.16
Stratus I	464	5	0.27
Altostratus	450	6	0.46
Stratus II	260	7	0.49
Cumulus congestus	207	9	0.67
Cumulonimbus	72	15	0.98
Nimbostratus	330	9	0.99

* These figures are quite variable, depending upon the extent of cloud development.

of 7 to 10 km. A brief summary of selected cloud types and their relevant characteristic parameters from Carrier *et al.* (1967) and Fletcher (1963) (adapted from Rodgers, 1979; and Slobin, 1982) are listed in Table 1.1. Additional cloud models of droplet distribution which can be related to cloud liquid water content are available from Fraser *et al.*, (1975). The droplet distributions are analytically represented using a modified gamma distribution approximation (Deirmendjian, 1969). Further discussion of model droplet distributions is not warranted since in Chapter 2 it will be shown that in the Rayleigh limit microwave attenuation is independent of the droplet size distribution.

The vertical distribution of cloud water content can vary considerably over a short distance, but typically increases with height above the cloud base, reaches a maximum in the upper half of the cloud and then decreases toward the cloud top, as shown in Figure 1.1 (Warner, 1955). The higher amounts of cloud liquid water are more closely correlated to the locations of largest drop sizes rather than largest droplet concentrations in a cloud (Pruppacher and Klett, 1980).

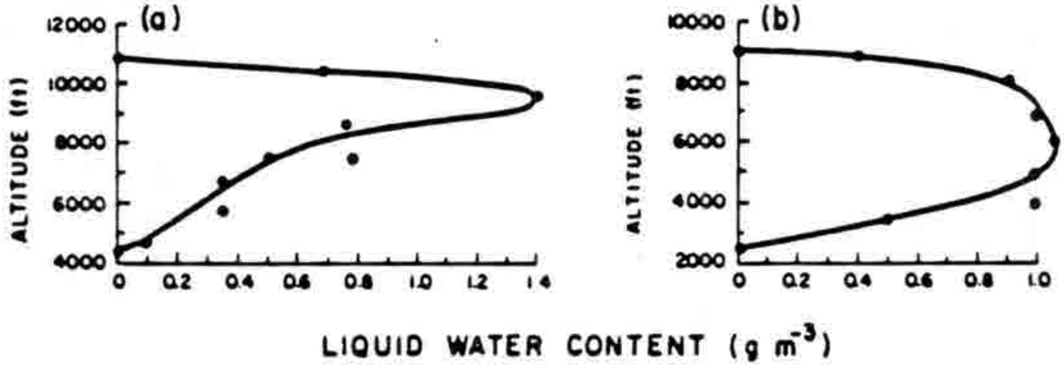

Figure 1.1: Examples of the vertical distribution of cloud liquid water in cumulus clouds (from Warner, 1955).

1.1.1 The Amount of Cloud Liquid Water Relative to Water Vapor in the Atmosphere

In an atmospheric column, the integrated cloud liquid water can be approximately a third of the column's total water. A simple calculation can be made to show this point. The water vapor density of the 1962 Standard Atmosphere (Valley, 1965) can be represented by,

$$\rho_v(z) = \rho_0 e^{-z/H} \mathrm{g{\cdot}m^{-3}}, \tag{1.1}$$

where H = 2 km, $\rho_0 = 7.72$ g·m^{-3}. The total integrated water vapor is then,

$$IWV = \int_0^\infty \rho_0 e^{-z/H} dz = \rho_0 H = 15.44 \text{ kg{\cdot}m}^{-2}. \tag{1.2}$$

For a cloud with a height of 5 km and a typical cumulus cloud liquid water content of 1.0 g·m^{-3} from Table 1.1, the total integrated cloud liquid water in the atmospheric column would be 5 kg·m^{-2} which is only a third of the column's integrated water vapor content.

1.1.2 Large Scale Variability of Liquid Water and Water Vapor

The variability of the atmosphere's total water is heavily influenced by the cloud liquid water content. A study of global water vapor and liquid water amounts over the earth's oceans by Prabhakara *et al.* (1983) confirmed that water vapor is the primary component in the atmosphere, but that liquid water, which has a much smaller spatial scale, contributes the most to the variability of the total water content in the atmosphere. By using the low frequency channels (6.6 GHz, and 10.7 GHz) on the Nimbus 7 Scanning Multichannel Microwave Radiometer (SMMR), the liquid water amounts retrieved also include precipitation-sized droplets since the Rayleigh approximation is valid for rain drops having a mode radius of 400 μm or smaller at those frequencies (Tsang *et al.*, 1977). A statistical examination of the SMMR vertical polarization data from the period 25 October - 25 November 1978 by latitudinal mean and standard deviation over the oceans produced the results shown in Figure 1.2. The mean brightness temperature, $\overline{T}_B$, for several latitudes in Figure 1.2 indicate that more moist conditions due to water vapor existed at the Intertropical Convergence Zone (ITCZ) at 7° N. Liquid water due to clouds and precipitation does not seem to influence $\overline{T}_B$ with latitude as much as the water vapor in the atmosphere. The standard deviation has largest values at 42° N which lies in the active baroclinic zone of the midlatitudes. A displacement of the standard deviation maximum with instrument frequency at 7° N is from a saturation effect produced when liquid water in the atmosphere exceeds approximately 0.4 kg·m^{-2} (Prabhakara *et al.*, 1982). The high variability at 42° N is due to the smaller spatial and temporal scales of liquid water associated with the baroclinic activity.

Practical climatological use of the SMMR data was made by Prabhakara *et al.* (1986) who derived maps of global liquid water content over ocean surfaces for the winter and summer seasons (see Figure 1.3) and related the derived liquid water content to the global precipitation distribution based on the Marshall-Palmer (1948) equation which relates droplet size to rainfall intensity. Monthly mean precipitation amounts were derived for a five year period (1979-83) which included an El Niño event. The retrieved liquid water showed an area in the equatorial western Pacific Ocean where a strong reversal of the mean pattern was associated with the El Niño. Anomalies due to the El Niño were also noticed in the SMMR derived water vapor fields over the same time period (Prabhakara, 1985).

1.1.3 Synoptic Scale Liquid Water Variability

The structure and evolution of liquid water fields were shown to be highly variable in a wintertime case study by Rauber and Grant (1986), and Rauber *et al.* (1986) over the northern Colorado Rocky Mountains. Several relationships of liquid water to several meteorological parameters for prefrontal cloud systems were noticed. Those relationships were: precipitation and liquid water content were inversely related; the highest liquid water values occurred when the cloud tops were warm and precipitation rates were low; and the clouds over the mountain slopes had consistently higher liquid water contents. The observations used in Rauber and Grant (1986) and Rauber *et al.* (1986) were made with a combination of aircraft and ground-based microwave radiometers.

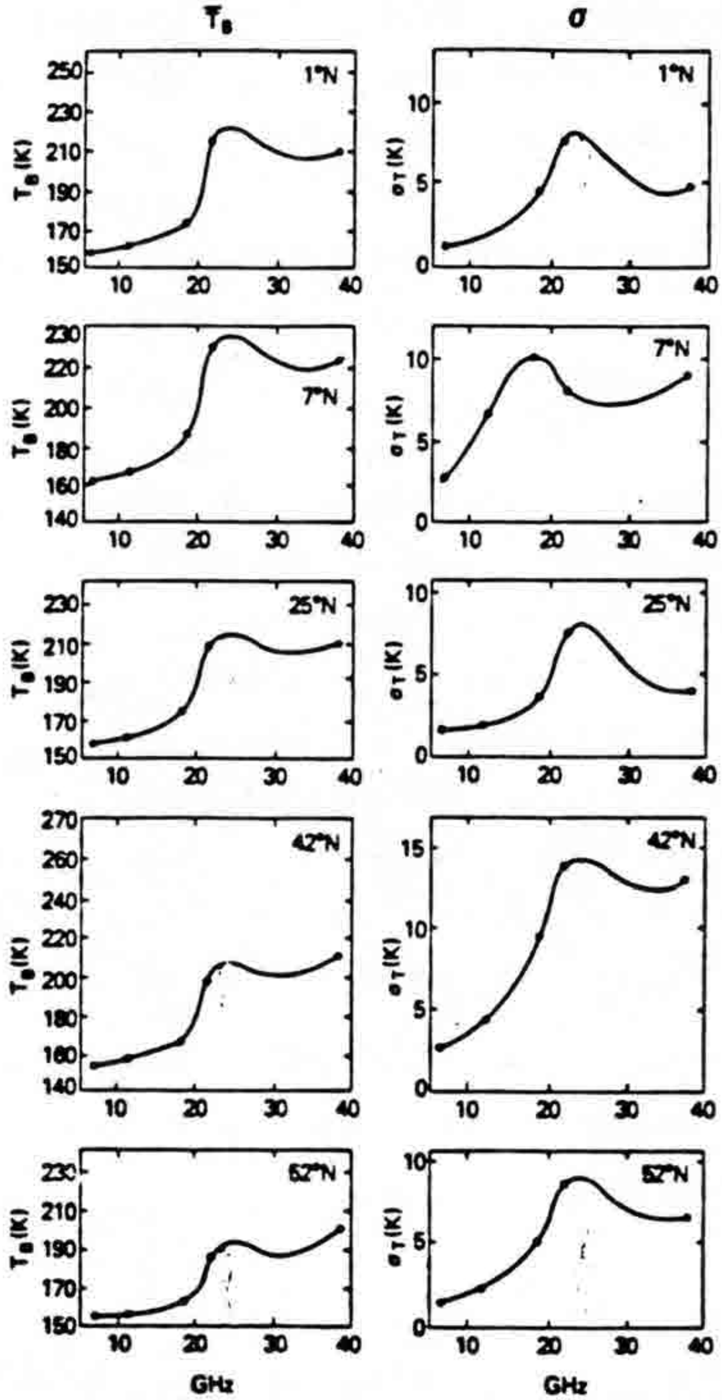

Figure 1.2: Zonal mean $\overline{T}_B$ and standard deviation σ of the microwave brightness temperature measured by Nimbus 7 SMMR in the vertical polarization for 25 Oct - 25 Nov 1978 (from Prabhakara *et al.*, 1983).

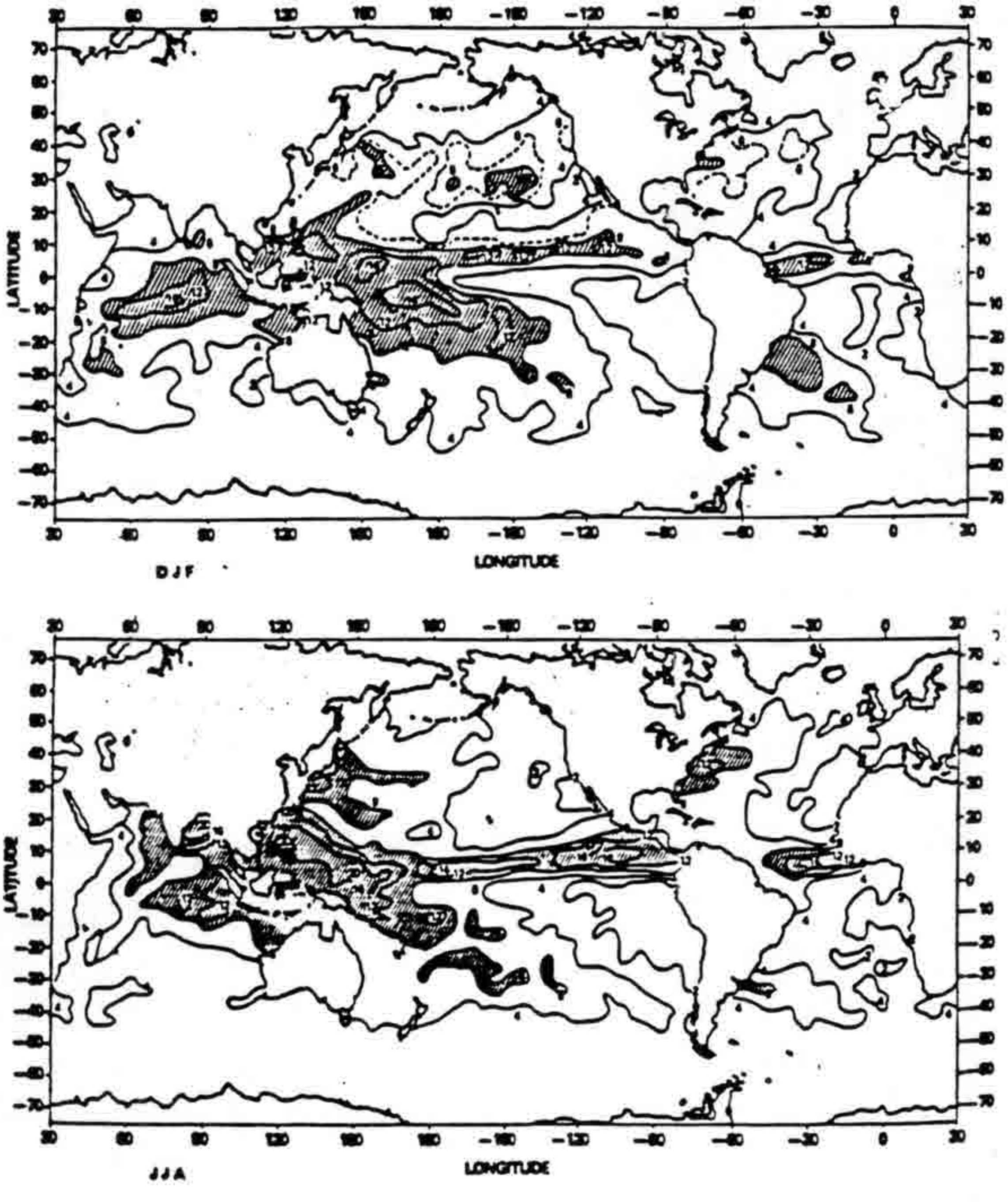

Figure 1.3: Global mean liquid water content distribution in the atmosphere (10^{-2} kg·m^{-2}) over the oceans during (a) Dec, Jan, and Feb; (b) Jun, Jul, and Aug, derived from SMMR data for 1979-81 (from Prabhakara, 1986).

1.2 MICROWAVE REMOTE SENSING BACKGROUND

Satellite-based remote sensing has had a short history in comparison to many other areas of atmospheric science. The use of earth-orbiting microwave radiometers for remote sensing began in 1968 with Cosmos 243 which was launched by the USSR and began a series of space-based microwave sensors (Njoku, 1982). The ability of the early low frequency (< 40 GHz) microwave sensors to "see through" clouds was a significant result with many applications to remote sensing techniques which were unable to function in a cloudy environment. Since the earlier generations of satellite microwave sensors, a wider range of frequency bands have been explored with many new opportunities resulting for remote sensing applications. Geophysical parameters which can be remotely sensed from space are liquid water, water vapor, temperature, sea surface winds, sea ice, and soil moisture among many others.

Meeks and Lilley (1963) were first to suggest the possibility of remotely sensing the atmosphere using the microwave spectrum of oxygen. A technique was soon developed by Westwater (1965) for determining the temperature profile of the atmosphere by inverting the microwave brightness temperatures. Determination of integrated precipitable water vapor and integrated liquid water of non-precipitating clouds using ground-based radiometers came later with work by Gorelik *et al.* (1973), Westwater (1978), and others. Ground-based microwave radiometer measurements have been used to interpret the physical processes in wintertime cloud systems (Heggli, 1985; Rauber *et al.*, 1986) and have shown the need for estimates of liquid water in developing systems for a deeper understanding of the meteorological processes which interact with the liquid water. The next major advance was in satellite-based remote sensing in which Grody (1976), Staelin *et al.* (1976), and Wilheit *et al.* (1977) among others developed methods to retrieve water vapor and liquid water over ocean surfaces using theoretical-empirical approaches.

1.3 CLOUD LIQUID WATER RETRIEVAL METHODS

Several established methods have been used to sense cloud liquid water in the atmosphere using passive microwave remote sensing techniques. The methods can be separated into ground-based and satellite-based methods. The ground-based systems have the advantage of not having to view a variable surface background which complicates the retrieval process, while satellite-based systems are capable of measuring the horizontal distribution of cloud liquid water over a large area. The satellite-based methods are further subdivided into retrievals over land and ocean surfaces due to the distinct radiometric differences of the surface layers. The ocean surfaces are radiatively cold in the microwave regions due to water's low surface emittance. When cloud liquid water is detected in the atmosphere the microwave instrument senses higher brightness temperatures for thin clouds due to the absorption and emission of microwave radiation by liquid water at a higher emittance, thus clouds appear warm over the ocean, but as the amount of cloud liquid water increases the microwaves originate primarily from the higher levels of the cloud and the brightness temperature decreases as shown by Tsang *et al.* (1977) in Figure 1.4. Over land surfaces, the surface emittance is relatively high which decreases the sensitivity of the instrument to cloud liquid water since the cloud emits radiation at nearly the same brightness temperature as the surface.

1.3.1 Ground-based Cloud Liquid Water Retrieval

Ground-based measurements of integrated water vapor and cloud liquid water are made with multichannel microwave radiometers which determine the brightness temperatures emitted by water vapor and cloud liquid water in the atmosphere. The radiometer typically has a lower frequency near the water vapor absorption line at 22.235 GHz and a higher frequency in the 30-40 GHz window region for determination of cloud liquid water. Path-integrated amounts of water vapor and cloud liquid water are calculated from the radiometer measurements of brightness temperature using statistical retrieval methods which reduce the brightness temperature variations to a linear function of integrated water vapor and cloud liquid water (Hogg *et al.*, 1983).

Field evaluations have been made of current ground-based microwave radiometers by several authors (Westwater, 1978; Heggli *et al.*, 1987). Water vapor retrievals showed root-mean-square (rms) errors of 0.7 kg·m^{-2}, but another study (Hogg *et al.*, 1983) had

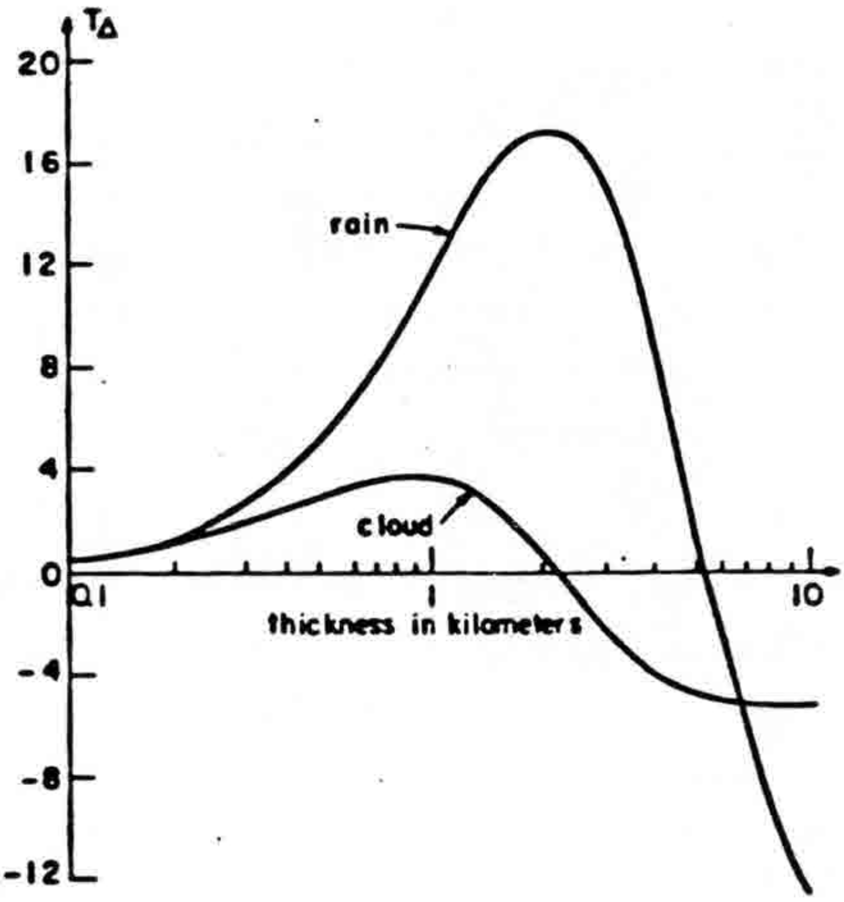

Figure 1.4: Brightening and darkening effects as a function of cloud thickness over an ocean surface at 94 GHz (from Tsang *et al.*, 1977).

rms differences of 1.7 kg·m^{-2} and 2.6 kg·m^{-2} for two separate case studies which was attributed to variability in the radiosonde measurements. These errors are similar to results reported by Guiraud *et al.* (1979), Elgered *et al.* (1982) and Gaikovich *et al.* (1983).

Liquid water retrieval accuracy is much more difficult to determine since radiosondes do not record such information. Comparisons have been made by Snider *et al.* (1980a, 1980b) which used the 28 GHz signal from the COMSTAR-3 satellite to measure the cloud optical depth directly and was compared to the ground-based radiometer brightness temperature fluctuations which are used to derive the liquid water content. Comparisons of data from the satellite attenuation measurements and the dual-channel ground-based radiometer were quite good but allowed no quantitative estimate of liquid water retrieval accuracy. Aircraft are generally used for crude comparisons but due to spatial and temporal sampling difficulties the comparison of radiometer derived data with aircraft data is not an easy process (Heggli and Reynolds , 1985).

1.3.2 Satellite-based Cloud Liquid Water Retrieval

An infrared method to retrieve ice and liquid water content using Nimbus 6 High-resolution Infrared Sounder (HIRS) data has been developed by Feddes and Liou (1978) which is based on a number of theoretical radiance calculations which are then parameterized so that an empirical method to determine cloud type and ice and water content is possible. Disadvantages of this technique are the opacity of water clouds in the infrared spectrum, and the sensitivity to cloud temperature, however, the spatial resolution of the infrared data is generally much higher than the microwave data and surface conditions are less important.

The microwave cloud liquid water retrieval methods are sensitive to the surface conditions of the earth. Assuming a relatively transparent atmosphere at microwave wavelengths such that the atmosphere can be assumed to be isothermal allows the estimation of the apparent microwave brightness temperature given by (Grody, 1976),

$$T_B = T_s[1 - (1 - \epsilon_\nu)\tau_\nu^2], \tag{1.3}$$

where T_s is the surface skin temperature, ϵ_ν is the surface emittance and τ_ν is the atmospheric transmittance for frequency ν. A similar form of Equation 1.3 was derived by Chang and Wilheit (1979). Chapter 2 contains a more complete discussion of microwave radiative transfer. The sensitivity of T_B from Equation 1.3 is,

$$\frac{\partial T_B}{\partial \tau_\nu} = -2T_s(1-\epsilon_\nu)\tau_\nu, \tag{1.4}$$

which is proportional to $(1-\epsilon_\nu)$. This means that for high emittance values close to unity (such as land surface values) that the microwave radiometer is insensitive to cloud liquid water content variations. Remote sensing of cloud liquid water over ocean surfaces is more feasible because water has a surface emittance of about 0.5. Early attempts to provide estimates of integrated water vapor and cloud liquid water from satellite measurements were made by Soviet scientists using data from the Cosmos 243 and Cosmos 384 (Gurvich *et al.*, 1970). More complete data sets from the Nimbus E Microwave Spectrometer (NEMS) and the Electronically Scanning Microwave Radiometer (ESMR) on Nimbus 5 (launched in 1972) were used to retrieve integrated water vapor and cloud liquid water over ocean surfaces (Grody, 1976; Staelin *et al.*, 1976; Chang and Wilheit, 1979). The Scanning Microwave Spectrometer (SCAMS) on Nimbus 6 (launched in 1975) was able to provide spatial coverage due to its scanning capabilities. Integrated water vapor retrievals over ocean surfaces by Grody *et al.* (1980) showed rms differences of 5.0 kg·m^{-2} which also includes errors due to the radiosonde instruments. Nimbus 7 (launched in 1978) carries the Scanning Multichannel Microwave Radiometer (SMMR) (SMMR was also onboard Seasat (1978) which became inactive after approximately 100 days) which is a conical scanning instrument with a fixed satellite zenith angle of 50° and has more channels than previous instruments. Retrieval accuracies of cloud liquid water and water vapor using SMMR data over ocean surfaces is approximately 0.045 kg·m^{-2} and 1.5 kg·m^{-2} respectively, based on simulated data (Wilheit and Chang, 1980). In the study by Prabhakara *et al.* (1983) mentioned in section 1.1.2 they conservatively estimated the liquid water retrieval accuracy to be approximately 0.1 kg·m^{-2}.

A empirical-theoretical method to determine liquid water content and water vapor amount over land surfaces using the Nimbus 6 SCAMS data is described by Liou and Duff

Table 1.2

Table 1.2: Prescribed surface emittance values used in Liou and Duff (1979).

Frequency (GHz)	Surface emittance dry	wet
22.235	0.95	0.93
31.4	0.96	0.94

(1979). A relatively simple approximation for the brightness temperature was used based on Grody (1976) which assumes that the clear column transmittance is near unity,

$$T_{B_\nu} \simeq \epsilon_\nu T_s + 2(1-\epsilon_\nu)T_s(Q/Q_0 + W/W_0), \tag{1.5}$$

where Q_0 and W_0 are constants, ϵ_ν is the surface emittance, T_s is the surface temperature, and Q and W are the total liquid water and water vapor amount. In their work the surface emittance was set at a predetermined value. Table 1.2 lists the surface emittances used for the dry and wet conditions for the SCAMS frequencies. Solving Equation 1.5 for Q and W yields,

$$Q = q_0 + q_1 T_{B_{\nu_1}} + q_2 T_{B_{\nu_2}} \tag{1.6}$$

$$W = w_0 + w_1 T_{B_{\nu_1}} + w_2 T_{B_{\nu_2}} \tag{1.7}$$

where $T_{B_{\nu_1}}$ and $T_{B_{\nu_2}}$ are brightness temperatures at 22.235 GHz and 31.4 GHz, and q_i and w_i $(i = 0, 1, 2)$ are coefficients which are determined empirically. Grody (1976) and Staelin *et al.* (1976) used the same method to determine water content over ocean surfaces using Nimbus 5 NEMS data. The statistical best fit is found for the coefficients for a number of simulated atmospheres and retrieval errors can be estimated from this fit (see Table 1.3). This method was compared to Feddes and Liou's (1979) infrared method and showed similar liquid water trends but the infrared method had consistently lower values of cloud liquid water. It was suggested that this was due to the microwave radiometer sensing the lower level cloud liquid water more effectively.

Table 1.3

Table 1.3: Estimated retrieval errors from Liou and Duff (1979).

	dry	wet
water vapor ($kg \cdot m^{-2}$)	8.7	9.7
liquid water ($kg \cdot m^{-2}$)	0.18	0.22

Another method by Yeh and Liou (1983) uses a combination of infrared and microwave channels to retrieve parameters such as cloud thickness, cloud top, cloud liquid water content, and surface emittance for a two layer cloud model using the Nimbus 6 HIRS and SCAMS instruments. A set of parameterized equations are developed based on a two layer cloud model which are then reduced to a set of polynomial equations using a group of model atmospheres for a statistical multiple regression analysis. Error sensitivity analysis over land with a surface emittance of 0.96, a cloud with an assumed liquid water content of 0.7 $kg \cdot m^{-2}$, and no instrument noise imposed retrieved a mean surface emittance of 0.97 ± 0.0043 and a cloud liquid water content of 0.76 ± 0.048 $kg \cdot m^{-2}$. Over estimation of the surface emittance directly affects the calculation of cloud liquid water. It was noticed that if the assumed surface emittance of 0.96 was used that the cloud liquid water content became 0.69 ± 0.035 $kg \cdot m^{-2}$ which is a much better value, but in doing so numerical stability was compromised for cases in which random noise was added. Cloud liquid water content results with random noise ranged from 0.76 to 1.0 $kg \cdot m^{-2}$.

1.4 RESEARCH OBJECTIVES

In the previous section it was noted that cloud liquid water retrieval over land is made more difficult due to the higher emittance of the land surface. In this study cloud liquid water will be retrieved over land from a space-borne instrument with careful analysis of the land surface emittance using co-located infrared data and the new 85.5 GHz channels of the SSM/I instrument. The retrieval method of Yeh and Liou (1983) showed how important an accurate estimate of the surface emittance is for cloud liquid water retrieval. By directly measuring the surface emittance in clear sky conditions before the clouds appear, the surface emittance variability problem in cloud liquid water retrieval should be minimized. An important aspect of the SSM/I instrument is that the 85.5 GHz channels are more sensitive to cloud liquid water than previously used microwave channels and surface effects become less important as the cloud liquid water increases and the atmospheric attenuation obscures the ground from view of the satellite-based sensor. The spatial resolution is also much better at the higher frequencies than previous microwave sensors. This allows for improved estimates of the horizontal variability of cloud liquid water.

Chapter 2

FUNDAMENTALS OF MICROWAVE REMOTE SENSING

The microwave region has many interesting and useful electromagnetic properties which are used for remote sensing. This chapter is a review of the basic fundamentals of passive microwave remote sensing. Section 2.1 introduces the radiative transfer equation and the various simplifying approximations used in the microwave region. The ability to use the Rayleigh approximation for non-precipitating clouds is of considerable importance to this work and is discussed in section 2.1.3. Properties of the atmosphere in the microwave region such as scattering and absorption are presented in section 2.2, and the final section, section 2.3, reviews microwave surface properties and how they influence microwave remote sensing.

2.1 MICROWAVE RADIATIVE TRANSFER THEORY

2.1.1 The Radiative Transfer Equation

The propagation of electromagnetic radiation through an atmosphere can be represented by the radiative transfer equation written in general form [1] (Chandrasekhar, 1960):

$$\frac{dL_\nu(\mathbf{r},\Omega_s)}{ds} = \sigma_e[J(\mathbf{r},\Omega_s) - L_\nu(\mathbf{r},\Omega_s)], \tag{2.1}$$

where $L_\nu(\mathbf{r},\Omega_s)$, is the spectral radiance at a frequency ν, and at a given location $\mathbf{r}$ in the direction Ω_s, σ_e is the atmospheric extinction coefficient, and $J(\mathbf{r},\Omega_s)$ is the total effective

[1] Symbols and units in this paper conform to recommended usage by the International Association of Meteorology and Atmospheric Physics (IAMAP) Radiation Commission (1978).

source function at $\mathbf{r}$ in the direction Ω_s. The extinction coefficient, σ_e, is defined as the sum of the absorption coefficient, σ_a, and the scattering coefficient, σ_s,

$$\sigma_e \equiv \sigma_a + \sigma_s, \tag{2.2}$$

with units of km^{-1}. Qualitatively, Equation 2.1 says that the rate of change of the radiance passing through the atmosphere at $\mathbf{r}$ in the direction Ω_s is composed of two terms, a source term due to thermal emission and scattering of radiation into the direction Ω_s, and an extinction term due to absorption and scattering of the radiation incident on the atmospheric volume.

The radiance measured by an earth-viewing satellite is found by integrating the radiative transfer equation over the total depth of the atmosphere. The solution of Equation 2.1 is facilitated by introducing the optical thickness,

$$\delta(s_1, s_2) = \int_{s_1}^{s_2} \sigma_e ds, \tag{2.3}$$

which is the integrated optical depth along a path s between two points s_1 and s_2. After multiplying Equation 2.1 by $e^{\delta(0,s')}$, where $s = 0$ is the surface boundary, and integrating, the formal solution of the radiative transfer equation along a path s is (Ulaby *et al.*, 1981):

$$L_\nu(s) = L_\nu(0)e^{-\delta(0,s)} + \int_0^s \sigma_e(s')J(s')e^{-\delta(s',s)}ds'. \tag{2.4}$$

The total effective source function including absorption and scattering effects is,

$$J(\mathbf{r}, \Omega_s) = (1 - \tilde{\omega})B_\nu[T(\mathbf{r})] + \frac{\tilde{\omega}}{4\pi}\int_0^{4\pi} \xi(\mathbf{r}, \Omega_i, \Omega_s)L_\nu(\mathbf{r}, \Omega_i)d\Omega_i, \tag{2.5}$$

where $B_\nu(T)$ is the Planck function for a temperature T, and $\tilde{\omega}$ is the single scatter albedo and is defined as,

$$\tilde{\omega} = \frac{\sigma_s}{\sigma_a + \sigma_s}. \tag{2.6}$$

The magnitude of $\tilde{\omega}$ determines whether absorption or scattering processes are dominant. $\xi(\mathbf{r}, \Omega_i, \Omega_s)$ is the scattering phase function which gives the probability at position $\mathbf{r}$ that energy incident from the direction Ω_i is scattered into the direction Ω_s.

2.1.2 Thermal Emission

In an atmosphere in local thermodynamic equilibrium Kirchoff's law says that the thermal emission must be equal to absorption, hence the source term due to the volume's thermal emission can be expressed as $\sigma_a B_\nu(T)$, where $B_\nu(T)$ is the Planck function. The Planck function,

$$B_\nu(T) = \frac{2h\nu^3}{c^2}(e^{h\nu/kT} - 1)^{-1}, \tag{2.7}$$

where $h = 6.63 \times 10^{-34}$ J·s is Planck's constant, $c = 3.0 \times 10^8$ m·s^{-1} the speed of light, $k = 1.38 \times 10^{-23}$ J·K^{-1} Boltzmann's constant, and T thermodynamic temperature, represents the spectral radiance an ideal blackbody would have as a function of frequency and temperature. A useful radiometric quantity associated with the Planck function is the equivalent brightness temperature,

$$T_B \equiv B^{-1}(L_\nu) = \frac{h\nu}{k}\left[\ln\left(1 + \frac{2h\nu^3}{L_\nu c^2}\right)\right]^{-1}, \tag{2.8}$$

which is defined as the temperature an ideal blackbody would have if it were emitting at a radiance L_ν. A common practice at this point in microwave regions is to approximate the Planck function using the Rayleigh-Jeans approximation,

$$B_\nu(T) = \frac{2\nu^2 kT}{c^2}, \tag{2.9}$$

which is valid for $h\nu/kT \ll 1$. However, for the SSM/I instrument to be used in this study the highest frequency is 85.5 GHz, and the approximation errors, ΔT_B, for a range of temperatures in Table 2.1 show unacceptable errors which are larger than the instrument accuracy of 1.5 K, therefore the full Planck function is used in preference over the Rayleigh-Jeans approximation.

2.1.3 The Rayleigh Approximation

Electromagnetic interaction with individual spherical particles is characterized by two quantities, a cross-section and an efficiency factor (Liou, 1980). The absorption cross-section, A_a, is defined as the ratio of the power absorbed by the particle, P_a, to the incident flux density, S_i,

$$A_a = \frac{P_a}{S_i}, \tag{2.10}$$

Table 2.1

Table 2.1: Rayleigh-Jeans approximation errors.

(ν = 85.5 GHz)				
T (K)	$T_{B_{exact}}$ (K)	$T_{B_{approx.}}$ (K)	ΔT_B (K)	error (%)
100	100	102.040	2.040	2.040
200	200	202.047	2.047	1.023
300	300	302.049	2.049	0.683

and has units of m^2. The absorption efficiency factor, Q_a, is the ratio of the absorption cross-section to the physical cross-section of the particle,

$$Q_a = \frac{A_a}{\pi r^2}, \tag{2.11}$$

where r is the radius of the particle. The scattering cross-section and efficiency factor are defined similarly,

$$A_s = \frac{P_s}{S_i}, \tag{2.12}$$

$$Q_s = \frac{A_s}{\pi r^2}. \tag{2.13}$$

From the law of conservation of energy, the extinction cross-section must be the sum of the absorption and scattering cross-sections,

$$A_e = A_a + A_s, \tag{2.14}$$

and therefore,

$$Q_e = Q_a + Q_s. \tag{2.15}$$

Scattering and absorption of electromagnetic waves by a dielectric spherical particle is solved by what is known as Mie theory (Mie, 1908) and is based on a size parameter,

$$\chi = \frac{2\pi r}{\lambda_b}, \tag{2.16}$$

where r is the particle radius and λ_b is the wavelength of the incident radiation in the background medium; and n, the ratio of the complex indices of refraction of the particle and the background medium,

$$n = \frac{n_p}{n_b}. \tag{2.17}$$

The scattering efficiency, Q_s, and extinction efficiency, Q_e, from Mie theory can be expressed as a series of terms of which the most significant terms are retained for the Rayleigh approximation ($|n|\chi \ll 1$) (van de Hulst, 1957),

$$Q_s = \frac{8}{3}\chi^4|K|^2 + \cdots, \tag{2.18}$$

and

$$Q_e = 4\chi\mathrm{Im}\{-K\} + \frac{8}{3}\chi^4|K|^2 + \cdots, \tag{2.19}$$

where,

$$K = \frac{n^2 - 1}{n^2 + 1}, \tag{2.20}$$

and since $Q_e = Q_a + Q_s$,

$$Q_a = 4\chi\mathrm{Im}\{-K\}. \tag{2.21}$$

For particles in the Rayleigh limit ($\chi \ll 1$), (unless $\mathrm{Im}\{-K\} \ll |K|^2$, such as a very weakly absorbing material), the absorption process is dominant since Q_a varies as χ and Q_s varies as χ^4, and scattering processes may be neglected. The accuracy of the Rayleigh approximation depends on the validity of the relation $|n|\chi \ll 1$, and as shown by Gunn and East (1954) in Figure 2.1, the Rayleigh approximation is best for the 3 mm wavelength (100 GHz) curve due to the frequency dependence of water's index of refraction. The size parameter is generally considered to be small enough if

$$|n|\chi < 0.5 \tag{2.22}$$

which reduces to $\chi < 0.13$ at 100 GHz where water's complex index of refraction at 18° C is $n_w = 3.41 - j1.94$ (Ulaby *et al.*, 1981). The complex index of refraction for water has a temperature dependence which decreases the index of refraction with decreasing temperature by approximately 2% per degree Celsius (Ray, 1972), this in turn extends

Table 2.2

Table 2.2: Characteristic Size Parameters (χ) for the SSM/I instrument.

Frequency (GHz)	wavelength (mm)	droplet radius (μm) 1	10	20	50	100
19.35	15.50	0.0004	0.0041	0.0081	0.0203	0.0405
22.235	13.49	0.0005	0.0047	0.0093	0.0233	0.0466
37.0	8.11	0.0008	0.0077	0.0155	0.0387	0.0775
85.5	3.51	0.0017	0.0179	0.0358	0.0895	0.1791

the range of χ at colder temperatures for which the Rayleigh approximation is valid. At 0° C water's complex index of refraction at 85.5 GHz is $n_w = 2.89 - j1.48$ (Warren, 1984) which when substituted into Equation 2.22 results in $\chi < 0.15$. Applying this criterion to the SSM/I frequencies in Table 2.2, which lists the corresponding size parameters for a range of particle sizes, shows that the 85.5 GHz channel has the most severe droplet size limitation for which the Rayleigh approximation is still valid. For 85.5 GHz, the limit on χ can be written in terms of droplet size, $r < 84\mu$m, which encompasses nearly all droplet sizes in non-precipitating clouds (see Table 1.1).

Ice particles in the microwave region have a refractive index, n_i, that is smaller than that of water, n_w. The real part of the refractive index of ice is

$$n_i' \simeq \sqrt{\varepsilon_i'} = 1.78, \tag{2.23}$$

where $'$ denotes the real part and ε_i' is the real part of the dielectric constant of ice and is relatively independent of frequency (Warren, 1984; Ulaby *et al.*, 1986) although lower values ($n_i' \simeq 1.73$) have been reported by Perry and Straiton (1973) and Vant *et al.* (1974). The imaginary part of n_i (denoted by n_i'') is much smaller than n_i' ($n_i''/n_i' < 10^{-2}$), so that

$$|n_i| \simeq 1.78, \tag{2.24}$$

and substituting Equation 2.24 into 2.22 defines the Rayleigh limit for ice,

$$\chi < 0.28. \tag{2.25}$$

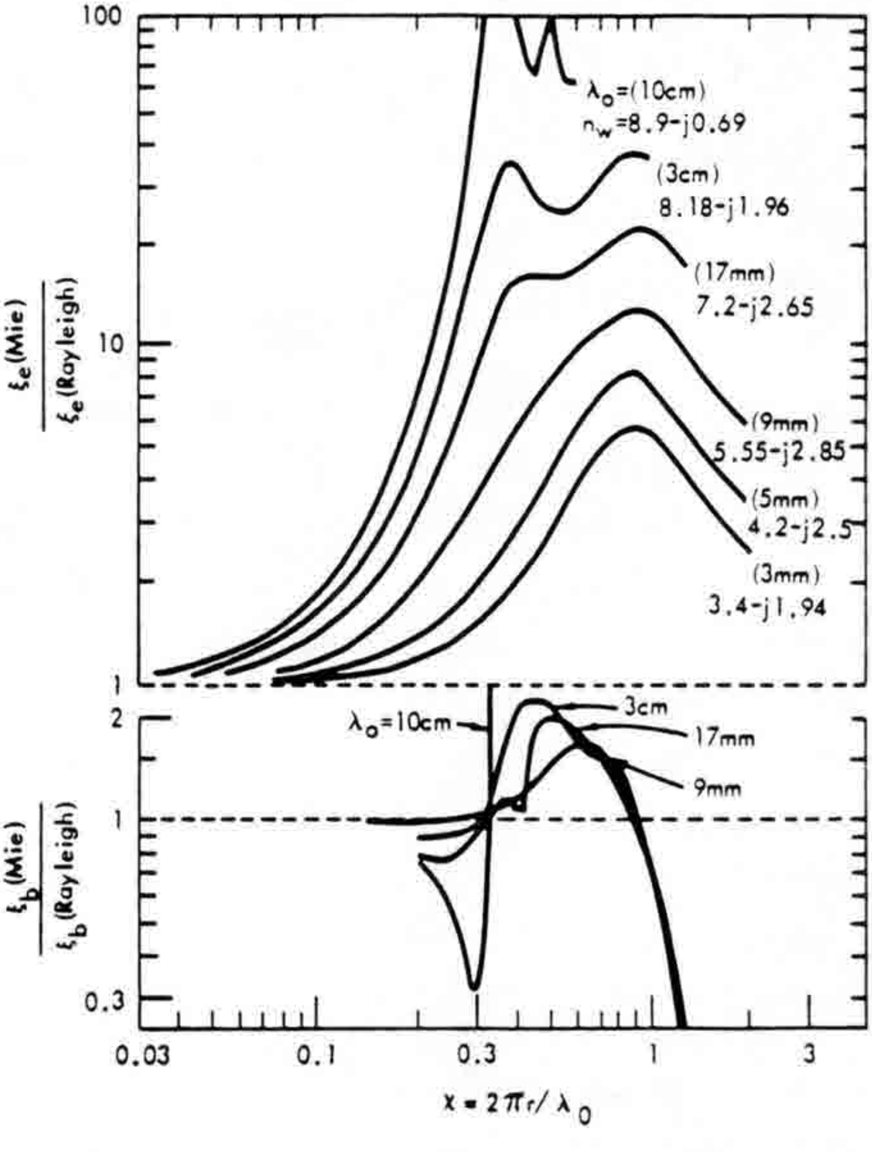

Figure 2.1: Ratio of Mie theory attenuation to that given by the Rayleigh approximation (from Gunn and East, 1954).

which yields a maximum effective ice droplet radius of 156 μm (at 85.5 GHz) for which the Rayleigh approximation is valid. For long cylindrical crystals, the effective spherical radius is approximately $(A_{sfc}/4\pi)^{1/2}$ where A_{sfc} is the surface area of the crystal, which is about a quarter of the actual crystal length (Stephens, 1980). Therefore the Rayleigh approximation can be considered valid for thin cylinders of length less than 624 μm.

Scattering due to ice is not necessarily negligible since ice is a weak absorber ($n_i''/n_i' < 10^{-2}$). Solving for the single scatter albedo, $\tilde{\omega}$, in the Rayleigh limit, using Equations 2.6, 2.11, 2.13, 2.18, and 2.21 yields,

$$\tilde{\omega} = \frac{2\chi^3|K|^2}{3\mathrm{Im}\{-K\} + 2\chi^3|K|^2}, \tag{2.26}$$

where $\tilde{\omega}$ is a function of ν, r, and n. Using values listed in Table 2.3 from Ray (1972) and Warren (1984) for the index of refraction for water and ice in Equation 2.26 yields a maximum single scattering albedo of 0.3084 for the 100 μm 85.5 GHz case for ice listed in Table 2.3. Such a high value seems to invalidate the non-scattering assumption to be made using the Rayleigh approximation, however, ice in the Rayleigh limit has an absorption coefficient two orders of magnitude smaller than liquid water (Benoit, 1968) therefore the scattering effects of ice, while sizeable to the ice absorption, is negligible compared to absorption by liquid water. Thus the Rayleigh limit approximation of negligible scattering in comparison to absorption is valid for clouds which are partially composed of ice and liquid water. Another result of the small absorption by ice compared to cloud liquid water is that microwaves can penetrate high ice clouds such as cirrus with relatively little attenuation.

By making use of the Rayleigh approximation, the integrated radiative transfer equation, Equation 2.4, may be simplified by assuming a non-scattering atmosphere , so that $\tilde{\omega} \approx 0$ and Equation 2.4 becomes,

$$L_\nu(s) = L_\nu(0)e^{-\delta(0,s)} + \int_0^s \sigma_e(s')B_\nu[T(s')]e^{-\delta(s',s)}ds'. \tag{2.27}$$

Table 2.3

Table 2.3: Single scatter albedos ($\bar{\omega}$) of water and ice in the Rayleigh limit for the SSM/I instrument.

		Frequency (GHz) 19.35	22.235	37.0	85.5
n_w^*		$5.37 - j2.96$	$4.98 - j2.84$	$3.93 - j2.39$	$2.89 - j1.48$
n_i^{**}		$1.786 - j0.0018$	$1.785 - j0.0020$	$1.785 - j0.0026$	$1.784 - j0.0043$
$\bar{\omega}_w$					
	1	6.918×10^{-10}	1.157×10^{-9}	2.924×10^{-9}	1.701×10^{-8}
	10	7.450×10^{-7}	9.614×10^{-7}	2.607×10^{-6}	1.673×10^{-5}
$r(\mu m)$	20	5.744×10^{-6}	7.448×10^{-5}	2.127×10^{-5}	1.338×10^{-4}
	50	9.041×10^{-5}	1.171×10^{-4}	3.309×10^{-4}	2.087×10^{-3}
	100	7.175×10^{-4}	9.362×10^{-4}	2.651×10^{-3}	1.648×10^{-2}
$\bar{\omega}_i$					
	1	1.193×10^{-8}	2.092×10^{-8}	6.591×10^{-8}	4.527×10^{-7}
	10	1.285×10^{-5}	1.737×10^{-5}	5.877×10^{-5}	4.450×10^{-4}
$r(\mu m)$	20	9.908×10^{-5}	1.346×10^{-4}	4.792×10^{-4}	3.549×10^{-3}
	50	1.557×10^{-3}	2.112×10^{-3}	7.406×10^{-3}	5.272×10^{-2}
	100	1.223×10^{-2}	1.665×10^{-2}	5.654×10^{-2}	3.084×10^{-1}

*Complex index of refraction for water at 0° C from Ray(1972).

**Complex index of refraction for ice at −5° C from Warren (1984).

2.1.4 The Transmittance Function and the Plane-parallel Atmosphere Approximation

The transmittance function is defined as,

$$\tau_\nu(s_1, s_2) \equiv e^{-\delta(s_1,s_2)} = \frac{L_\nu(s_1)}{L_\nu(s_2)}, \tag{2.28}$$

such that for a non-attenuating atmosphere $\tau_\nu = 1$, and for an opaque atmosphere $\tau_\nu = 0$. Another approximation used to simplify the radiative transfer equation is the plane-parallel atmosphere approximation. The schematic in Figure 2.2 shows that the optical path, ds, through a horizontally homogeneous atmosphere can be approximated by $\sec\theta dz$ where θ is the satellite zenith angle and dz is the normal optical path length. The transmittance function then becomes,

$$\tau_\nu(\theta, p_1, p_2) \approx e^{-\sec(\theta)\delta(p_1,p_2)}, \tag{2.29}$$

which is a function of zenith angle and pressure levels p_1 and p_2. Substituting Equation 2.29 into Equation 2.27 yields,

$$L_\nu(p) = L_\nu(p_s)\tau_\nu(p_s, p) + \int_{p_s}^{p} B_\nu[T(p')]\frac{\partial\tau_\nu(p', p)}{\partial p}dp', \tag{2.30}$$

which is the integrated radiative transfer equation for a non-scattering atmosphere assuming plane-parallel geometry, where the θ dependence is understood.

For highly variable quantities such as precipitating clouds, significant differences can result between brightness temperature estimates of plane-parallel clouds and finite clouds (Kummerow and Weinman, 1988). Footprint-filling errors, which have been studied using fractal cloud models (Lovejoy *et al.*, 1987; Lovejoy and Schertzer, 1988), are due to the nonlinearities of the finite cloud radiation field. The same effect is present in cloud liquid water fields but to a lesser degree. The radiatively derived parameters in this study should therefore be thought of as plane-parallel equivalent parameters.

2.1.5 Surface Boundary Conditions

Before using Equation 2.30 the surface radiance term, $L_\nu(p_s)$, must be determined. For infrared wavelengths, the surface emits approximately as an ideal blackbody and its

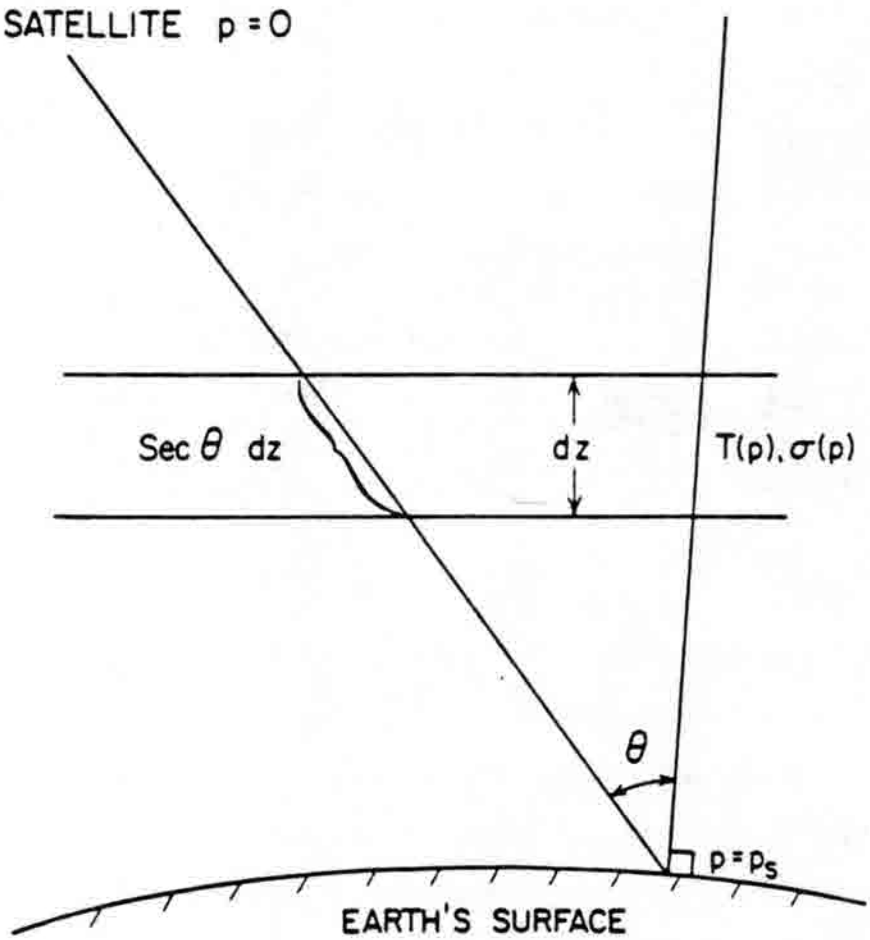

Figure 2.2: Plane-parallel geometry.

surface radiance is just $B_\nu(T_s)$ where B is the Planck function and T_s is the surface skin temperature, then Equation 2.30 becomes,

$$L_\nu(0) = B_\nu(T_s)\tau_\nu(p_s,0) + \int_{p_s}^{0} B_\nu[T(p)]\frac{\partial\tau_\nu(p,0)}{\partial p}dp, \tag{2.31}$$

for the satellite's orbit position at $p = 0$. However, the surface does not emit as a blackbody in the microwave region.

In general, an electromagnetic wave incident on a surface boundary can be characterized by its reflectance, absorptance, and transmittance, ρ, α, τ, respectively, and usually has a strong dependence on the angle of incidence. To assure that energy is conserved, the sum of the reflectance, absorptance, and transmittance must be unity,

$$\rho + \alpha + \tau = 1. \tag{2.32}$$

A common quantity related to the reflectance is the surface emittance, ϵ_ν, and is defined as the ratio of the observed brightness temperature to the brightness temperature an ideal blackbody would have at that thermodynamic temperature,

$$\epsilon_\nu \equiv \frac{T_B}{T_{B_{\epsilon_\nu=1}}}, \tag{2.33}$$

and for a specular surface (a mirror-like surface),

$$\epsilon_\nu = 1 - \rho = \alpha + \tau. \tag{2.34}$$

If the surface is considered opaque ($\tau \approx 0$), then the surface emittance is directly related to the absorptance, and the radiance of a surface with temperature T and surface emittance ϵ_ν is then given by,

$$L_\nu(sfc) = \epsilon_\nu B_\nu(T_s). \tag{2.35}$$

The rest of the radiance from the surface is due to reflected radiation from above the surface. The total upward radiance at the surface is the sum of the downward contribution of the atmosphere reflected by the surface,

$$L_\nu \downarrow = \int_{0}^{p_s} B_\nu[T(p)]\frac{\partial\tau_\nu(p,p_s)}{\partial p}dp, \tag{2.36}$$

the deep space emission, $B_\nu(T_{space})$, due to cosmic background radiation, and the radiance emitted upward by thermal emission, $L_\nu(sfc)$. The total upward radiance is then,

$$\begin{aligned} L_\nu(p_s) &= (1-\epsilon_\nu)\int_0^{p_s} B_\nu[T(p)]\frac{\partial\tau_\nu(p,p_s)}{\partial p}dp \\ &+ (1-\epsilon_\nu)\tau_\nu(0,p_s)B_\nu(T_{space}) \\ &+ \epsilon_\nu B_\nu(T_s). \end{aligned} \tag{2.37}$$

Substituting Equation 2.37 into Equation 2.30 and using the multiplicative property of the transmittance function for monochromatic light,

$$\tau_\nu(0,p_s) = \tau_\nu(0,p)\cdot\tau_\nu(p,p_s), \tag{2.38}$$

which provides the relation,

$$\frac{\partial\tau_\nu(p,p_s)}{\partial p} = -\frac{\tau_\nu(p_s,0)}{[\tau_\nu(p,0)]^2}\frac{\partial\tau_\nu(p,0)}{\partial p}, \tag{2.39}$$

yields the integrated radiative transfer equation for a non-scattering, plane-parallel atmosphere with a non-blackbody surface boundary condition:

$$\begin{aligned} L_\nu(0) &= \epsilon_\nu B_\nu(T_s)\tau_\nu(p_s,0) \\ &+ \int_{p_s}^{0} B_\nu[T(p)]\frac{\partial\tau_\nu(p,0)}{\partial p}dp \\ &+ (1-\epsilon_\nu)[\tau_\nu(p_s,0)]^2\int_{p_s}^{0}\frac{B_\nu[T(p)]}{[\tau_\nu(p,0)]^2}\frac{\partial\tau_\nu(p,0)}{\partial p}dp \\ &+ (1-\epsilon_\nu)[\tau_\nu(p_s,0)]^2 B_\nu(T_{space}). \end{aligned} \tag{2.40}$$

As we can see, the radiance is a function of surface temperature, surface emittance, the atmosphere's transmittance, which is a function of the temperature and moisture profile, and the deep space emission temperature. Since the deep space emission temperature is small ($T_{space} \approx 2.7$ K) in comparison to the atmospheric emission temperature above 5 GHz, it is usually neglected, but is presented here for completeness.

The atmospheric weighting function is a useful tool for understanding how the atmosphere contributes to the upwelling radiance as viewed from the satellite. By rearranging

Equation 2.40, the upwelling radiance can be expressed as,

$$\begin{aligned} L_\nu(0) &= \epsilon_\nu B_\nu(T_s)\tau_\nu(p_s,0) \\ &+ (1-\epsilon_\nu)[\tau(p_s,0)]^2 B_\nu(T_{space}) \\ &+ \int_{p_s}^{0} B_\nu[T(p)]W(p)dp, \end{aligned} \tag{2.41}$$

where the first two terms are the attenuated boundary source terms and the last term is the atmospheric source term, where $W(p)$ is the atmospheric weighting function (Grody, 1983),

$$W(p) = \frac{\partial \tau_\nu(p,0)}{\partial p} + (1-\epsilon_\nu)\left[\frac{\tau_\nu(p_s,0)}{\tau_\nu(p,0)}\right]^2 \frac{\partial \tau_\nu(p,0)}{\partial p}, \tag{2.42}$$

which describes the relative contribution of each layer in the atmosphere to the total atmospheric component of the upwelling radiance.

2.2 ATMOSPHERIC EFFECTS

2.2.1 Gaseous Absorption

It is useful to review the basic characteristics of radiative transfer through the atmosphere in the microwave region. Microwaves have a wide range of behavior at different spectral regions. In the lower frequencies, 1 - 15 GHz, the atmosphere is transparent even to clouds and moderate rain rates, but in the higher frequencies (> 15 GHz) molecular absorption bands become more prominent and the atmosphere becomes more opaque to microwave radiation. The main gaseous atmospheric constituents attenuating the radiation are oxygen and water vapor (Liebe, 1985). Oxygen has a nearly constant mixing ratio for the lower atmosphere (below 30 km) while water vapor is highly variable and is concentrated at the lowest levels of the atmosphere. In Figure 2.3 from Liebe (1985), curve 1 represents the attenuation due to oxygen alone and curves 2-9 represent the attenuation for increasing amounts of water vapor at a given pressure and temperature. Features to note are the two oxygen absorption peaks at 60 GHz and 118.75 GHz, the water vapor lines at 22.235 GHz, 183.31 GHz and 325.15 GHz, and the gradual increase of attenuation with frequency due to the water vapor continuum absorption. The oxygen absorption peaks at 60 GHz and 118.75 GHz are the result of the electromagnetic radiation interacting with the O_2 molecule's magnetic dipole moment causing the the molecule's spin orientation to change which results in the emission and absorption of photons at 60 GHz (which is actually a group of lines) and 118.75 GHz (Van Vleck, 1947a; Herzburg, 1950). The water vapor rotational bands at 22.235 GHz and 183.31 GHz are caused by the electric dipole moment of the H_2O molecule which also interacts with the microwave radiation (Van Vleck, 1947b). The absorption spectra of these lines from quantum theory would ideally be discrete spikes, but due to pressure broadening the lines appear thick. Many different models have been used to describe the actual shape of these lines and will not be mentioned here. A summary of Dr. Hans J. Liebe's Millimeter-wave Propagation Model (MPM) used in this work is presented in Appendix A.

The window regions of the microwave spectrum, labeled W1, W2, etc. in Figure 2.3, are not true windows, for example the W2 window in which the SSM/I 85.5 GHz channel resides has more attenuation than the 22.235 GHz water vapor absorption line. The SSM/I instrument has channels in the W1 and W2 window regions and at the 22.235 GHz water vapor absorption line, hence the name *imager* as opposed to *sounder*. Microwave temperature sounding instruments are usually centered on the 60 GHz oxygen absorption lines, and new sounding instruments have been proposed for the 118.75 GHz oxygen line, and the 183.31 GHz water vapor absorption line (Kakar, 1983; NASA, 1987; Simpson *et al.*, 1988). The low frequencies in the 1-10 GHz range have low spatial resolution and are used mainly for estimating land and ocean surface parameters due to their ability to penetrate clouds and most vegetation (Wilheit, 1978a; Schmugge, 1983; Becker and Choudhury, 1988).

2.2.2 Absorption by Hydrometeors

It was shown in section 2.1.3 that spherical particles can absorb and scatter microwave radiation and that the complete solution for a single particle of radius r can be represented by the scattering, absorption, and extinction cross-sections, A_a, A_s, A_e given by Equations 2.10, 2.12, and 2.14. A representative volume in an atmosphere can contain several particles of different sizes which interact with the electromagnetic radiation.

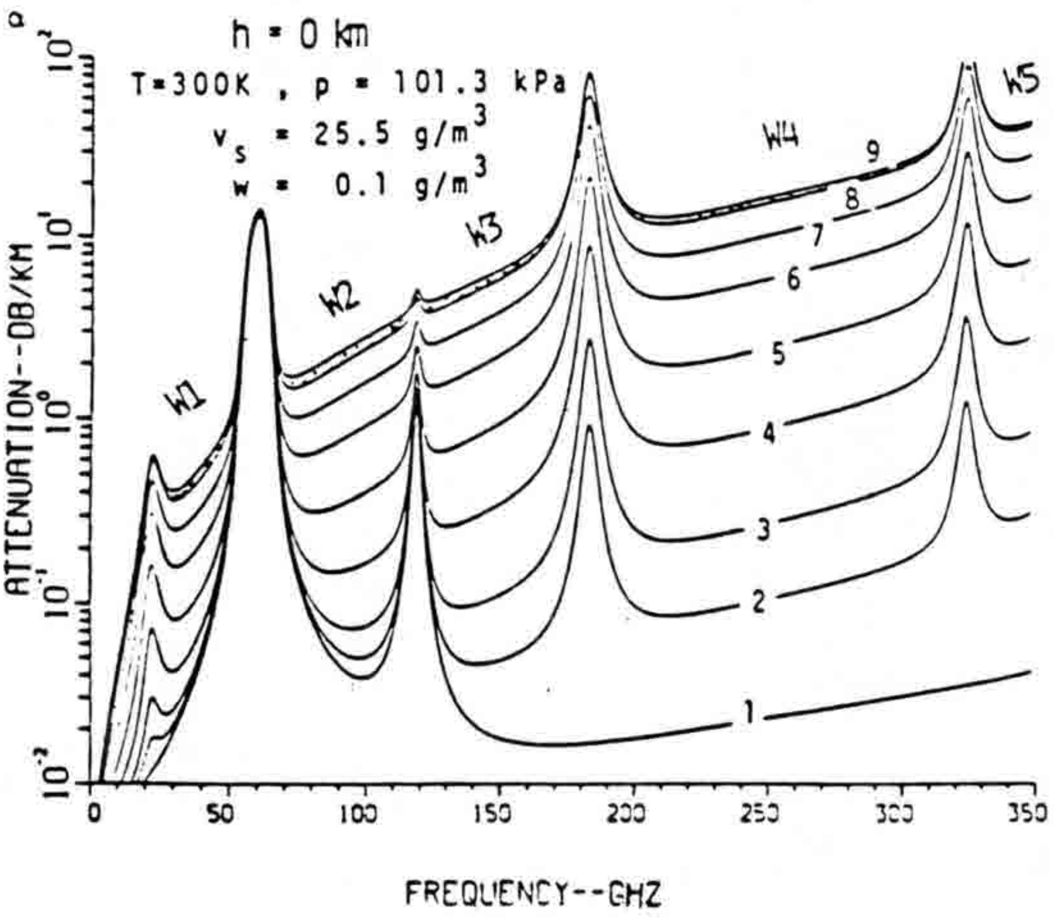

Figure 2.3: Microwave atmospheric attenuation (from Liebe, 1985).

The combined effects of the particles in the volume can be represented by the volume absorption coefficient,

$$\sigma_a = \int_0^\infty p(r) A_a(r) dr, \tag{2.43}$$

where $p(r)$ is the drop-size distribution, and r is the particle radius.

There are two alternatives at this point, one is to assume that the particles are relatively small and make the Rayleigh approximation, and the other is to consider the particles large enough to require the full Mie equations. Of considerable convenience is the natural size differential of cloud droplets and precipitation which enables atmospheric liquid water to be divided into two classes: non-precipitating clouds and precipitating clouds (Deirmendjian, 1963). Assuming non-precipitating clouds allows the application of the Rayleigh approximation for the SSM/I frequencies.

Substituting Equations 2.10, 2.16, and 2.21 into Equation 2.43 and taking the Rayleigh limit yields,

$$\sigma_a = \frac{8\pi^2}{\lambda_b} \mathrm{Im}\{-K\} \int_0^\infty p(r) r^3 dr, \tag{2.44}$$

and since the cloud water content in the volume is given by,

$$m_v = \frac{4\pi\rho_L}{3} \int_0^\infty p(r) r^3 dr, \tag{2.45}$$

where ρ_L is the water density, the volume absorption coefficient is directly related to cloud water content,

$$\sigma_a = \frac{6\pi}{\lambda_b \rho_L} \mathrm{Im}\{-K\} m_v. \tag{2.46}$$

The absorption coefficient is not a function of the droplet size distribution in the Rayleigh limit, and allows the calculation of the absorption coefficient with a more convenient parameter, liquid water content (Westwater, 1972).

However, for precipitation sized particles the full Mie theory must be used. When scattering processes are included, the high frequency channels such as the 85.5 GHz channel can have brightness temperatures well below their actual thermal temperature as shown by Wu and Weinman (1984) using their radiation model in Figure 2.4. This is due to the scattering of cold deep space radiation by the large precipitation sized particles into the satellite's sensor. Brightness temperatures can be as low as 100 K which represents a dynamic range of approximately 200 K. The most responsible component for the large scattering effects are ice particles in the higher levels of the precipitating clouds. Figure 2.5 from Spencer *et al.* (1988) shows that ice and water have comparable volume scattering coefficients but that ice has negligible volume absorption compared to water which is the cause of the significantly higher single scatter albedo of ice than for water.

2.3 SURFACE EFFECTS

A key to understanding microwave remote sensing techniques, is to realize that the surface emittance can vary depending on the electromagnetic properties of the surface. For land the surface emittance varies due to soil moisture content and can range from near unity for dry soils to less than 0.6 for wet soils (Wang and Schmugge, 1980; Schmugge, 1985). In fact, remote sensing of soil moisture is one of the many areas of remote sensing applications which use the surface emittance to sense surface characteristics. The surface emittance of water is approximately 0.5, so that water surfaces appear very cold. This leads to the effect of clouds appearing relatively warm over ocean surfaces since the clouds emit microwave radiation more efficiently at a higher brightness temperature. The application of the radiatively cold ocean surface is referred to as emission based microwave remote sensing (Grody, 1976; Wilheit *et al.*, 1977). Frequencies generally used are in the 10-37 GHz range where emission and absorption dominate over scattering processes in the precipitating clouds. The limitation of this technique is that it is necessary to have a cold surface background to observe measurable brightness temperature differences, and is therefore ineffective over land surfaces.

Polarization of electromagnetic radiation is another surface effect and is used for soil moisture and sea ice determination among others (McFarland *et al.*, 1984; Comiso, 1985; Becker and Choudhury, 1988). It is similar to the glare off a table. The reflected light is polarized preferentially in the horizontal due to the horizontal polarization's higher reflectance. The reflectance of an electromagnetic wave by a specular dielectric surface is given by the square of the magnitude of the Fresnel reflection coefficients (Reitz

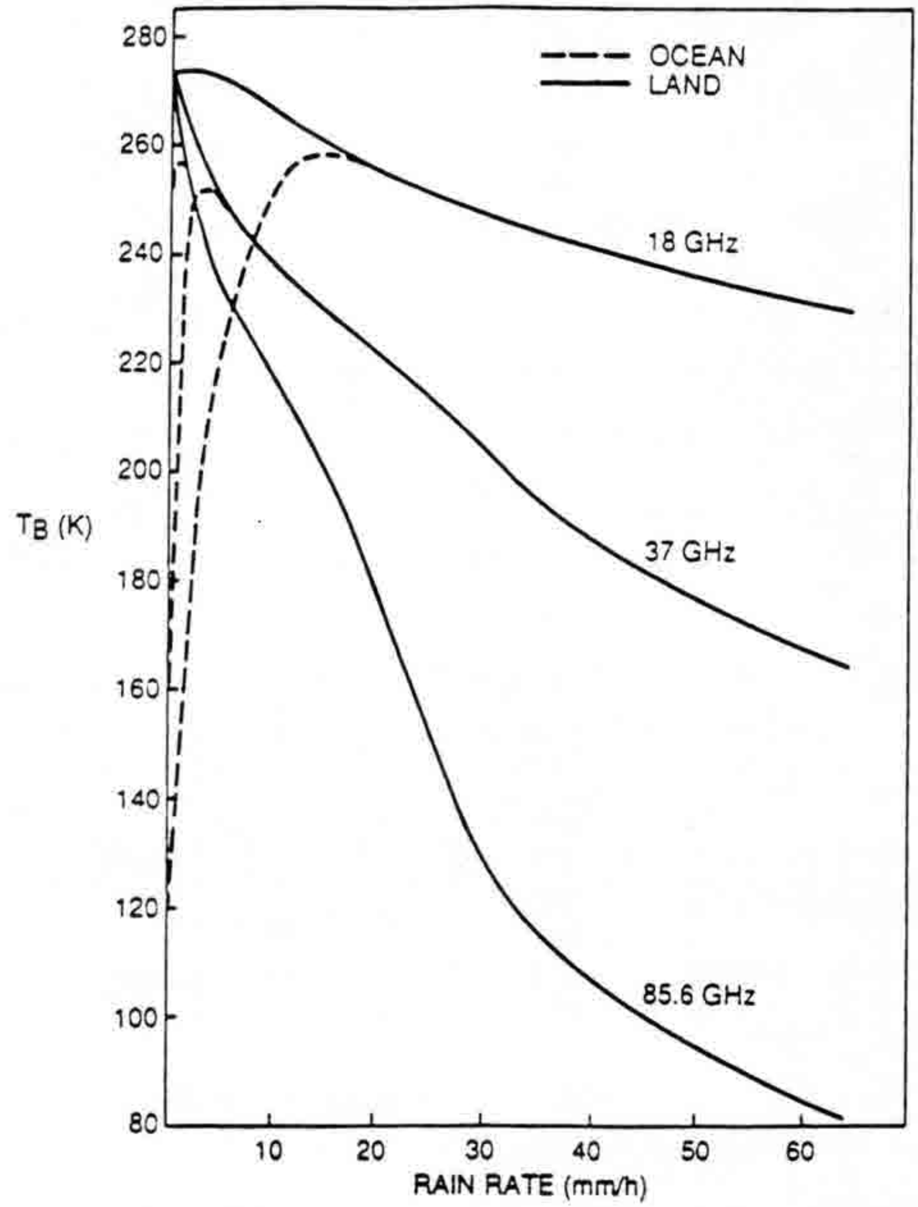

Figure 2.4: Brightness temperature - rain rate relationships at 18, 37, and 85.6 GHz from the radiative transfer modeling of Wu and Weinman (1984) (from Spencer *et al.*, 1988).

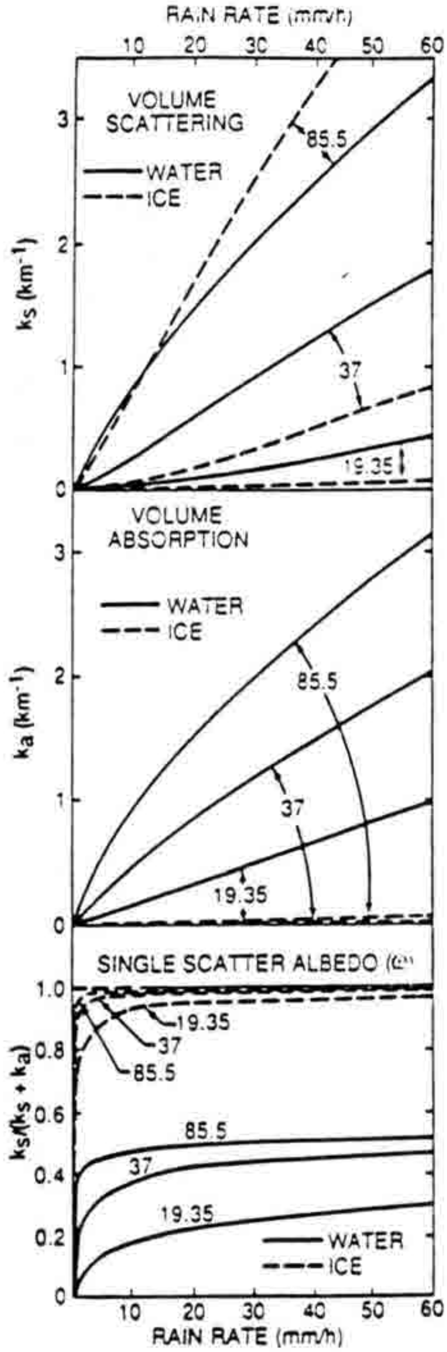

Figure 2.5: Mie volume scattering coefficients (top), volume absorption coefficients (middle), and single scattering albedos (bottom) of water and ice spheres (from Spencer *et al.*, 1988).

et al., 1979),

$$\rho_h = \left| \frac{\cos\theta - \sqrt{\varepsilon - \sin^2\theta}}{\cos\theta + \sqrt{\varepsilon - \sin^2\theta}} \right|^2, \tag{2.47}$$

for horizontal polarization and,

$$\rho_v = \left| \frac{\varepsilon\cos\theta - \sqrt{\varepsilon - \sin^2\theta}}{\varepsilon\cos\theta + \sqrt{\varepsilon - \sin^2\theta}} \right|^2, \tag{2.48}$$

for vertical polarization, where θ is the angle of incidence and ε is the relative complex dielectric constant for the two mediums. Recalling from section 2.1.5 that $\epsilon = 1 - \rho$, then the surface emittance must also have different values for each polarization, with the vertical polarization surface emittance generally greater than the horizontal polarization.

Among the most important properties influencing the dielectric constant for land surfaces is soil moisture. Values of ε for varying degrees of wetness from Schmugge and Choudhury (1981) shown in Figure 2.6, show a marked increase in ε for increasing levels of soil moisture. An increase in the dielectric constant corresponds to a decrease in the surface emittance. Soil depth penetration by the electromagnetic radiation has been theoretically (Wilheit, 1978b) and experimentally (Newton *et al.*, 1982) determined to be on the order of a few tenths of a wavelength. Application to the SSM/I instrument frequencies show that the effective surface emittance is from the top 1 cm of the soil and is therefore sensitive to surface soil moisture and not sub-surface soil moisture.

Other influences on the surface emittance are surface roughness, and non-homogeneity of the surface which can be due to wind speed and salinity for ocean surfaces (Kidder, 1979), and vegetation, terrain, etc. for land surfaces (Choudhury *et al.*, 1979; Schmugge *et al.*, 1980; Owe *et al.*, 1988). For a spectral surface the reflected electromagnetic radiation is entirely coherent and obeys Snell's Law of $\theta_i = \theta_r$, so that the angle of incidence equals the angle of reflection. As the surface becomes rougher the scattering due to the surface has a larger diffuse component in addition to the coherent reflection until for a Lambertian surface (a perfectly rough surface) the scattered radiation is composed entirely of a diffuse component such that,

$$\sigma^\circ(\theta_i, \theta_s) = \sigma_0^\circ \cos\theta_i \cos\theta_s, \tag{2.49}$$

where σ° is the bistatic scattering coefficient and θ_s is the scattering angle (Ulaby *et al.*, 1986). The surface emittance of a Lambertian surface is then (Peake, 1959),

$$\begin{aligned} \epsilon_{\nu}(\theta_i, \phi_i) &= 1 - \frac{1}{4\pi \cos\theta_0} \int_0^{2\pi} \int_0^{\pi/2} \sigma_0^{\circ} \cos\theta_i \cos\theta_s \sin\theta_s d\theta_s d\phi_s, & (2.50) \\ &= 1 - \frac{\sigma_0^{\circ}}{4}, & (2.51) \end{aligned}$$

which is independent of polarization and angle. Several studies have been made on vegetation's effect on surface emission, but nearly all the studies have been made for low frequency channels ($<$ 10 GHz). The results are very diverse since several variables can change from one experiment to another. Studies have been made which treat row crops as thin dielectric cylinders, and such things as coefficients of air-leaf reflectivity, leaf-loss factors, attenuation of wheat with and without grain heads, moisture content of the vegetation among a seemingly endless list of possible variations are used as parameters to estimate surface emittance values (see Ulaby *et al.*, 1986 for a summary of current research in this area). In summary, theoretical calculation of surface effects is a non-trivial task.

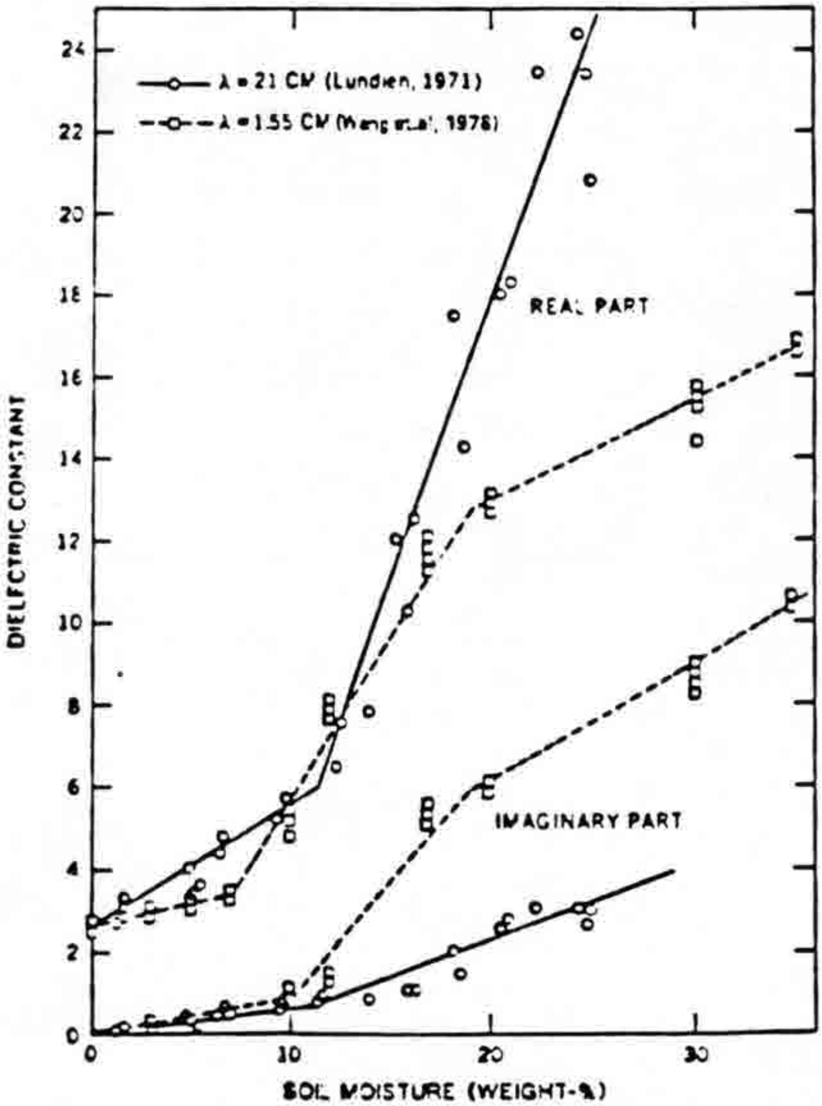

Figure 2.6: Real and imaginary parts of the dielectric constant for soils with varying moisture content (from Schmugge and Choudhury, 1981).

Chapter 3

DATA

3.1 GENERAL INFORMATION

The area and time selected for the case study was northeast Colorado during the first week of August 1987. The coverage provided by the SSM/I instrument is twice daily with equator crossing times near 0612 local time. The crossing times over Colorado are approximately 0130 UTC and 1250 UTC for the descending and ascending orbits. During this period the Convective Initiation and Downburst Experiment (CINDE) was in progress in a smaller subset of the case study area which provided extensive meteorological instrumentation in the case study region. The CINDE project was a joint effort with many governmental agencies and universities participating. For more on the project see Kessinger (1987,1988). Also during the case study, GOES satellite data was taken by the Colorado State University groundstation in support of the First International Satellite Cloud Climatology Project (ISCCP) Regional Experiment (FIRE) and provided near simultaneous coverage of the area with the SSM/I instrument. The domain of the selected area was an area approximately 500 km $\times$ 500 km centered on 104° W and 40° N (approximately 37° - 43° latitude and 101° - 107° longitude). The location of the CINDE network is shown by Figure 3.1. Figure 3.2 is an enlargement of the high density meteorological network. In particular, the high resolution soundings were used to supplement the normal National Weather Service (NWS) radiosonde stations. Several doppler radars were in place for the CINDE project and provided extensive coverage of the area. Unfortunately, none of the radars were operating during the times of the SSM/I orbit passes.

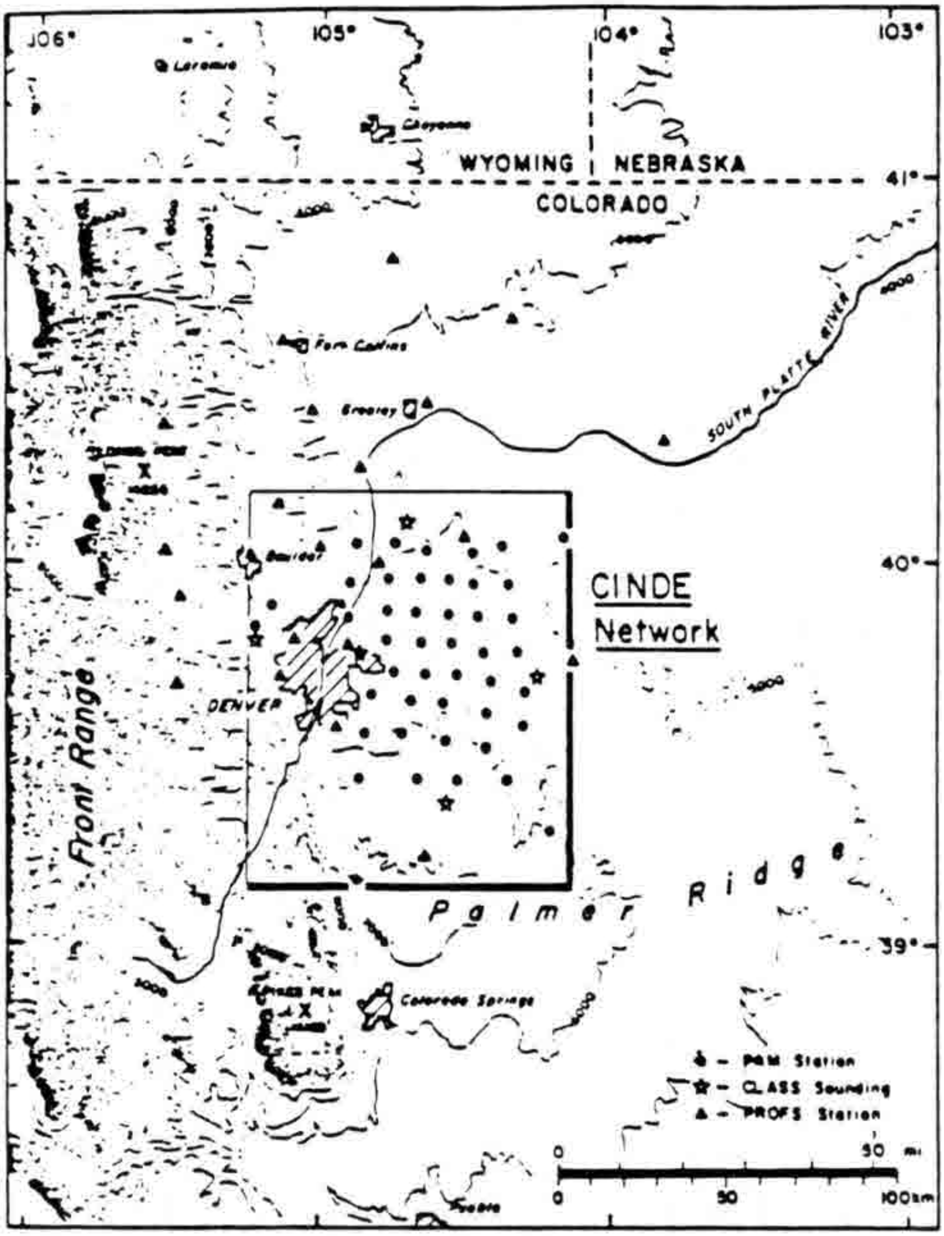

Figure 3.1: CINDE Network location (from Kessinger, 1987).

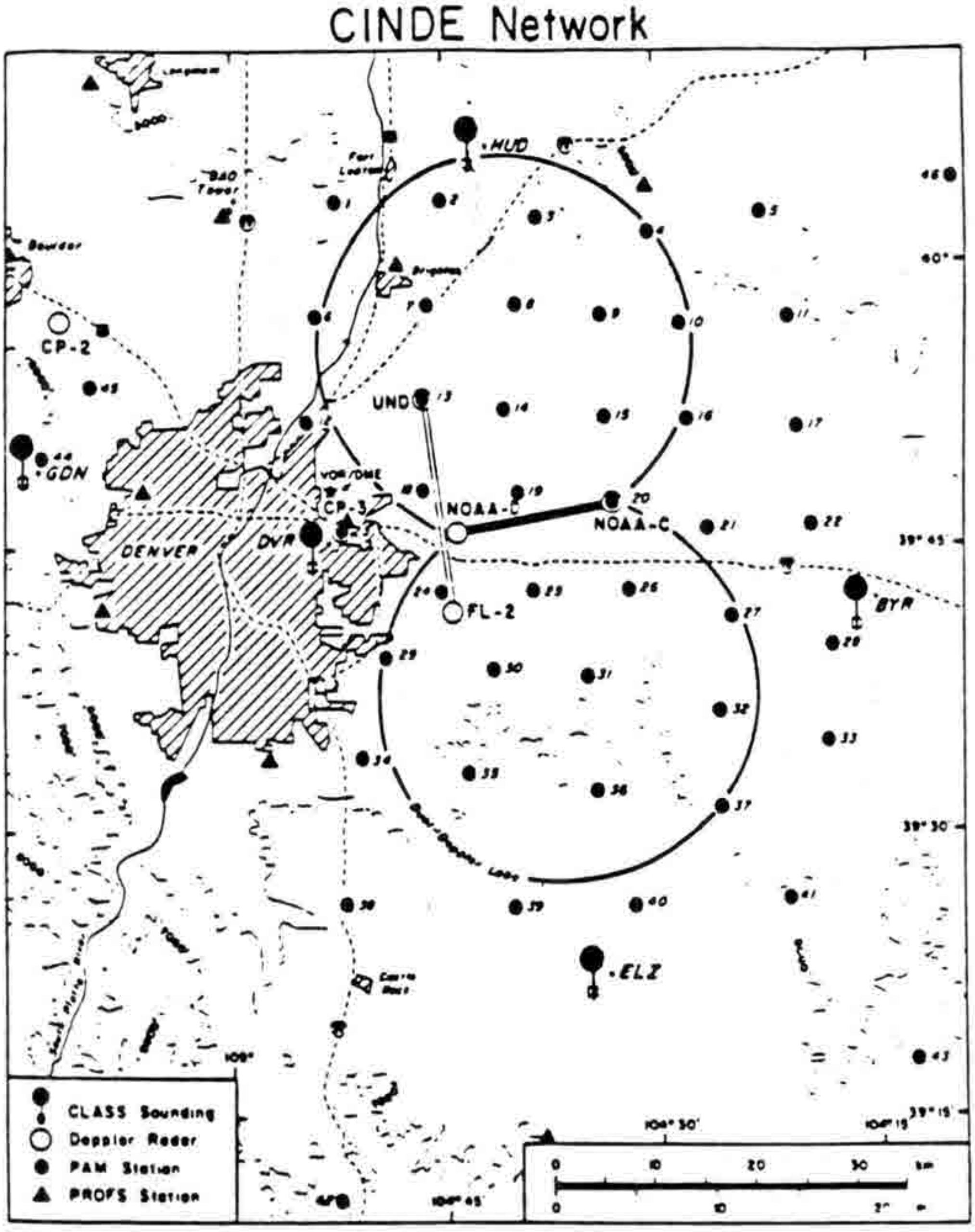

Figure 3.2: CINDE Surface Network (from Kessinger, 1987).

Table 3.1

Table 3.1: Satellite data case coverage summary over the region (37°-43° latitude and 101°-107° longitude).

Case number	SSM/I data coverage Time (UTC)	GOES data coverage Time (UTC)	cloud cover conditions
1	4 Aug. 0149	No matching data	—
2	5 Aug. 0136	5 Aug. 0045	clear
3	5 Aug. 1301	5 Aug. 1245	clear
4	6 Aug. 0124	6 Aug. 0145	clear
5	6 Aug. 1249	6 Aug. 1445	partly cloudy
6	7 Aug. 0112	7 Aug. 0045	cloudy
7	7 Aug. 1240	7 Aug. 1245	cloudy
8	11 Aug. 0204	11 Aug. 0145	clear

3.1.1 Satellite Data Sets

Coincident satellite coverage was obtained for a continuous 3 day period from 5 August to 7 August. Table 3.1 summarizes the satellite coverage available by each satellite and their respective times. Each case study has been assigned a number and will be referenced throughout this paper by the case number assigned by Table 3.1. The GOES and SSM/I data sets are within one hour of each other with several just a few minutes apart with the exception of case 5. Images of the SSM/I brightness temperatures are similar in appearance to the GOES infrared data with clouds appearing radiatively cold (white) as in Figure 3.3 but water surfaces are notably colder due to the low surface emittance. Convective regions in the SSM/I imagery are extremely cold in comparison to the infrared data in Figure 3.4. Work by Wu (1988), and Spencer *et al.* (1988) have shown that the cold temperatures are due to scattering by precipitation sized ice particles. An enlargement of the convective storm in Nebraska in Figure 3.5 shows a minimum brightness temperature of 182 K.

3.1.2 Atmospheric Synoptic Conditions

The case study area was dominated by a dry air mass following a cold front passage on 4 August (see Figure 3.6), 500 hPa winds were also light over the region. The region was mainly clear for cases 2-4, with increasing cloud amounts by case 5. Remains of two

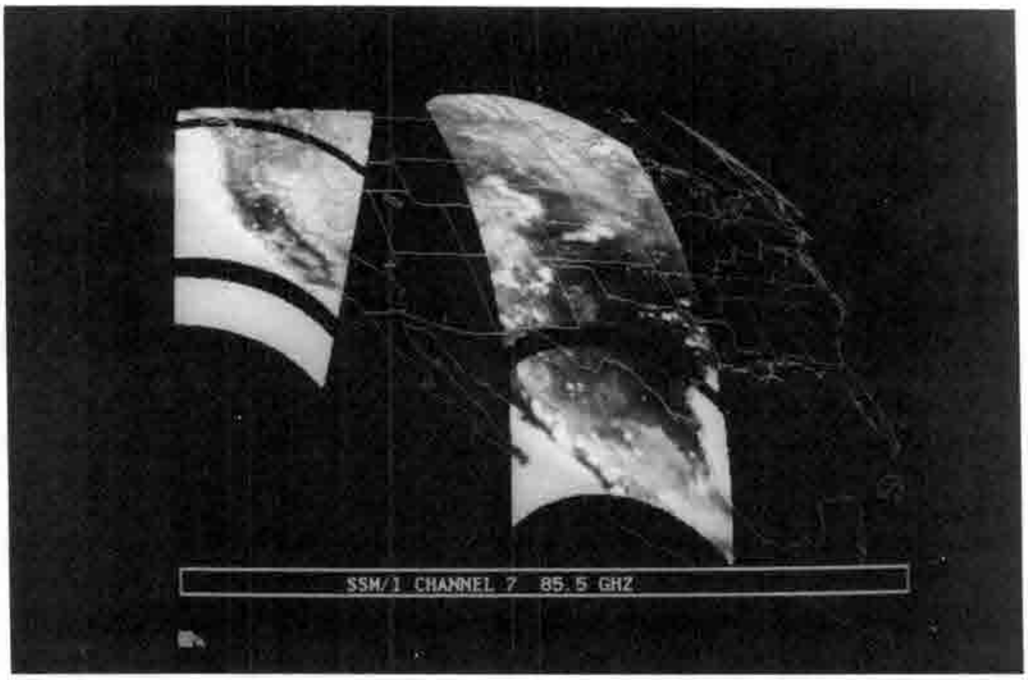

Figure 3.3: An example of SSM/I channel 7 imagery.

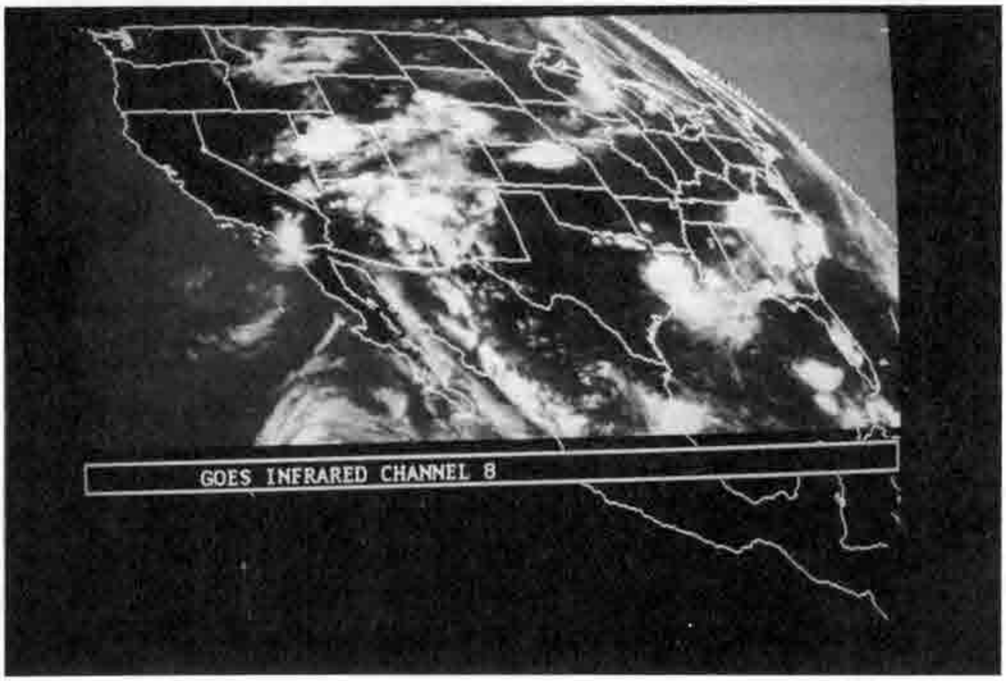

Figure 3.4: An example of coincident infrared GOES imagery.

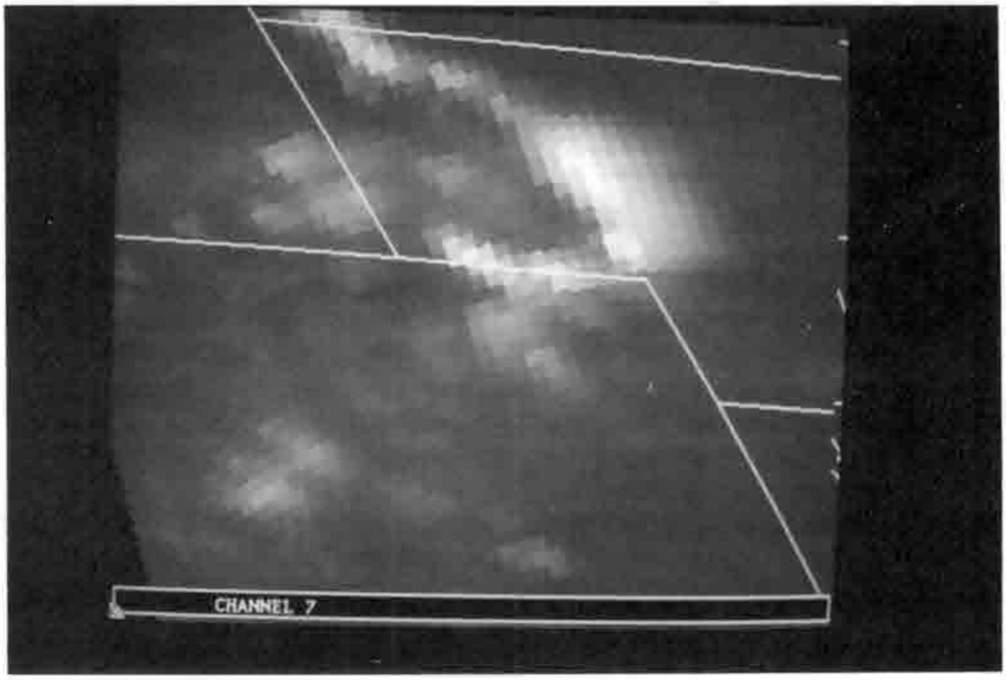

Figure 3.5: Enlargement of SSM/I channel 7 imagery.

hurricanes (Greg and Hillary) in the Pacific off the coast of Mexico supplied a northward flux of moisture which later developed into convective activity. On 6 August another surface cold front entered the region which initiated the convection on 7 August (case 6) (see Figure 3.7) with a large storm in the Nebraska panhandle. Behind the cold front passage weak upslope conditions produced more stratiform-like clouds (case 7) which persisted until 8 August. The region was clear during the last satellite orbit pass (case 8). The precipitation from the observed National Meterological Center (NMC) 24 hour precipitation maps showed the heaviest precipitation in the area for the 24 hours preceding 4 August 12 UTC when the Nebraska panhandle region received up to 2 inches (50 mm) of precipitation. Precipitation was recorded in extreme northeast Colorado on 5 August where a station reported 1.22 inches (31 mm) of precipitation. Throughout the remainder of the case study only scattered light amounts (< 5 mm) were reported from 7 August to 11 August.

3.1.3 Soil Moisture Conditions

Soil moisture conditions in Figure 3.8 prior to the case study on 1 August show the case study region to be abnormally to slightly dry for crop needs. The total precipitation for the week of 26 July to 1 August was minimal as can be seen in Figure 3.9 with the largest amounts being reported in the Colorado Rocky Mountains which received a little over 0.5 inches (13 mm) of precipitation. However, during the week of the case study, soil moisture conditions (shown in Figure 3.10) improved to slightly dry with only southeast Colorado and west-central Kansas remaining abnormally dry. The majority of rain fell in the Nebraska panhandle region (see Figure 3.11) which had over 2 inches (50 mm) of precipitation (*Weekly Weather and Crop Bulletin*, 1987).

3.2 GOES VISSR INSTRUMENT DESCRIPTION

The Geostationary Operational Environmental Satellite (GOES) series are operated by the National Oceanic and Atmospheric Administration (NOAA). Presently, two such satellites are in operation over the Western Hemisphere, GOES-6 (GOES-WEST) and

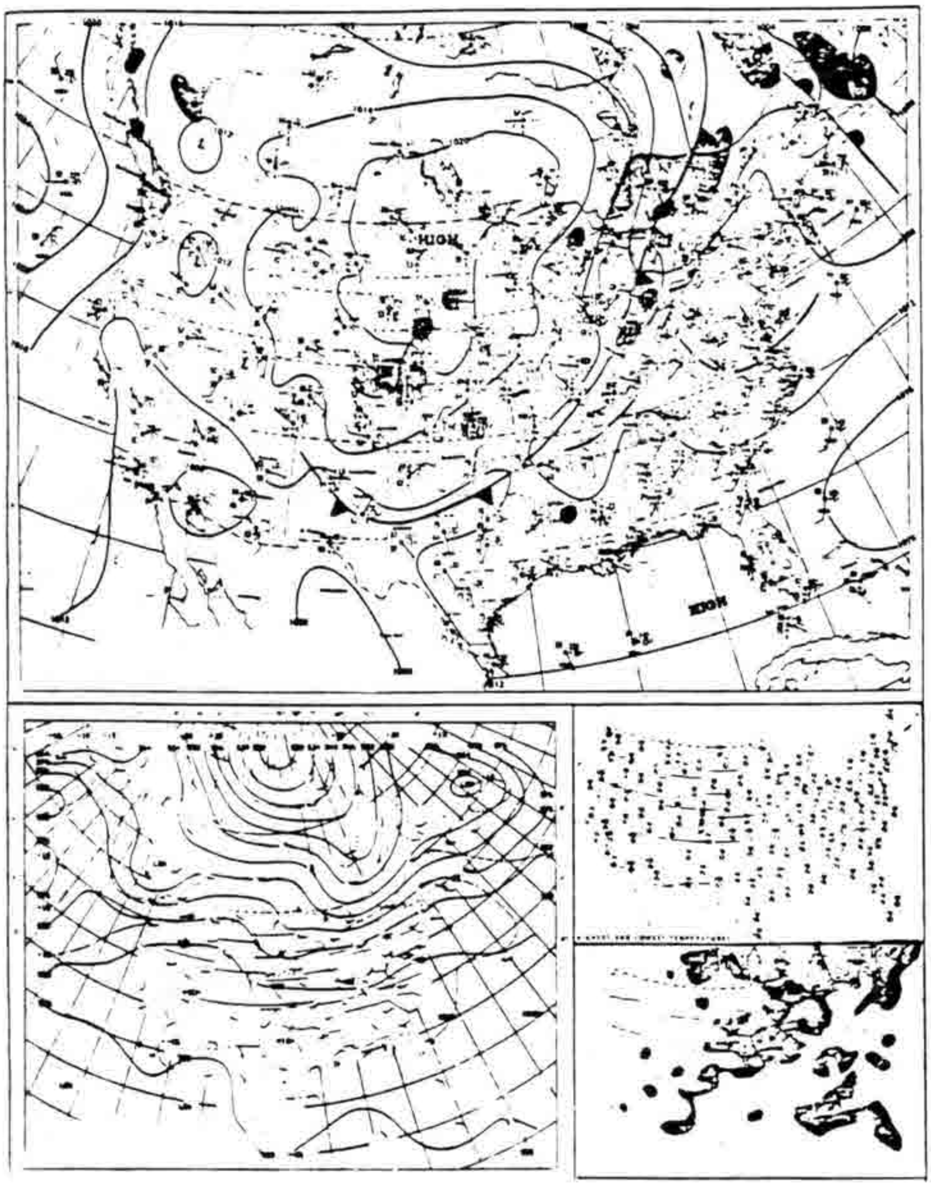

Figure 3.6: Synoptic conditions 4 August 1100 UTC.

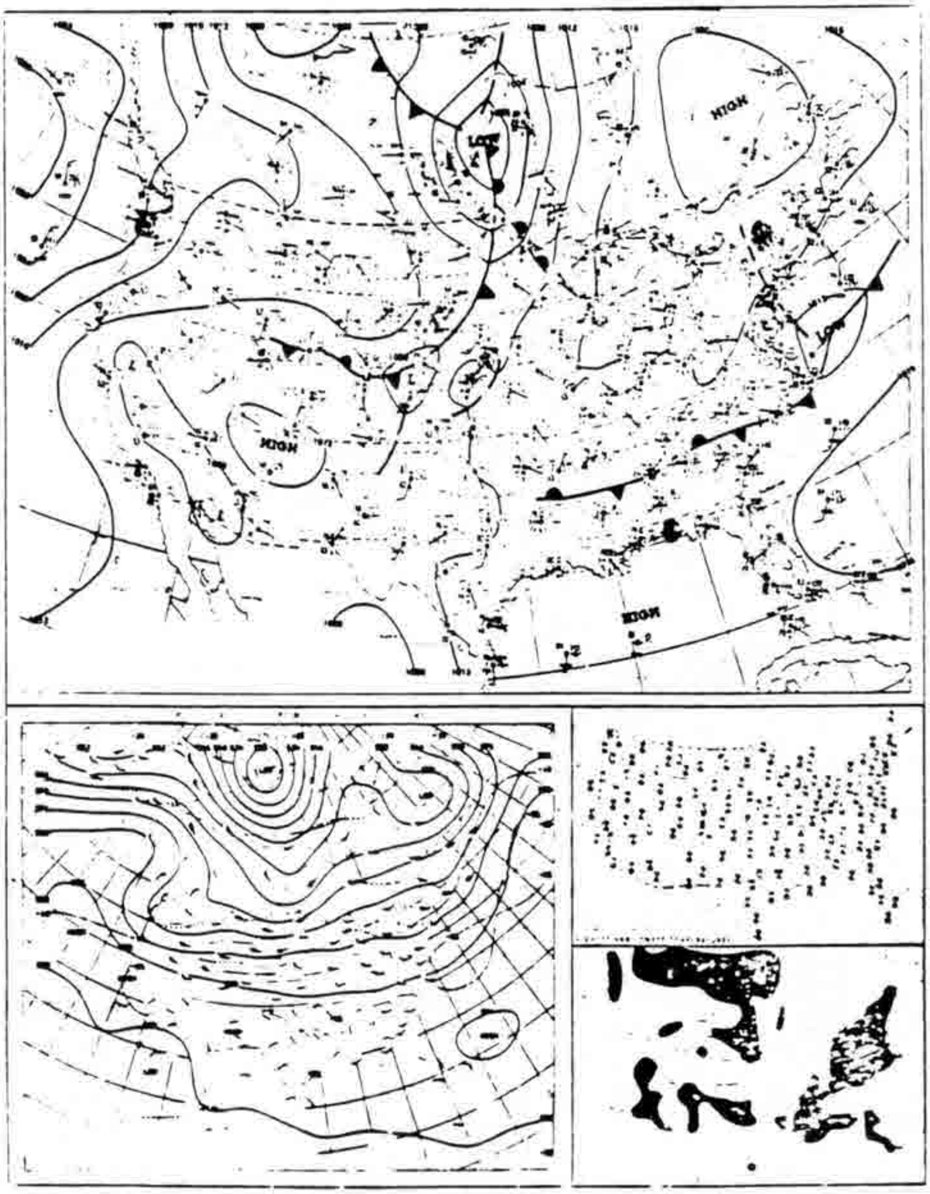

Figure 3.7: Synoptic conditions 6 August 1100 UTC.

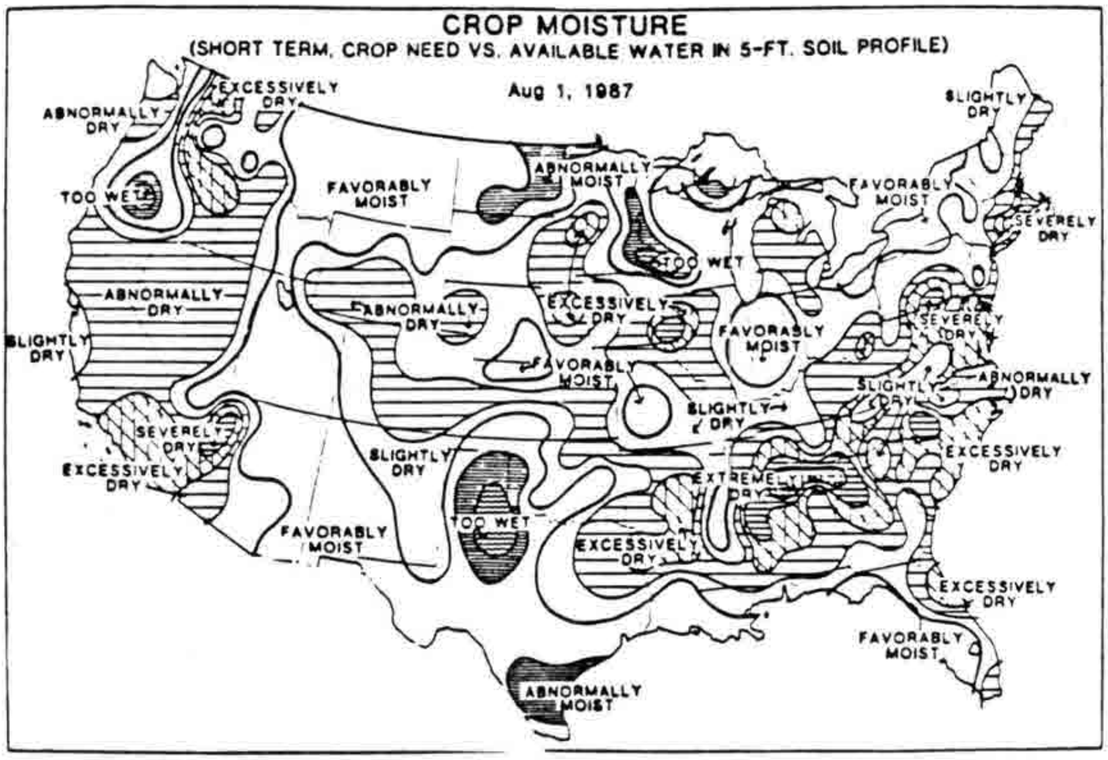

Figure 3.8: Soil moisture for the case study region 1 August (from *Weekly Weather and Crop Bulletin*, 1987).

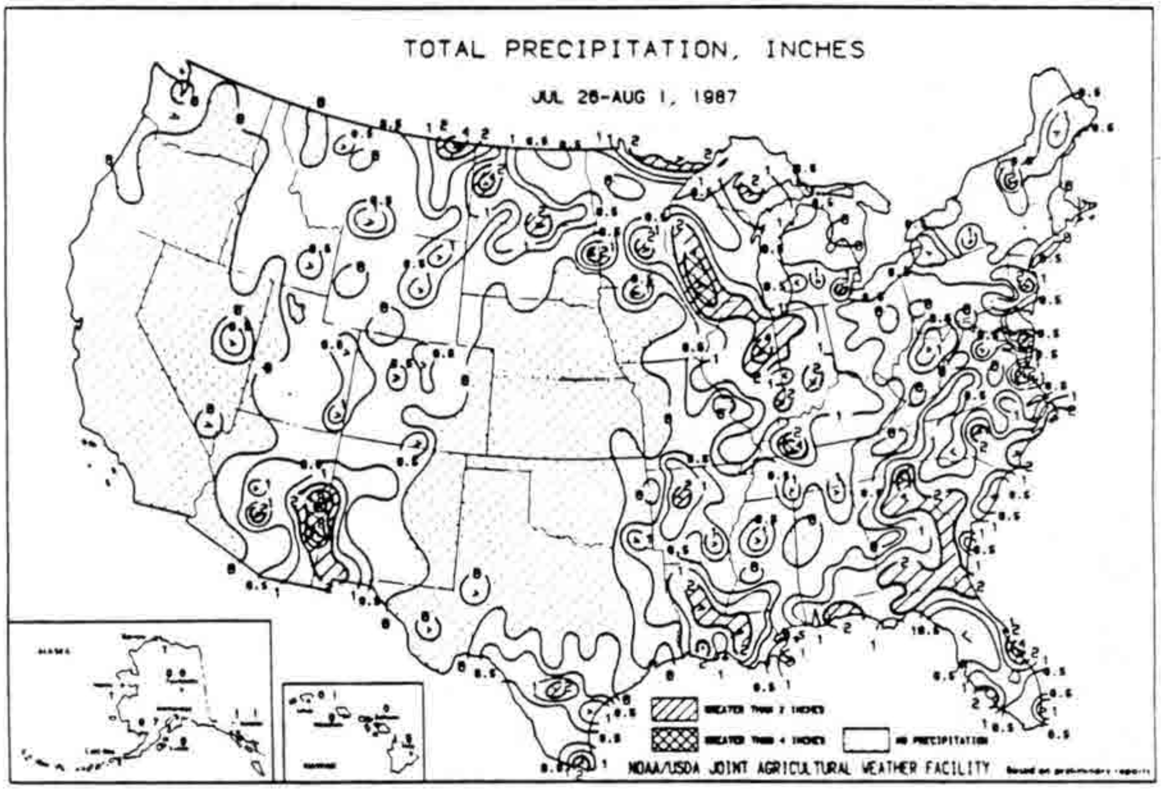

Figure 3.9: Total precipitation for the week of 26 July - 1 August (from *Weekly Weather and Crop Bulletin*, 1987).

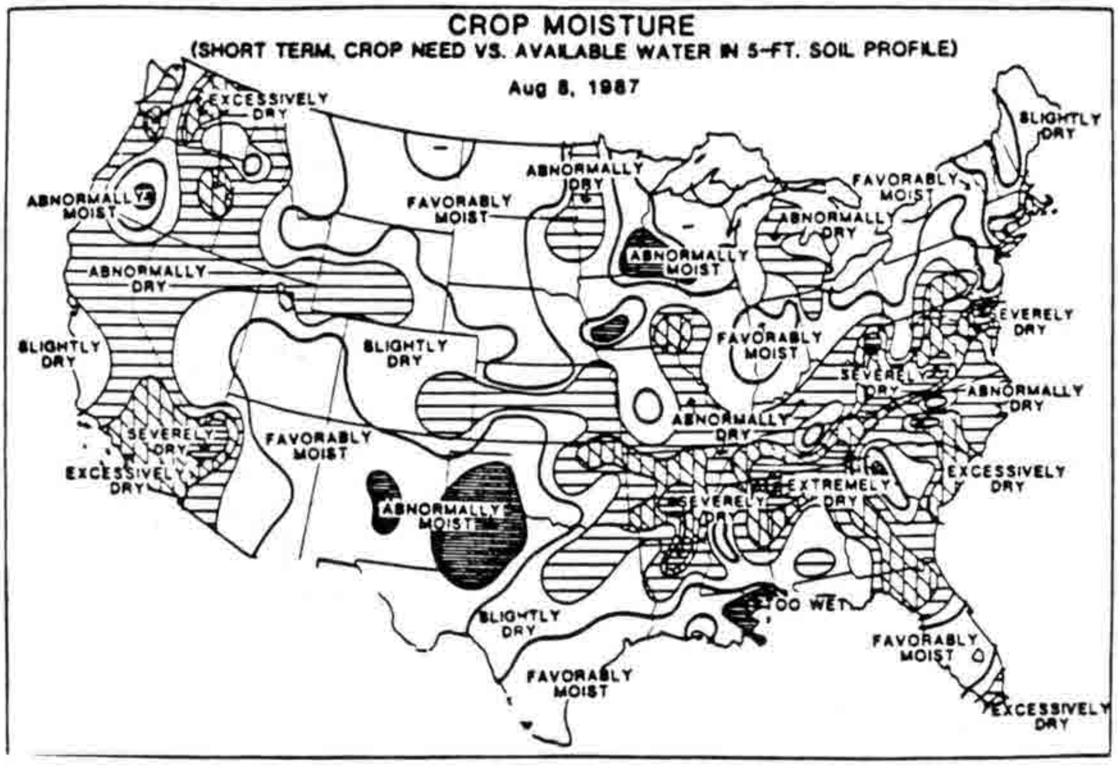

Figure 3.10: Soil moisture for the case study region 8 August (from *Weekly Weather and Crop Bulletin*, 1987).

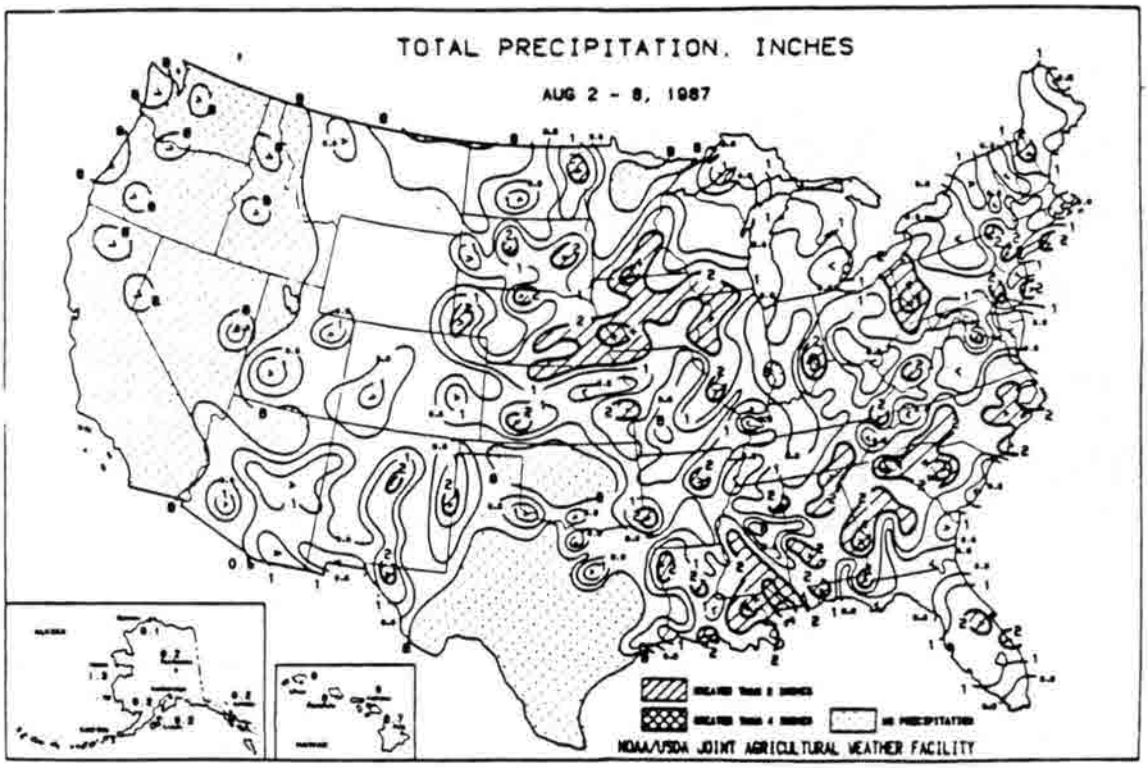

Figure 3.11: Total precipitation for the week of 2 August - 8 August (from *Weekly Weather and Crop Bulletin*, 1987).

GOES-7 (GOES-EAST), maintaining a geosynchronous orbit at the equator at an altitude of 35,800 km. The satellite used in this study, GOES-6, is commonly called GOES WEST due to its stationary longitudinal position at approximately 135° W. This position can vary depending on NOAA needs. During the time period of this study, the actual longitudinal position was at 134.35° W and was relatively stable.

The instrument on board the GOES-6 satellite used in this study is the Visible and Infrared Spin Scan Radiometer (VISSR) and when operated in dwell sounding mode it is known as the VISSR Atmospheric Sounder (VAS). The instrument is capable of measuring the upwelling radiance from the earth in the visible and in 12 infrared spectral channels from 3.9 μm to 15 μm. Table 3.2 adapted from Chesters and Robinson (1983) lists the spectral characteristics of the VAS channels. In normal VISSR mode, the visible and surface infrared channel, channel 8, are transmitted each half hour for the whole hemisphere. The FIRE data was transmitted in VISSR mode. Channel 8 is a surface channel with a high sensitivity to the surface as the atmospheric weighting function, $d\tau/d\ln p$, for channel 8 in Figure 3.14 indicates. The other VAS channels are used for sounding retrievals since their weighting functions peak at a higher level in the atmosphere.

The instrument is actually several detectors combined. The visible detector is a separate unit with 8 sensors which scan the earth West-to-East (W-E) in parallel. Three infrared sensors of multiple types with different field-of-views (FOVs) are used in conjunction with a selectable narrow-band filter creating a quite complex arrangement that is capable of several modes of operation (Clark, 1983). The instrument scans the earth by moving a mirror in the north-to-south (N-S) direction in angular increments of 0.192 mrad as the satellite spins at 100 rpm about its axis which is perpendicular to the earth's equatorial plane. The sampling rate for the infrared data is 8 μs, which produces 3822 elements for each line of data, and for the maximum mirror steps there are 1821 lines, which result in hemispheric coverage of approximately $\pm 70°$ in longitude with respect to the satellite subpoint. The visible data with its 8 sensors has a possible 14568 lines and elements. The visible resolution at nadir is 0.9 km and channel 8 has a nadir resolution of 6.9 km. During the scanning process the E-W direction is over sampled, which results in 4 $\times$ 8 km rectangular FOVs.

Table 3.2

Table 3.2: VAS instrument characteristics (GOES-6) (adapted from Chesters and Robinson, 1983).

VAS channel number	Central wavelength (μm)	Weighting function peak (hPa)	Absorbing constituent	single sample noise values * (K)
1	14.73	40	CO_2	3.1
2	14.48	70	CO_2	2.0
3	14.25	150	CO_2	1.4
4	14.01	450	CO_2	1.0
5	13.33	950	CO_2	0.5
6	4.525	850	CO_2	0.4
7	12.66	surface	H_2O	0.6
8	11.17	surface	window	0.2
9	7.261	600	H_2O	1.6
10	6.725	400	H_2O	1.0
11	4.444	500	CO_2	1.8
12	3.945	surface	window	0.3

*VAS large field of view sensor

An example of the VISSR infrared imagery for clear sky conditions over the case study region is shown in Figure 3.12. A cloudy case as observed by the visible sensor in Figure 3.13 shows how much better the resolution is for the visible compared to the infrared imagery.

The pre-launch noise specifications were originally given in terms of Noise Equivalent Radiance Differences but are listed in Table 3.2 as Noise Equivalent Temperature Differences (NEΔTs). The absolute accuracy of the VISSR infrared data is $\pm$ 1.5 K.

The VISSR data is navigated using the CSU Interactive Research Imaging System (IRIS) based on the automatic navigation parameters the satellite transmits to the ground-station which are updated daily. The apparent navigation error during the case study was ± 2 pixels for the infrared imagery which roughly corresponds to ± 14 km.

3.3 SSM/I INSTRUMENT DESCRIPTION

The Special Sensor Microwave/Imager (SSM/I) on the Defense Meteorological Satellite Program (DMSP) F8 satellite was launched June 1987 in a sun-synchronous near-polar

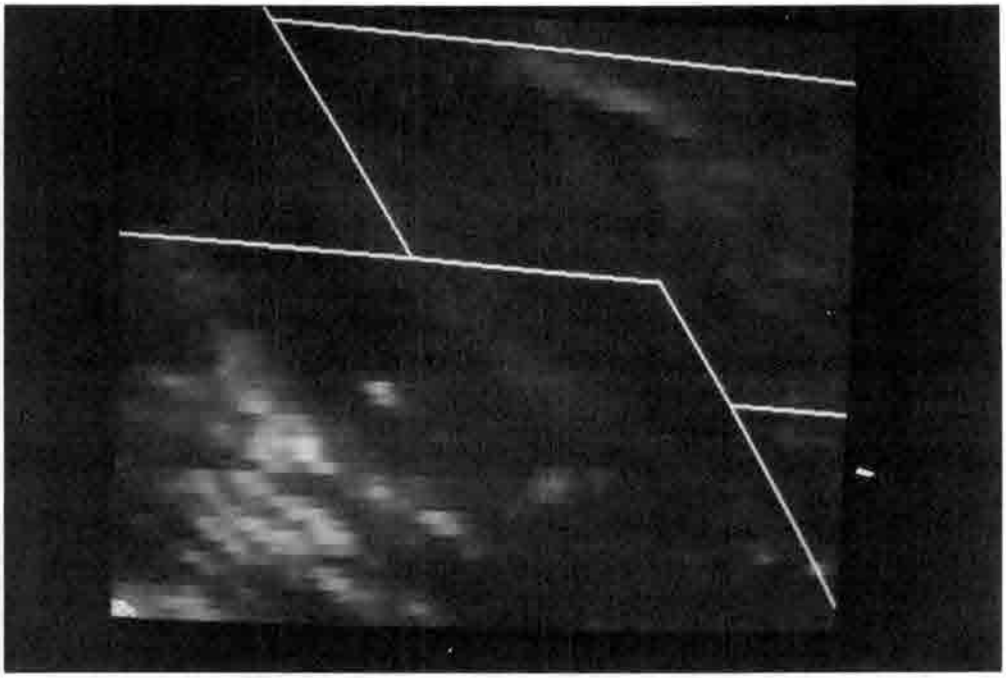

Figure 3.12: An example of VISSR infrared imagery over the case study region for clear sky conditions.

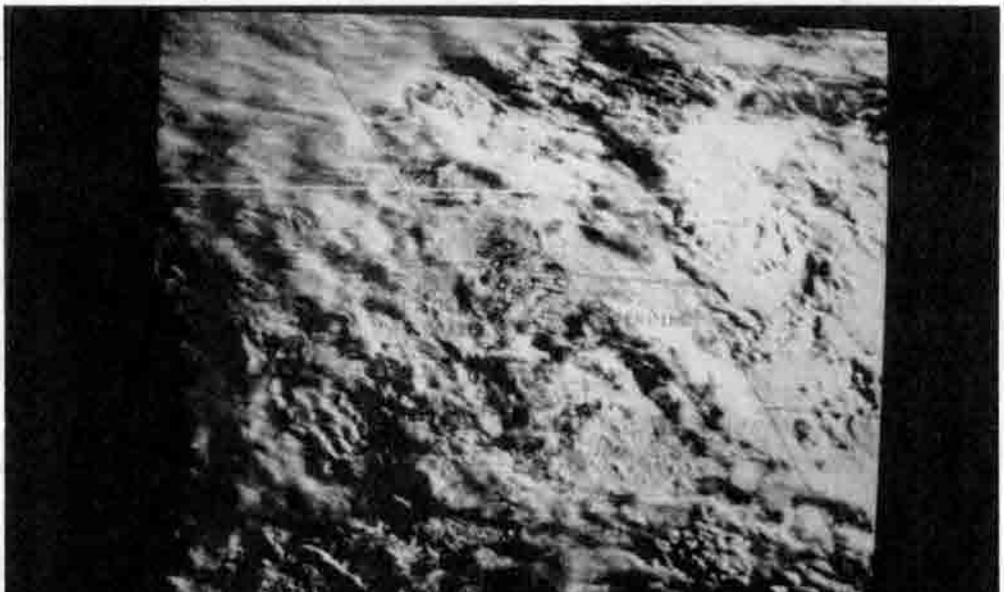

Figure 3.13: VISSR visible imagery over the case study region for cloudy conditions.

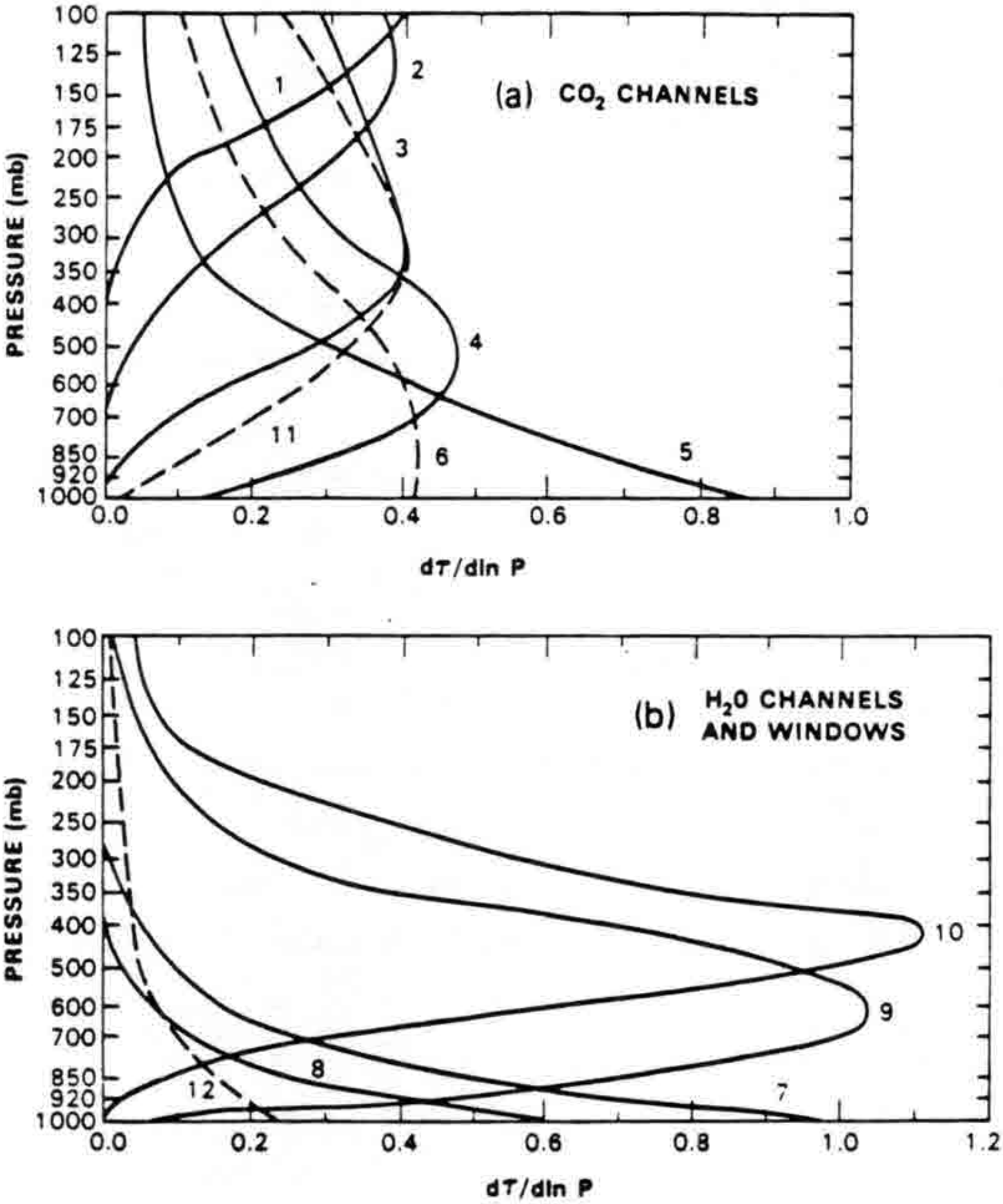

Figure 3.14: Comparison of VAS CO_2 sounding channel atmospheric weighting functions with VAS channel 8 (from Montgomery and Uccellini, 1985).

orbit at an altitude of 833 km with a period of 102 minutes. The orbit equator crossing times are approximately 0612 local time and has an orbit inclination of 98.8° which allows for twice daily coverage poleward of 50° latitude (Hollinger *et al.*, 1987).

The instrument consists of an offset parabolic reflector which is 61 cm × 66 cm in size and is mounted on a rotating drum which also contains the feedhorn and various supporting electronics. The simultaneous rotation of the feedhorn assembly with the reflector is an improvement over earlier microwave imaging systems such as the Scanning Multichannel Microwave Radiometer (SMMR) which had a fixed feedhorn assembly. The simultaneous rotation allows for more accurate polarization measurements since the direction of polarized radiation with respect to the feedhorn is the same as the feedhorn rotates with the reflector. The SMMR data must have polarization corrections made to overcome this problem (Njoku, 1980). The SSM/I has four frequencies (19.35, 22.235, 37.0, and 85.5 GHz) and dual polarization capabilities on all except the 22.235 GHz frequency which records only the vertical polarization (see Table 3.3). The data is collected during the rearward 102° portion of the instrument rotation which results in a conical scanning pattern 1394 km wide (see Figure 3.15). The conical scanning pattern has a constant zenith angle of 53.1°, eliminating changing limb effects due to varying zenith angle. Since the instrument uses the same antenna for the various channels, the effective-field-of-view (EFOV) of the sensor varies with frequency, with the highest frequency, 85.5 GHz, having the highest resolution. The resolutions given in Table 3.3 and shown schematically in Figure 3.16 are for the 3 dB (half-power) antenna beam widths. The data is sampled at 64 positions (every 1.6°) per scan line (128 samples at 85.5 GHz) with an integration time of 7.95 ms (3.89 ms at 85.5 GHz). Since the 85.5 GHz is of higher resolution, the lower resolution channels are sampled every other scan line with the 85.5 GHz channels being sampled for each line continuously. This pattern results is a sample resolution of 12.5 km × 12.5 km for the 85.5 GHz channels and 25 km × 25 km for the lower resolution channels.

The SSM/I data used in this study was collected at the Navy's Fleet Numerical Operations Center (FNOC) and was acquired through the Hughes Aircraft Company

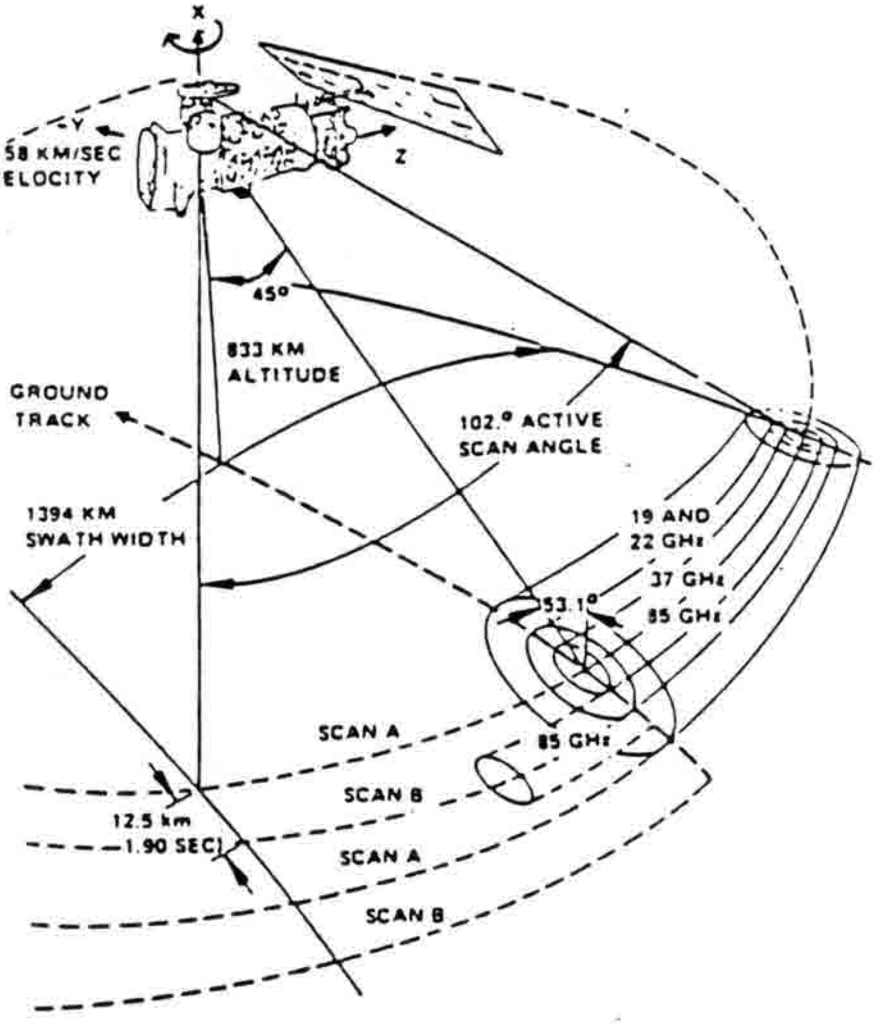

Figure 3.15: SSM/I conical scanning geometry (Hollinger *et al.*, 1987).

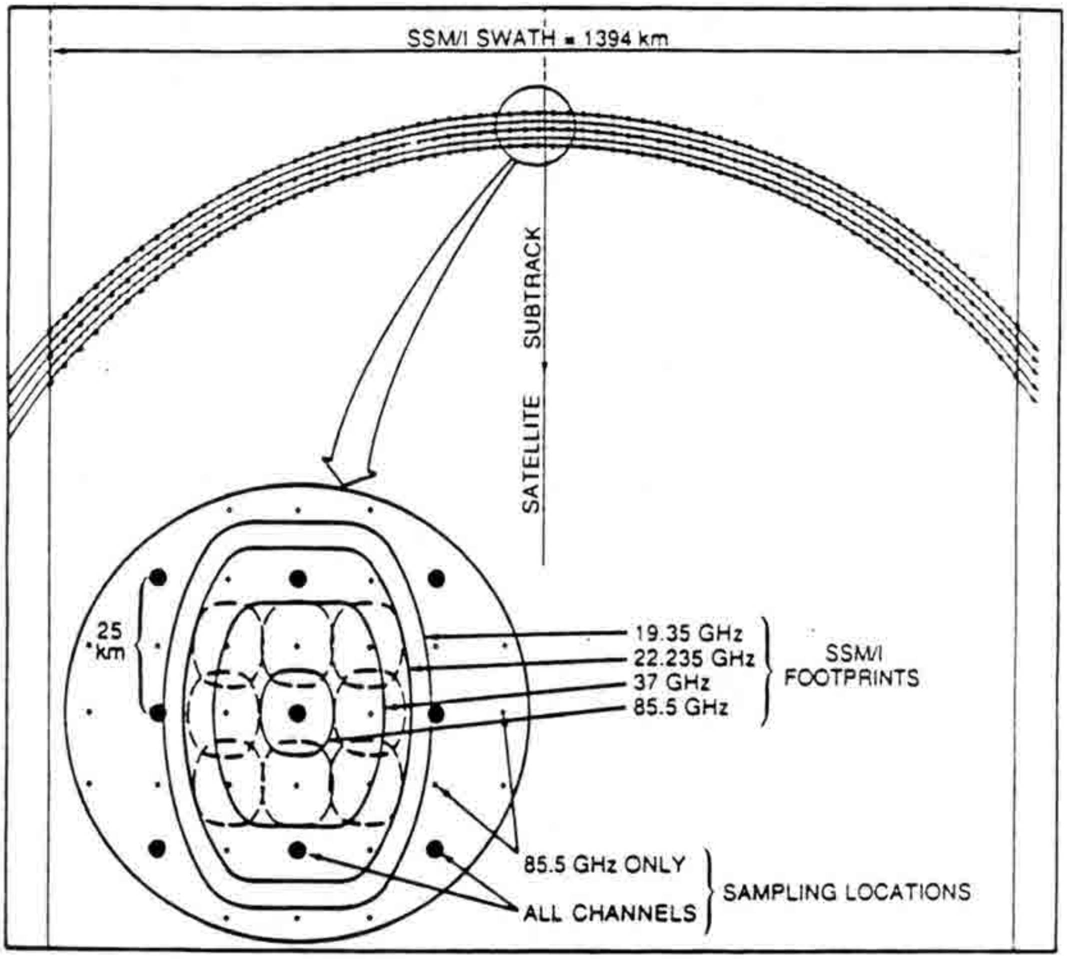

Figure 3.16: SSM/I field-of-view (FOV) (Spencer *et al.*, 1988).

Table 3.3

Table 3.3: SSM/I instrument characteristics (adapted from Hollinger *et al.*, 1987).

Channel number	Frequency (GHz)	Polar-ization (H or V)	Effective-field-of-view (EFOV) * (km)	Sensitivity ($NE\Delta T$)** (K)	Accuracy (K)
1	19.35	V	70 × 45	0.45	1.5
2	19.35	H	70 × 45	0.42	1.5
3	22.235	V	60 × 40	0.74	1.5
4	37.0	V	38 × 30	0.37	1.5
5	37.0	H	38 × 30	0.38	1.5
6	85.5	V	16 × 14	0.69	1.5
7	85.5	H	16 × 14	0.73	1.5

*3 dB limits.

**Average of laboratory measurements.

Space and Communications Group which designed and tested the SSM/I sensor. The raw data is processed by several algorithms which provide antenna corrections for the calibrated sensor brightness temperatures and navigation parameters which will not be explained in detail here (for more information see Hollinger *et al.*, 1987). The SSM/I data used was in the final calibrated form of the sensor brightness temperatures known as Sensor Data Record (SDR) files. The navigation for each data location was assigned at FNOC from the satellite ephemeris data.

3.4 CO-LOCATION OF SATELLITE DATA SETS

The SSM/I data was remapped to the GOES projection for intercomparison of the data sets. Due to lower resolution (fewer pixels) of the SSM/I data, it is more efficient to go to the GOES projection. Navigation of the SSM/I data was observed to have a bias of approximately 30 km in the direction of the satellite's motion. All data was corrected for this error by calculating new latitude and longitude values taking the shift into consideration. Verification of the navigation is possible due to the large land/ocean surface emittance contrast which allows coastal boundaries to be distinguished extremely well. The corrected navigation is accurate to ±15 km (±2 GOES pixels).

A point to remember when comparing the satellite data sets is the different zenith angles of the satellites. The SSM/I data has a constant zenith angle of 53.1° and the GOES data has a zenith angle range of 51° to 61° for the domain of the case study. For the entire region the GOES zenith angle was assumed to be the same as that at the center of the case study area which has a zenith angle of 55.8°. The maximum limb effect variations for the domain's zenith angle range for channel 8 is approximately 0.2 K which is of the same magnitude as the instrument precision of 0.2 K. Thus the assumption of a constant zenith angle over the small case study region is therefore a reasonable one.

3.5 CLASS SOUNDINGS

Special upper air soundings were obtained for the CINDE project using fixed and mobile Cross-chain Loran Atmospheric Sounding System (CLASS) soundings. Five CLASS trailers from the National Center for Atmospheric Research (NCAR) were located in the CINDE area as shown in Figure 3.2 to provide a much higher spatial resolution than the normal NWS radiosonde network. The sounding profiles were obtained from Charles Wade at NCAR and were analyzed with the Research Sounding Analysis (RSANAL) package which produced smoothed soundings with values every 10 hPa. The CLASS soundings supplemented the National Weather Service (NWS) radiosonde network and provided the atmospheric profiles of temperature and water vapor mixing ratio necessary for the atmospheric transmittance calculations used in this study.

Chapter 4

MEASUREMENT OF SURFACE EMITTANCE

The estimation of the microwave surface emittance is necessary for the proper determination of the surface boundary conditions which are used in calculations of the total upwelling radiance. Accurate estimates of surface emittance are necessary for good retrievals of cloud liquid water as shown by Yeh and Liou's (1983) work discussed in Chapter 1. Other studies have correlated an Antecedent Precipitation Index (API) to the surface emittance and have shown correlations greater than 0.8 using the 19.35 GHz channel on the Nimbus-5 Electronically Scanned Microwave Radiometer (ESMR) (Blanchard *et al.*, 1981) and greater than 0.9 for the Nimbus 7 Scanning Multichannel Microwave Radiometer (SMMR) (Wilke and McFarland, 1986). Satellite derived API fields can be used as input into models which need soil moisture conditions for flood predictions and crop growth monitoring. Since soil moisture affects the surface energy budget it is is also an important parameter in meteorological models. Effects of variations in vegetation and soil moisture with regard to its impact on boundary-layer circulation patterns have been studied by Segal *et al.* (1988a) and Segal *et al.* (1988b) and they have found that spatial differences of vegetation and soil moisture are sufficient to set up mesoscale circulations similar to sea breezes.

The surface emittance retrieval method of Wilke and McFarland (1986) divided the microwave brightness temperature by the minimum air temperature for a nighttime overpass and the maximum air temperature for a daytime overpass, so that,

$$\epsilon_\nu = \frac{T_B}{T_a}, \tag{4.1}$$

where T_a is the atmospheric temperature. This assumes that the atmospheric transmittance is 1.0 and that the influence of clouds in negligible. For the SSM/I 85.5 GHz channels the atmospheric transmittance for the 1962 standard atmosphere is approximately 0.71. Transmittances for the SMMR channels used by Wilke and McFarland (1986) are approximately 0.88 and above under clear sky conditions.

A method used by Grody (1983) with the Microwave Sounding Unit (MSU), which has a set of sounding channels in the oxygen band (50.30 GHz, 53.74 GHz, 54.96 GHz, and 57.95 GHz), is to compare the surface channel to a lower sounding channel which is relatively unaffected by the surface. Theoretical calculations of microwave brightness temperature were made for 53 radiosonde reports available over the United States on a single day. In the calculations the brightness temperatures were calculated at the nadir viewing angle and at surface emittances of 0.6, 0.8, and 1.0. The brightness temperatures for the surface channel (50.30 GHz) and the lowest sounding channel (53.74 GHz) are plotted as a function of surface emittance in Figure 4.1. Based on Figure 4.1 and also including the zenith angle dependence a parametric equation is obtained relating the measured brightness temperatures at 50.30 GHz and 53.74 GHz to the surface emittance,

$$\epsilon_\nu = a_0(\theta) + a_1(\theta)T_{B_{\nu_1}} - a_2(\theta)T_{B_{\nu_2}}, \tag{4.2}$$

where $a_i(\theta)$ $(i = 1, 2, 3)$ are coefficients as a function of zenith angle and $T_{B_{\nu_1}}$ and $T_{B_{\nu_2}}$ are the brightness temperatures for the surface and lower sounding channels of the MSU instrument. At larger zenith angles however, the increased attenuation decreases the sensitivity of the surface channel to the surface emittance. Another problem noted by Grody was the poor resolution of the MSU data (110 km at nadir) which smoothed the results.

Results of the method applied to MSU data for 10 April at 2045 UTC and the radar summary chart for the same time period are shown in Figure 4.2. Values of surface emittance range from above 0.95 to values below 0.8. Some of the low values are due to cloud contamination. The attenuating effects of the clouds reduces the observed brightness temperature which is translated into lower surface emittance. The low surface emittance values are located along the Mississippi River and the Great Lakes region and a small area in Oklahoma which is associated with an area of intense radar echoes. The low emittance values in the Minnesota area are due to mid and high level clouds which were detected using infrared data.

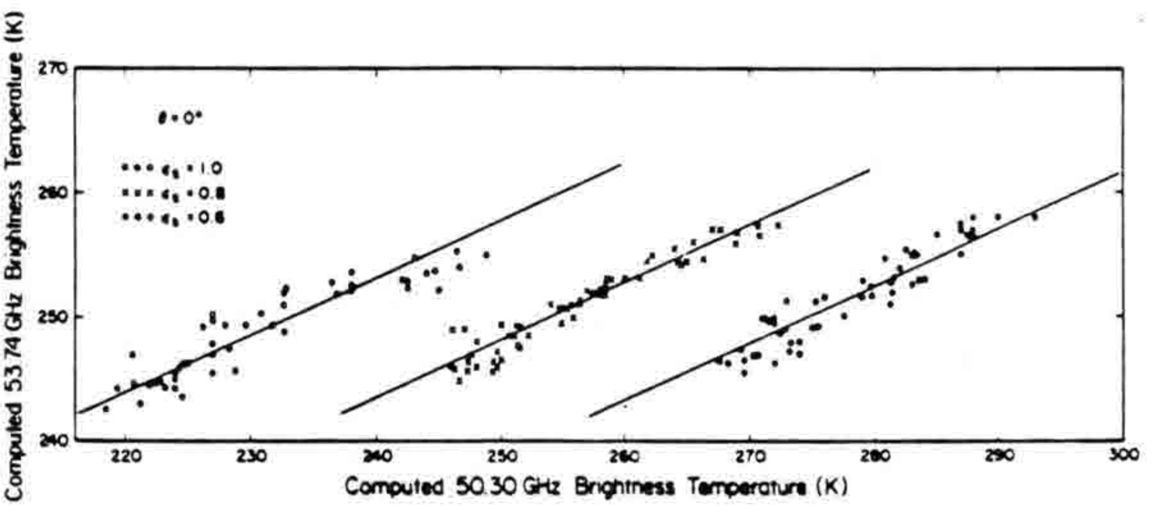

Figure 4.1: Comparison between the 50.74 GHz and 50.30 GHz computed brightness temperatures at nadir for surface emittances of 0.6, 0.8, and 1.0 (from Grody, 1983).

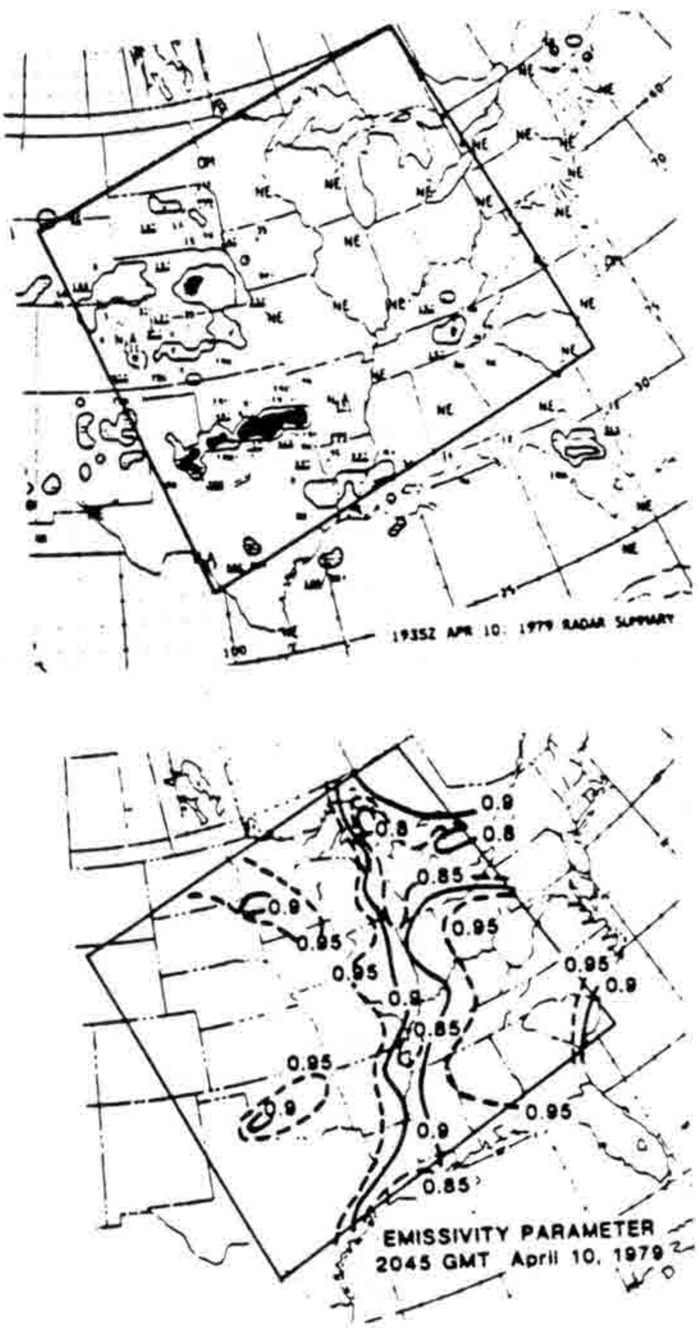

Figure 4.2: (a) Radar summary chart and (b) MSU derived surface emittance for 10 April at 2045 UTC (from Grody, 1983).

4.1 SURFACE EMITTANCE RETRIEVAL PROCEDURE

The surface emittance retrieval method used in this study employs co-located GOES VISSR infrared data in addition to the SSM/I microwave data. The infrared data is used to retrieve the surface skin temperature which is used in the radiative transfer calculation to determine the surface emittance given a microwave brightness temperature. As a simple example, consider a planet with no atmosphere, and a surface skin temperature from an infrared measurement of 300 K and a microwave brightness temperature of 270 . From the definition of emittance given in Chapter 2,

$$\epsilon_\nu = \frac{T_B}{T_{B_{\epsilon_\nu = 1}}}, \tag{4.3}$$

the surface emittance would 0.90. The same principle is used in the full surface emittance retrieval method except that atmospheric contributions due to water vapor and oxygen absorption must be accounted for, and care taken to avoid cloudy regions which significantly affect the infrared data.

4.1.1 Cloud Discrimination

The surface emittance is calculated only for clear sky conditions. The cloud free regions are determined from the GOES infrared and visible imagery using a simple thresholding technique. The thresholds were selected subjectively for each image using an interactive image display software package known as IM-4000 at CSU/CIRA on a VAX/II GPX. The thresholds were selected conservatively so that no significant cloud contamination is likely.

4.1.2 SSM/I Antenna Effective Field-of-view Adjustment

Once the cloud/nocloud determination was made using the visible and infrared data, the SSM/I data was checked to see if it was cloud contaminated within the microwave FOV. The EFOV of the SSM/I data in Table 3.3 is for the antenna beam's half-power limit. The area checked for cloud contamination for each SSM/I data point was expanded beyond the 3 dB EFOV limits to eliminate as much cloud influence as possible due to the microwave antenna's sensitivity to the area outside the 3 dB limits. As an example, the antenna pattern for the 85.5 GHz vertical polarization channel in Figure 4.3 has a strong center lobe with several smaller side lobes. The 3 dB EFOV limits include a large portion of the center lobe but exclude a significant portion of the sides of the center lobe. The possible cloud contamination by the sides of the center lobe was minimized by fitting the SSM/I antenna pattern with a spatial weighting function,

$$WF(x,y) = \begin{cases} \cos(\frac{\pi x}{3\ \mathrm{EFOV_x}}) + \cos(\frac{\pi y}{3\ \mathrm{EFOV_y}}), & \text{if } |x| < \frac{3}{2}\ \mathrm{EFOV_x} \text{ and } |y| < \frac{3}{2}\ \mathrm{EFOV_y} \\ 0, & \text{elsewhere,} \end{cases} \tag{4.4}$$

where x and y are the horizontal earth coordinates, and has a maximum value of 1 for the center point of the beam, decreases to 0.5 at the 3 dB EFOV limits given in Table 3.3 and then extrapolates the weighting function beyond the 3 dB EFOV limits to a zero value at 3/2 EFOV. This function was chosen as a crude fit to the actual antenna pattern in Figure 4.3.

4.1.3 Surface Skin Temperature Calculation

The surface skin temperature is calculated in the clear sky regions using the infrared data from the GOES VISSR instrument. Equation 2.31 from section 2.1.5 is solved for T_s to determine the surface skin temperature (Jones *et al.*, 1988). Equation 2.31 can be written more compactly as,

$$L_m = L_{sfc} + L_{atm}, \tag{4.5}$$

where the frequency dependence is understood, L_m is the measured radiance from the infrared surface channel, VAS channel 8, and L_{sfc} and L_{atm} are the surface and atmospheric contributions to the total upwelling radiance. The atmospheric contribution can be expressed more fully as,

$$L_{atm} = \int_{p_s}^{0} B_\nu[T(p)] \frac{\partial \tau_\nu(p,0)}{\partial p} dp. \tag{4.6}$$

Measurements of the atmospheric temperature and water vapor profiles from CINDE CLASS soundings are used to compute $\tau(p_s, 0)$ using VAS transmittance software received from the University of Wisconsin. The VAS transmittance software is a 40-level model based a set of polynomials which are functions of the temperature, water vapor, and zenith

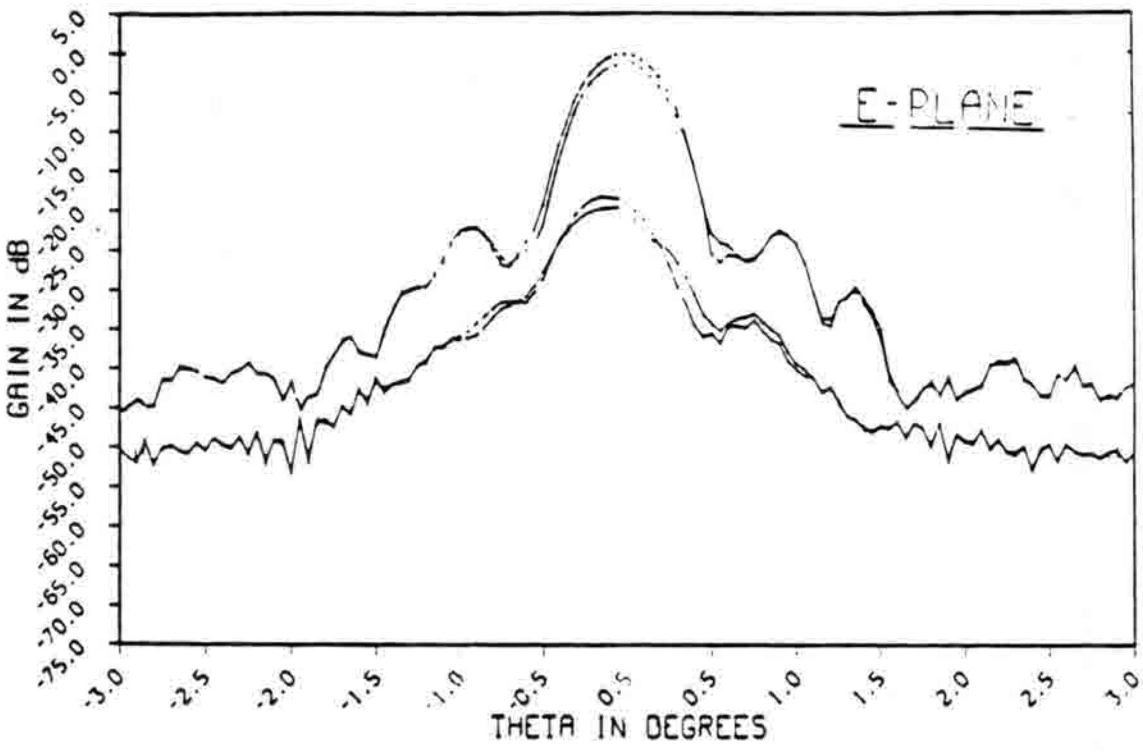

Figure 4.3: Antenna pattern for SSM/I channel 6 (85.5 GHz vertical polarization) (from Hollinger *et al.*, 1987).

angle (McMillin and Fleming, 1976; Fleming and McMillin, 1977). The atmospheric term, L_{atm}, is then calculated using the transmittances from the VAS transmittance software. The surface contribution,

$$L_{sfc} = B_\nu(T_s)\tau(p_s, 0), \tag{4.7}$$

is then solved for the surface skin temperature,

$$T_s = B_\nu^{-1}\left[\frac{L_m - L_{atm}}{\tau(p_s, 0)}\right], \tag{4.8}$$

where B_ν^{-1} is the inverse of the Planck function. The mean surface skin temperature, $\overline{T}_s$, for the microwave FOV is given by a weighted average of the retrieved skin temperatures within the SSM/I FOV,

$$\overline{T}_s = \frac{\sum WF(x,y)T_s(x,y)}{\sum WF(x,y)}, \tag{4.9}$$

where $WF(x, y)$ is given by Equation 4.4.

4.1.4 Surface Emittance Calculation

The surface emittance is calculated by solving the integrated microwave radiative transfer equation (Equation 2.40) for ϵ_ν, which results in,

$$\begin{aligned}
\epsilon_\nu = & \left\{L_\nu(0) - \int_{p_s}^{0} B_\nu[T(p)]\frac{\partial\tau_\nu(p,0)}{\partial p}dp\right. \\
& -[\tau_\nu(p_s,0)]^2\int_{p_s}^{0}\frac{B_\nu[T(p)]}{[\tau_\nu(p,0)]^2}\frac{\partial\tau_\nu(p,0)}{\partial p}dp \\
& \left.-[\tau_\nu(p_s,0)]^2 B_\nu(T_{space})\right\}\Big/ \\
& \left\{B_\nu(\overline{T}_s)\tau_\nu(p_s,0) - [\tau_\nu(p_s,0)]^2 B_\nu(T_{space})\right. \\
& \left.-[\tau_\nu(p_s,0)]^2\int_{p_s}^{0}\frac{B_\nu[T(p)]}{[\tau_\nu(p,0)]^2}\frac{\partial\tau_\nu(p,0)}{\partial p}dp\right\},
\end{aligned} \tag{4.10}$$

where $L_\nu(0)$ is the measured radiance from the SSM/I instrument. The remaining terms on the right hand side of Equation 4.10 are determined using Liebe's Millimeter-wave Propagation Model (MPM) and integrating the terms numerically.

4.1.5 Summary of the Surface Emittance Retrieval Method

Below is a brief outline of the surface emittance retrieval method. This process is repeated for each microwave channel.

- Remap SSM/I microwave imagery into the GOES satellite projection.
- Select cloud/nocloud thresholds using infrared and visible data from the GOES satellite.
- Determine the EFOV of the microwave channel and search for any cloud contamination within the EFOV. If cloud contamination exists, go on to next microwave data point.
- Within the microwave EFOV calculate the surface skin temperature using the GOES infrared data.
    1. Calculate $\tau(p_i, 0)$ $(i = 1, 40)$ using the CLASS sounding for the transmittance calculations.
    2. Compute L_{atm} using Equation 4.6.
    3. Calculate T_s using Equation 4.8.
- Determine the mean surface skin temperature within the EFOV using Equation 4.9.
- Compute the microwave atmospheric transmittance using the Liebe MPM model and the CLASS sounding.
- Calculate the surface emittance using Equation 4.10.

4.2 RESULTS

4.2.1 Composite Surface Emittance Values

Composite surface emittance values were calculated for the case study region due to clouds blocking the infrared FOVs causing incomplete coverage of the area for each time period. Cases 2, 3, 4, 6, and 8 were chosen to be composited together since Case 1 had no matching infrared data, case 5 had a significant time lag between the infrared and microwave data, and case 7 was almost completely overcast for the entire case study area. When more than one retrieval of the surface emittance was possible at one location the retrieved surface emittance values were averaged together.

Since the case 5 GOES infrared imagery was more than 2 hours later than the corresponding SSM/I data (see Table 3.1), the retrieved surface skin temperatures from the infrared data were too warm. In two hours the surface skin temperature can easily increase 10 K (Shih and Chen, 1984) which biases the surface emittance calculations. For case 5 the mean surface emittance retrieved for channel 7 was 0.917 while the mean for the composite time period was 0.949. Channel 6 had a surface emittance of 0.933 for case 5 while its composite mean value was 0.967.

The mean composite surface emittance values in Table 4.1 range from 0.940 for channel 2 to 0.976 for channel 1. Channels 1 and 2 at 19.35 GHz are more polarized than the channels at higher frequencies. Defining the fractional emittance polarization of a channel by,

$$P \equiv \frac{\epsilon_h}{\epsilon_v}, \tag{4.11}$$

where ϵ_h is the horizontal polarization emittance and ϵ_v is the vertical polarization emittance and applying it to the SSM/I data (see Table 4.2) shows that the fractional polarization for the SSM/I data is frequency dependent. It was shown in Chapter 2 that for a Lambertian surface the surface emittance is independent of polarization. Since the surface emittance results exhibit a polarization difference, this implies that the surface in the case study area can not be considered perfectly rough. Results from the lower frequency SSM/I channels in Table 4.1 confirm this result. The frequency dependence of the fractional polarization is due to the relative roughness with respect to incident radiation wavelength (Ulaby, *et al.*, 1986). The irregularities of the rough surface appear smaller and thus smoother at the long wavelengths which decrease the fractional polarization with increasing frequency.

The surface emittance standard deviations in Table 4.1 show that the horizontally polarized channels appear to have consistently larger variability than the vertically polarized channels. This preferential variability is due to surface roughness effects. In Figure 4.4 field measurements at 21 cm (1.4 GHz) from Newton (1977) are plotted as a function of zenith angle and surface roughness. At a zenith angle of 50°, the horizontal brightness temperature range is larger than the vertical polarization brightness temperature range for variations in surface roughness while the effects of soil moisture affect vertical and horizontal polarizations approximately the same (see Figure 4.4). The result is larger

Table 4.1

Table 4.1: Summary of surface emittance retrieval results.

Channel number	Frequency (GHz)	Polarization (H or V)	Surface emittance mean	Surface emittance std. dev.
1	19.35	V	0.976	0.0128
2	19.35	H	0.940	0.0208
3	22.235	V	0.974	0.0152
4	37.0	V	0.965	0.0120
5	37.0	H	0.940	0.0183
6	85.5	V	0.967	0.0144
7	85.5	H	0.949	0.0192

Table 4.2

Table 4.2: SSM/I fractional surface emittance polarization.

Frequency (GHz)	fractional polarization
19.35	0.962
37.0	0.973
85.5	0.981

horizontal polarization surface emittance variability due to surface roughness variability. This is consistent with results by Choudhury *et al.* (1979).

4.2.2 Comparison of Retrieved Composite Surface Emittance to Precipitation and Irrigation Areas

Areas of irrigated croplands in the case study region are represented in Figures 4.5, 4.6, and 4.7. In Figure 4.5 the heaviest irrigation regions in Colorado are along the South Platte River, Arkansas River, and along the Front Range in the area bordered by Fort Collins, Greeley, and Denver. For the case study region in Kansas (see Figure 4.6) two irrigation areas are of interest: the northwest counties of Sherman and Thomas and the southwest region along the Arkansas River. The dots in Figure 4.7 represent center pivot

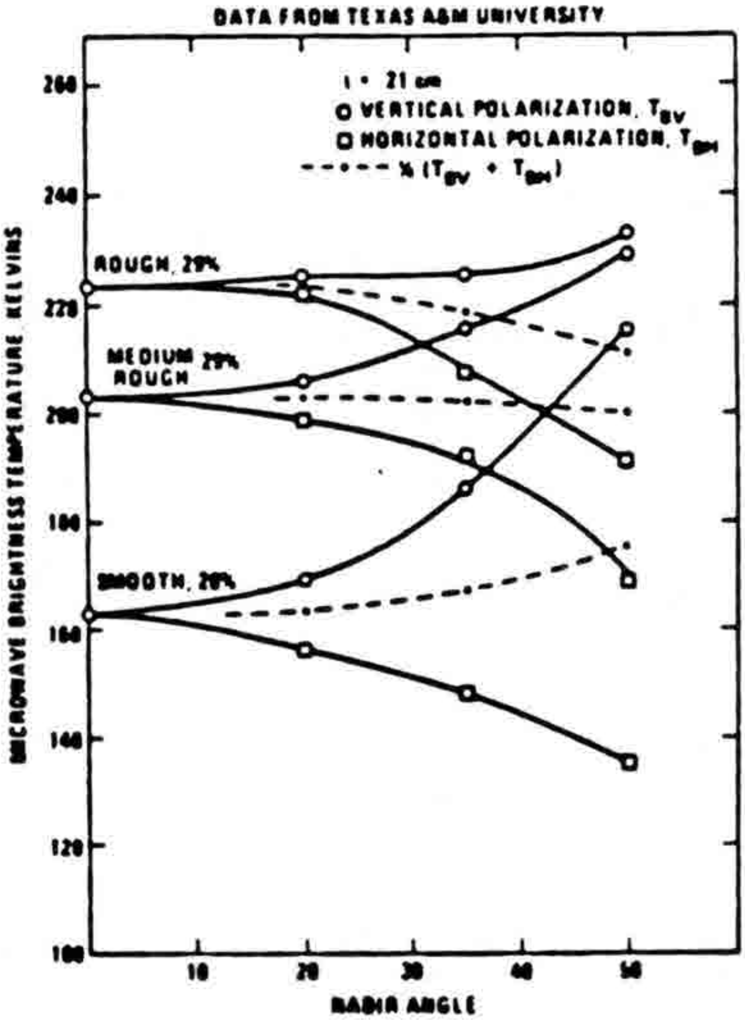

Figure 4.4: Microwave brightness temperature at 21 cm (1.4 GHz) versus zenith angle for different surface roughnesses (from Newton, 1977).

irrigation systems reported in Nebraska for 1985. The southwest corner of Nebraska along the South Platte is heavily irrigated as are sections along the North Platte.

The retrieved composite surface emittance results for channels 6 and 7 (85.5 GHz vertical and horizontal polarizations) are shown in image form in Figures 4.8 and 4.9 and in histogram form in Figures 4.10 and 4.11. The surface emittance results for SSM/I channels 1-5 are presented in histogram and image form in Appendix B. The color table used represents the low surface emittance areas as blue and as the surface emittance increases the colors progress through green, yellow, orange, red, pink, and white, where white represents a surface emittance of 1.0. The black colored areas were contaminated by clouds throughout the composite time period so that no surface emittance retrievals were possible.

The most prominent feature in Figures 4.8 and 4.9 is a region of low surface emittance ($0.88 < \epsilon_h < 0.92$) ($0.94 < \epsilon_v < 0.95$) in the Nebraska panhandle. There are two principal causes of this feature. The primary cause is due to a heavy precipitation event (> 50 mm (2 inches)) in this region in the afternoon of 3 August which wetted the surface significantly (see Figure 3.11). The secondary cause is irrigation in the region (see Figure 4.7) which occurs along tributaries of the North Platte River. Since irrigation is heavier along the North Platte and did not depress surface emittance values as much as the area in southwest corner of the Nebraska panhandle, the rainfall must have been the main contributor to the lower surface emittance values. Precipitation affected the extreme northeast corner of Colorado as well where the contrast is seen between dry (high emittance) land in Nebraska and Kansas and the more moist (lower emittance) land in northeast Colorado. However, since the precipitation was not as heavy, the effects are not as pronounced.

Irrigation did play an important role in the low surface emittance values observed in other regions. Low surface emittance values were retrieved over the heavily irrigated region near the Fort Collins-Greeley area along the Front Range. The 0.92 horizontal surface emittance contour at 85.5 GHz closely matches the outer boundary of the irrigation region. The low surface emittance values appear to extend farther west than the extent of the irrigation region. This is most likely due to the effects of lakes and reservoirs close

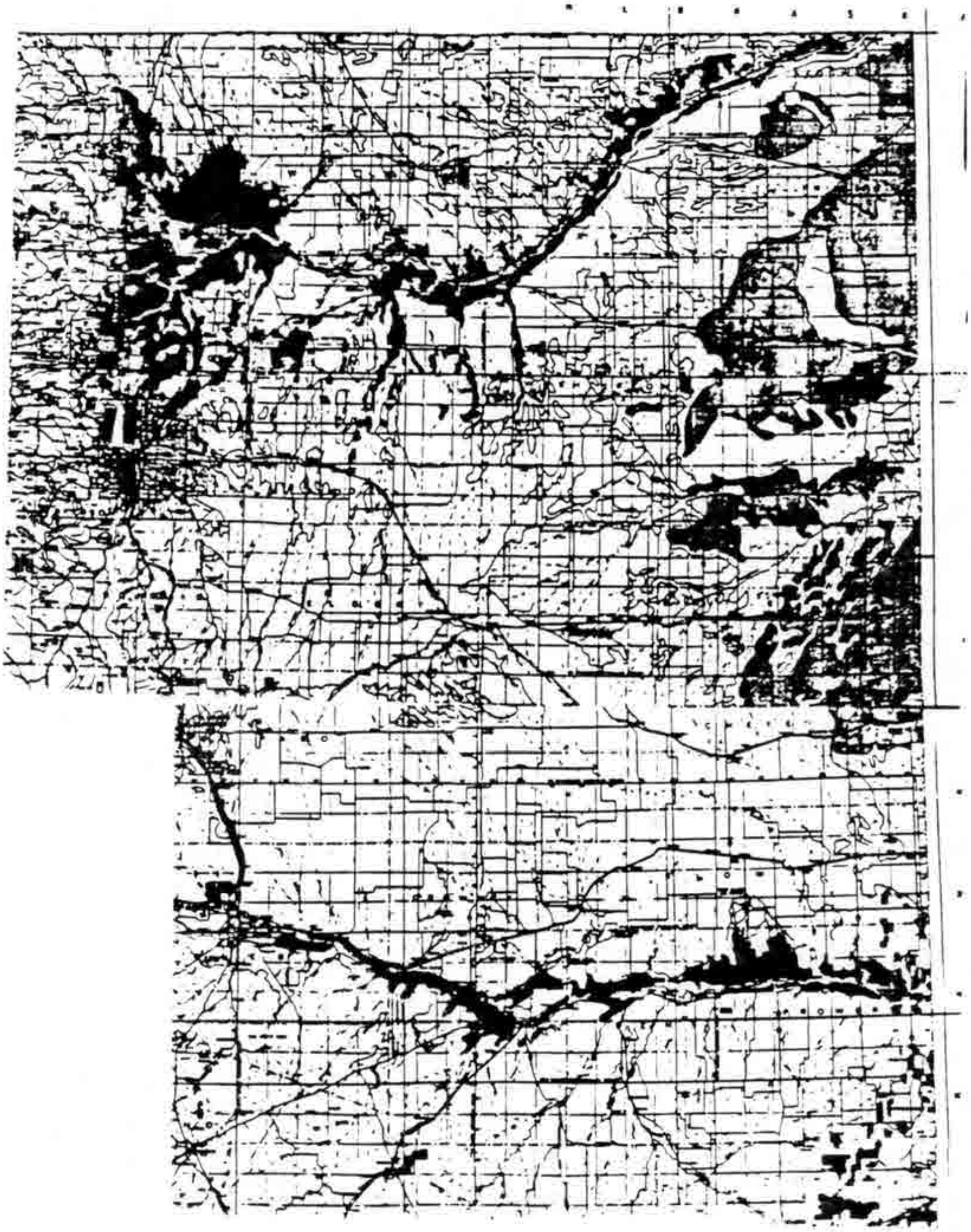

Figure 4.5: Irrigation areas in Colorado (from *Irrigated Croplands in Colorado*, 1980).

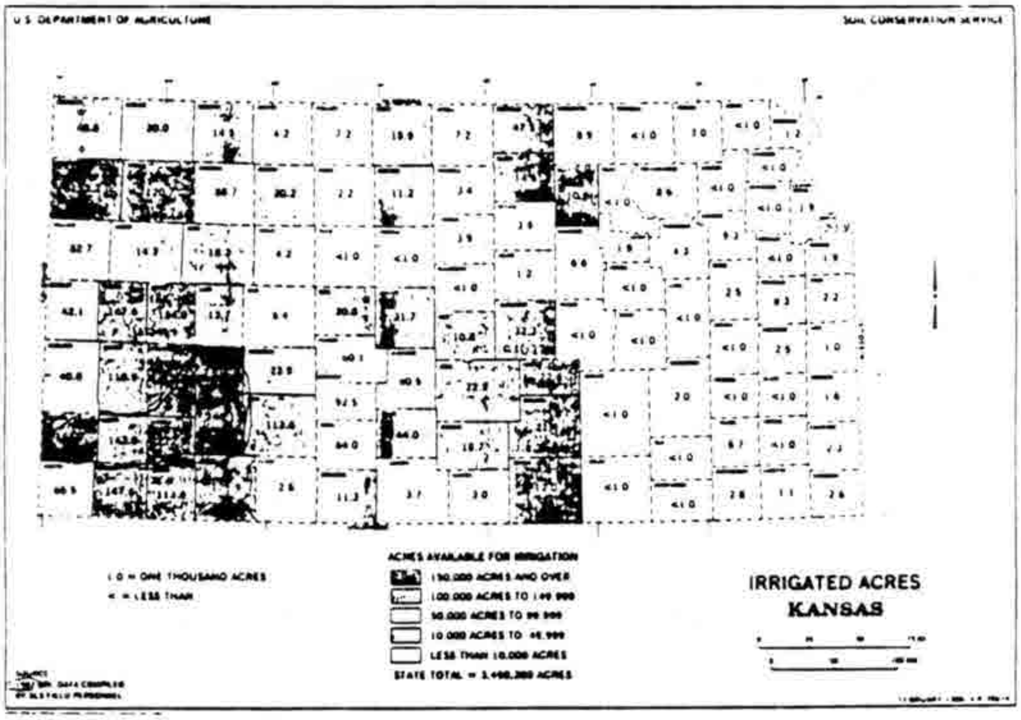

Figure 4.6: County acreage under irrigation in Kansas (from *Irrigated Acreage: Kansas*, 1986).

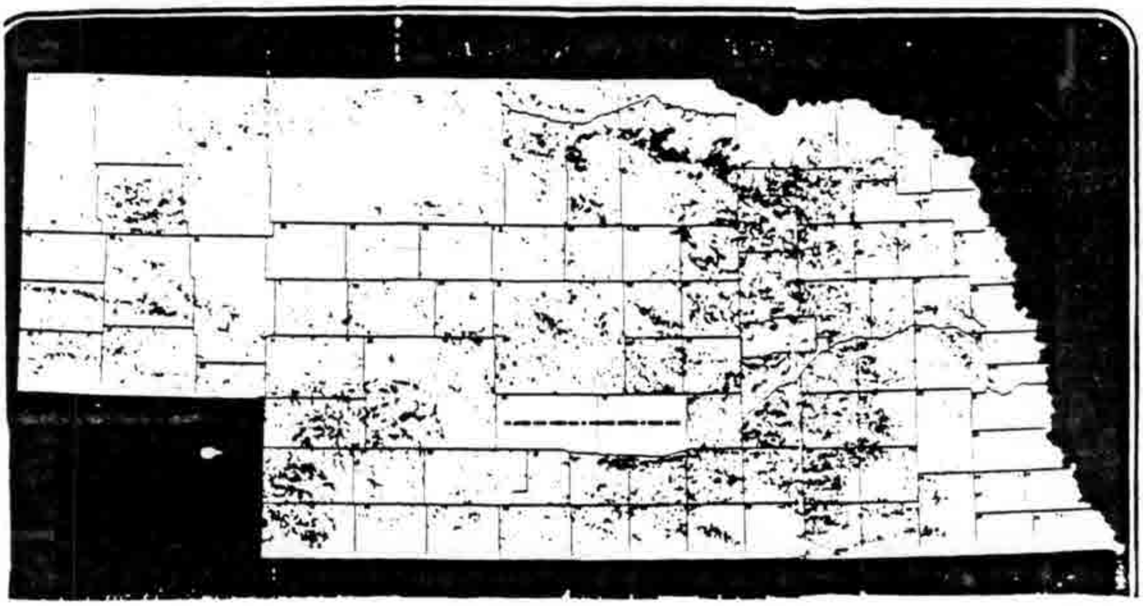

Figure 4.7: Center pivot irrigation systems in Nebraska, (1985).

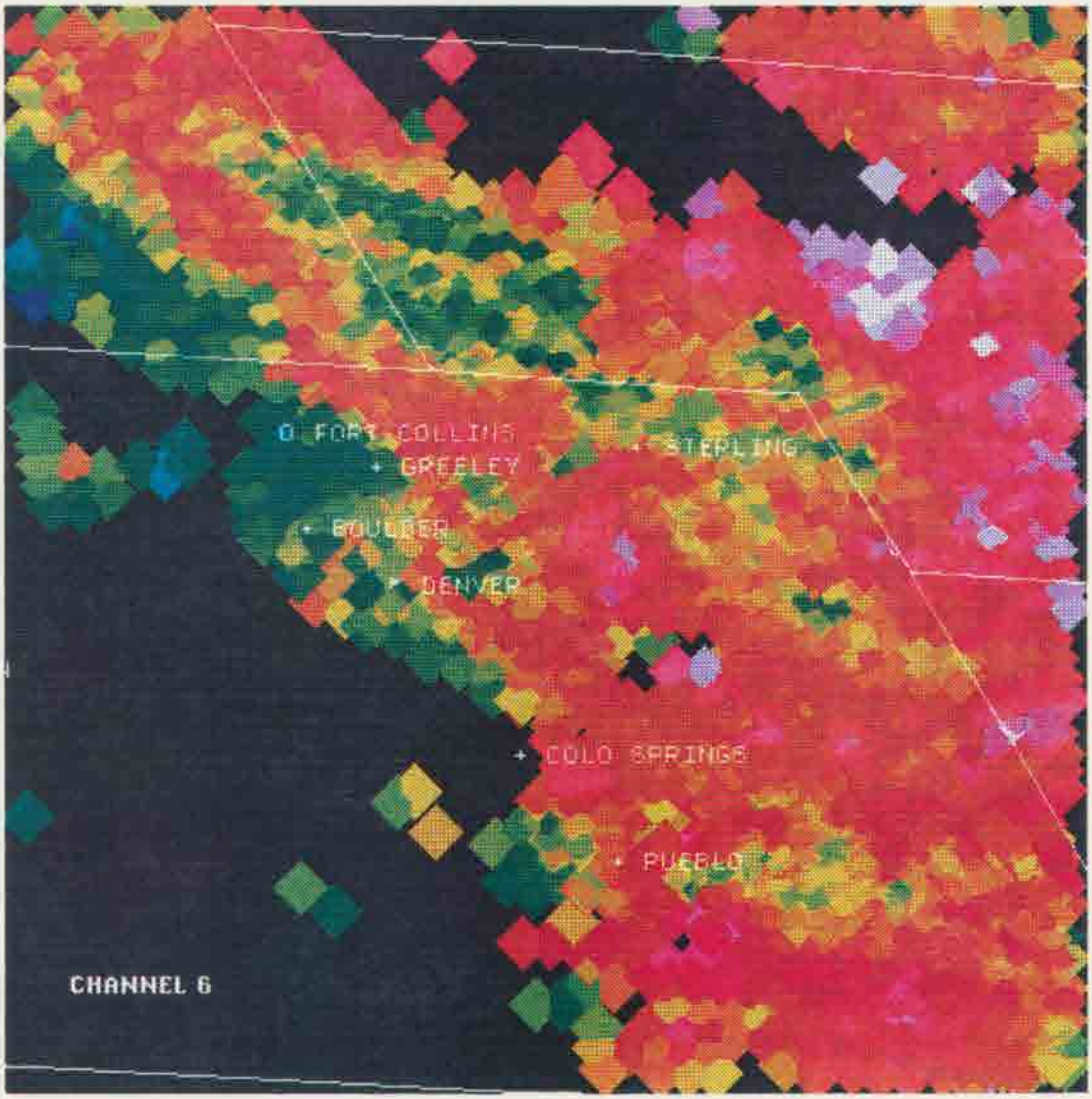

Figure 4.8: Composite surface emittance imagery for SSM/I channel 6 (85.5 GHz vertical polarization).

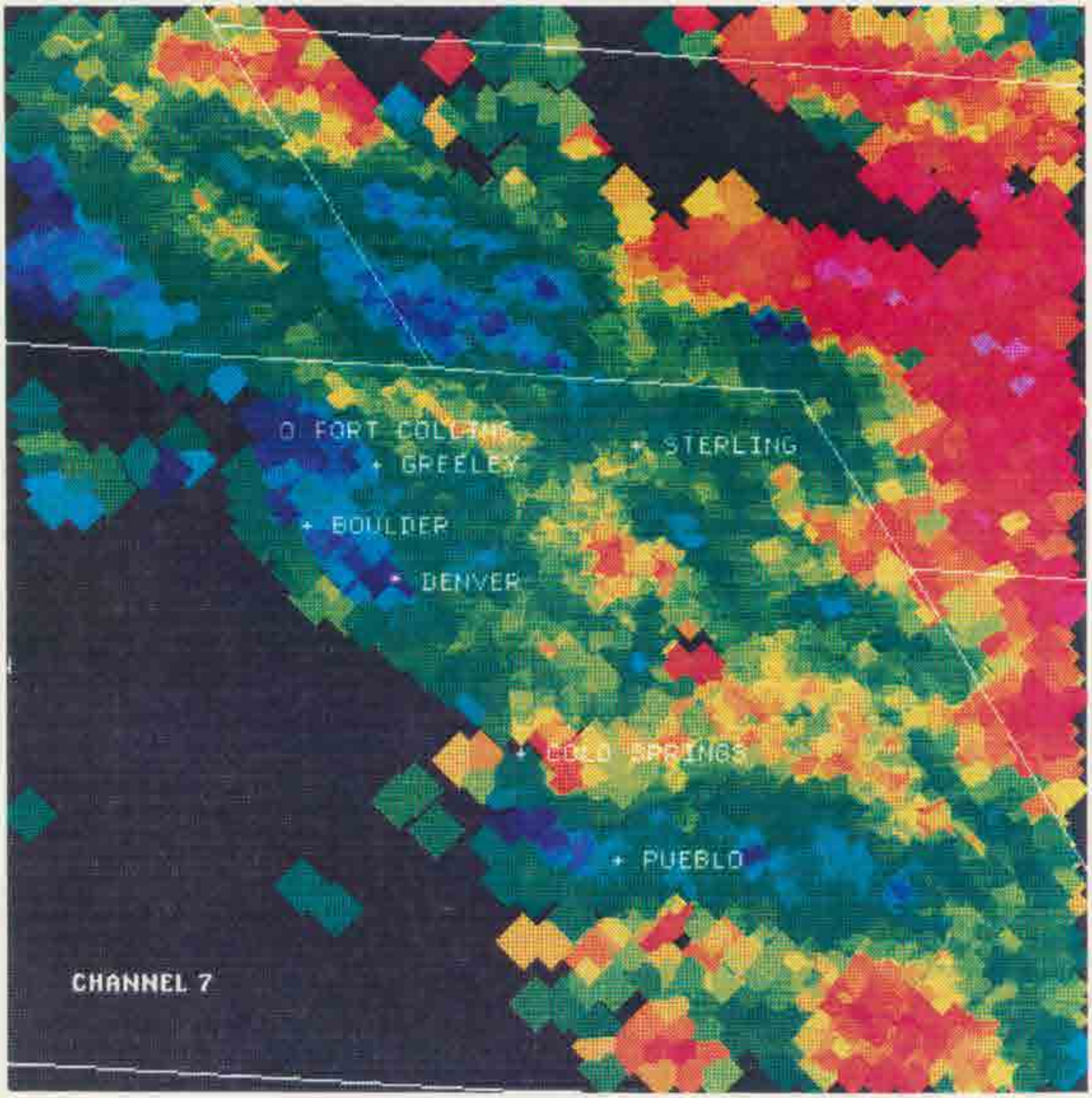

Figure 4.9: Composite surface emittance imagery for SSM/I channel 7 (85.5 GHz horizontal polarization).

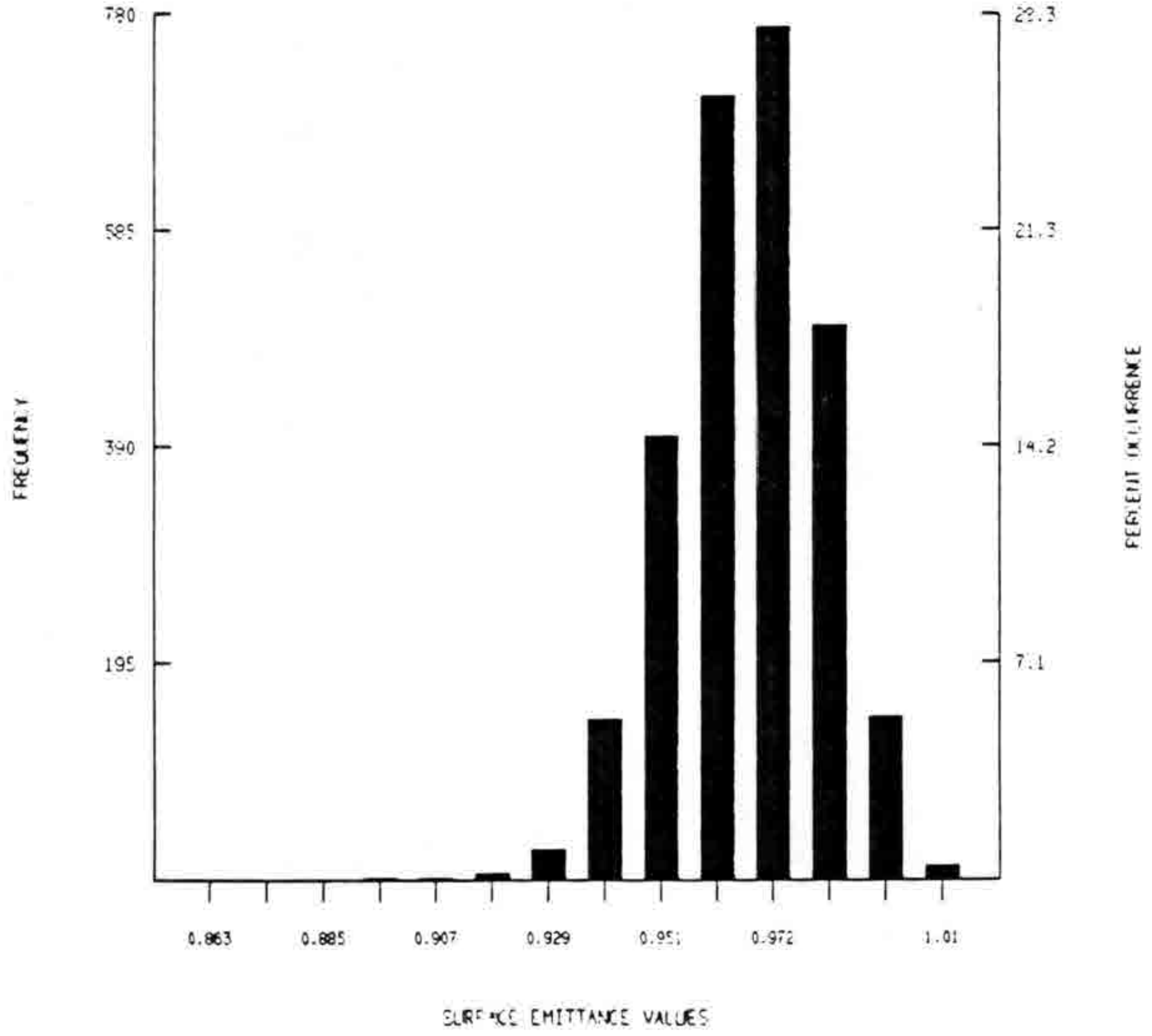

Figure 4.10: Composite surface emittance values for SSM/I channel 6 (85.5 GHz vertical polarization).

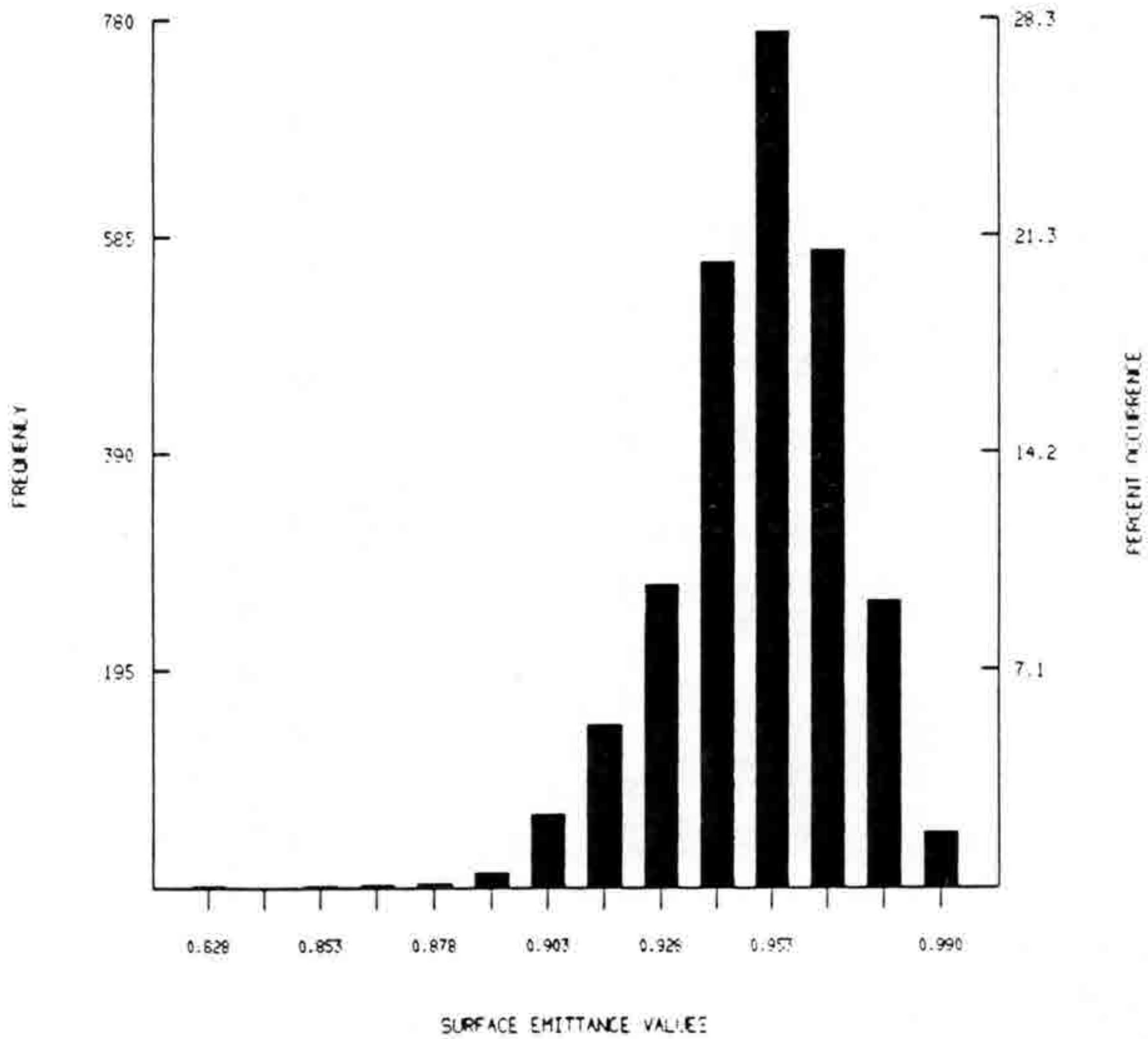

Figure 4.11: Composite surface emittance values for SSM/I channel 7 (85.5 GHz horizontal polarization).

to the foothills (*e.g.* Horsetooth Reservoir and Boyd Lake among many other smaller bodies of water) which depress the retrieved surface emittances with their low surface emittance property. Lake McConaughy in Nebraska on the North Platte River near the northeast corner of Colorado shows up extremely well as two FOVs with low surface emittance ($\epsilon_\nu \simeq 0.88$ for channel 7). Since the location of Lake McConaughy in the imagery remained very stable during the case study time period, the navigation for SSM/I data appears to have been adequately corrected. The river valleys of the North Platte, South Platte and the Arkansas River all show lower surface emittance values. Irrigation is limited to narrow bands along the rivers which diffuse the impact of the irrigated soil conditions. Conversely, the dry land areas of Kansas and Nebraska show high surface emittance conditions approaching unity. In the Kansas counties of Sherman and Thomas the small depression in the surface emittance values due to irrigation is surrounded by higher surface emittances from dry lands. A ridge of land known as the Palmer Lake divide extends into the plains from the Rocky Mountains just south of Denver, Colorado. Along the ridge are higher surface emittances due to drier conditions associated with the dryland pastures on the ridge.

4.2.3 Surface Emittance Retrieval Errors

In this algorithm no limit is placed on the maximum range of the retrieved surface emittance. Values as high as 1.01 were retrieved over Nebraska for SSM/I channel 3 (22.235 GHz vertical polarization). The remaining channels had maximum surface emittances near 0.99. Since 22.235 GHz is a water vapor absorption line, this suggests that the atmospheric transmittance at 22.235 GHz was underestimated. Initial profiles used in the calculation of the atmospheric transmittances were from the CINDE area near Denver, Colorado, thus it is reasonable to assume that the atmosphere over Kansas contained more water vapor, and that the calculated atmospheric transmittances used in the surface emittance retrieval were biased in that region. Lower elevation in Kansas also contributes to this bias.

In clear sky conditions the surface contributes a majority of the total upwelling radiance ($\tau(p_s, 0) \simeq 0.71$) which heavily links the retrieved surface emittance and the surface skin temperature. Since the same surface skin temperature is used in the retrieval process for all channels at a given location, any bias in the surface skin temperature would affect all channels similarly. Channel-to-channel biases must be due to the microwave brightness temperature biases and errors in the microwave transmittance algorithm. The microwave brightness temperatures are the most likely cause of channel-to-channel biases since the atmospheric component of the upwelling radiation is small (less than 1/4). Estimates of absolute brightness temperature errors are difficult even with co-located infrared data since the surface emittance has a wide range of reasonable values.

Numerical simulations were used to estimate errors in the retrieved surface emittances. A control case which had a surface emittance of 0.95 and the 1962 Standard Atmosphere (Valley, 1965) was used to determine the magnitudes of the retrieved surface emittance errors from induced perturbations. Simulated data was generated with various amounts of random noise added to several parameters which influence the retrieved surface emittances. The surface emittance was found to be the most sensitive to two parameters, the microwave brightness temperature and the surface skin temperature. The relative and absolute instrument errors of the VISSR and SSM/I instruments (see Tables 3.2 and 3.3) were used to calculate the propagation of error through the surface emittance retrieval algorithm (Beers, 1957). Results from the analysis in Table 4.3 show absolute accuracies ranging from 0.008 to 0.012. Frequencies with higher atmospheric attenuation have the largest errors (*e.g.* 22.235 GHz, and 85.5 GHz). In a physical sense, the high attenuation is obscuring the surface from view which makes it more difficult to measure the surface emittance accurately. The lower relative error at 37 GHz is due to the lower relative instrument noise at that frequency.

4.2.4 Summary of Surface Emittance Retrieval Results

The surface emittance retrieval algorithm used is a direct physical model which is capable of excellent results. The limitation of retrieval over clear sky conditions is problematic for many applications, but in the error analysis section the deterioration of results is directly linked to the decreasing radiometric contribution of the surface. The retrieval

Table 4.3

Table 4.3: Error sensitivity analysis for retrieved surface emittance.

Frequency (GHz)	Surface emittance errors relative	absolute
19.35	0.00206	0.00783
22.235	0.00408	0.00943
37.0	0.00198	0.00845
85.5	0.00530	0.01232

method is most accurate when the surface emittance has the largest influence on the radiation field.

Chapter 5

CLOUD LIQUID WATER RETRIEVAL

The SSM/I instrument offers unique possibilities for remote sensing of cloud liquid water. The high frequency channels at 85.5 GHz are much more sensitive to liquid water than previous channels on earlier sensors which had lower frequencies such as the Scanning Microwave Spectrometer (SCAMS) on Nimbus 6 and the Scanning Multichannel Microwave Radiometer (SMMR) on Nimbus 7. As an example, at the previous highest frequency on SMMR (37.0 GHz) the attenuation at 1013 hPa, and 15° C along a 20 km path length for 100% relative humidity due to water vapor is 0.975 dB while a liquid water content of 0.1 $g \cdot m^{-3}$ for the same conditions has an attenuation of 1.70 dB (Allen and Liebe, 1983). Thus the relative sensitivity of cloud liquid water versus water vapor from the ratio of the attenuations is 1.74. For the SSM/I 85.5 GHz channel the same conditions produce a water vapor attenuation of 2.34 dB and a cloud liquid water attenuation of 7.55 dB, which is a factor of 3.22. This means that the SSM/I 85.5 GHz channel is nearly twice as sensitive to cloud liquid water as the SMMR instrument and makes it an excellent tool to sense liquid water content in the atmosphere with minimal interference from other attenuating sources.

Cloud liquid water attenuates the microwave radiation emitted from the surface and emits the radiation at cooler brightness temperatures since its ambient temperature at a higher altitude is colder. Theoretical calculation of microwave brightness temperatures from Spencer *et al.* (1988) which use the Rayleigh approximation, a zenith angle of 53°, a surface emittance of 0.9, and a cloud base of 950 hPa show a cooling of the brightness temperature with increasing cloud liquid water content (see Figure 5.1). The colder temperatures associated with the higher cloud tops depress the brightness temperatures more which makes the brightness temperature more sensitive to cloud liquid water at higher levels.

5.1 CLOUD LIQUID WATER RETRIEVAL PROCEDURE

The cloud liquid water is retrieved by calculating theoretical brightness temperatures and comparing them to the observed brightness temperature measured by the SSM/I instrument for the 85.5 GHz channels. The surface emittance results from Chapter 4 are used to supply estimates of ϵ_ν used in the calculations of brightness temperature. The difference between the calculated and observed brightness temperatures is used to to make a new estimate of the cloud liquid water content. The cloud liquid water retrieval process ends once the calculated and observed brightness temperatures are within the instrument noise level. Retrieval of cloud liquid water is possible at any location which has an estimate of ϵ_ν and SSM/I 85.5 GHz coverage.

5.1.1 Discrimination of Precipitation

As discussed in Chapter 2, the Rayleigh approximation used in the calculation of cloud liquid water attenuation is valid only for non-precipitating clouds at millimeter wavelengths. Application of this method to precipitating clouds is therefore invalid and a method to detect precipitating clouds is necessary. Scattering of microwave radiation by precipitation has been studied as a method to retrieve rain rates over oceans and land (Spencer *et al.* 1983; Spencer 1986). Spencer *et al.* (1988) have recent results from the SSM/I instrument which indicate that a brightness temperature threshold of 255 K for the 85.5 GHz channels can discriminate between precipitating and non-precipitating areas. The threshold of 255 K is not meant to represent an absolute condition. Rain can exist at brightness temperatures below *and* above 255 K, but is more likely to exist below 255 K. Comparisons of SSM/I 85.5 GHz brightness temperatures below 255 K were shown to correspond well with radar echoes and aircraft data in several cases in Spencer *et al.* (1988). The scattering of the microwave radiation by large ice particles in the precipitating clouds depresses the brightness temperatures below 255 K and below 100 K in some instances. Retrieval of cloud liquid water is attempted only for 85.5 GHz brightness temperatures above 255 K.

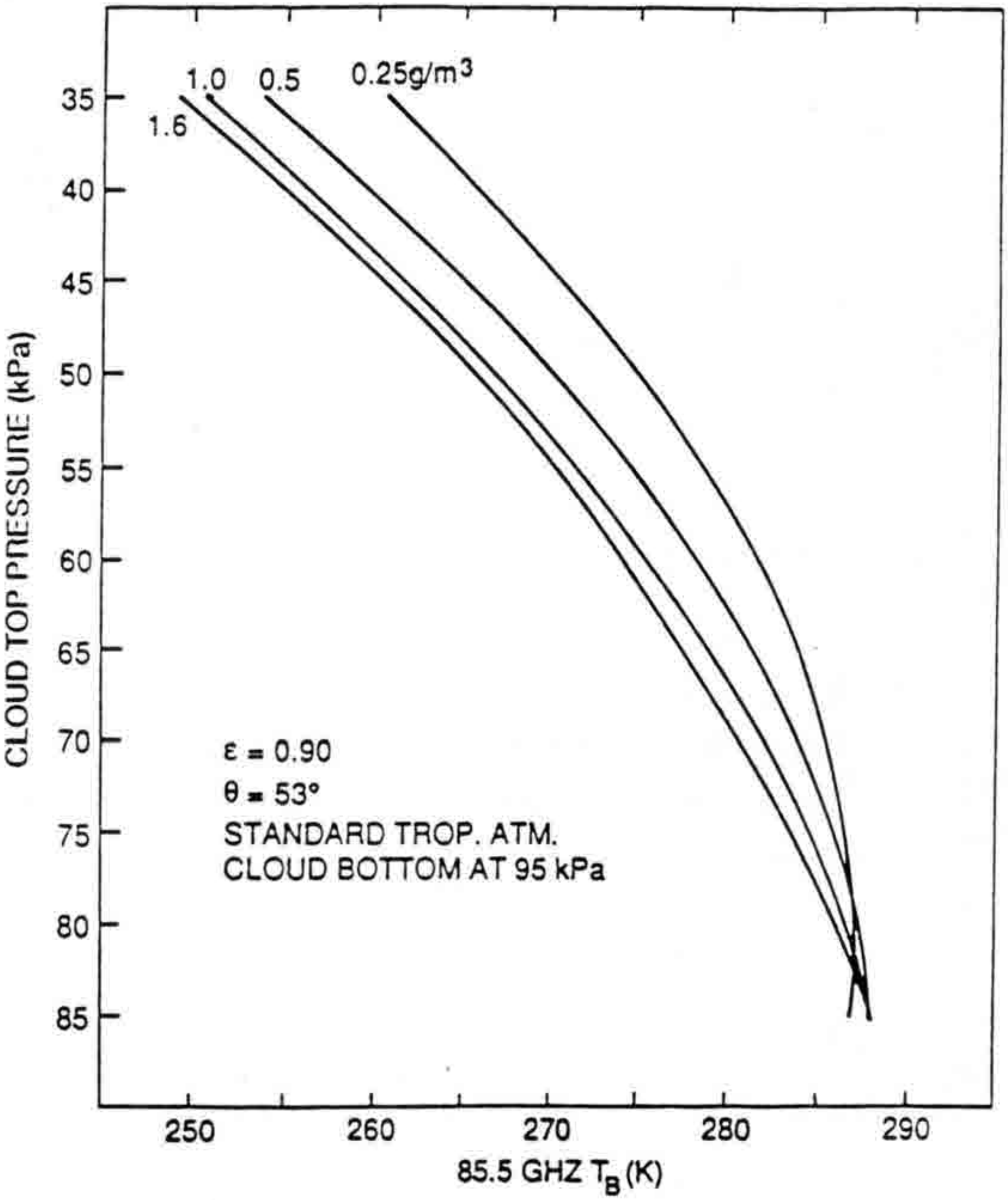

Figure 5.1: Brightness temperature as a function of vertical extent and cloud water content at 85.5 GHz. Calculations assume Rayleigh absorption, a zenith angle of 53°, a surface emittance of 0.9, and a cloud base at 950 hPa (from Spencer *et al.*, 1988).

5.1.2 Theoretical Calculation of Brightness Temperature

The theoretical brightness temperatures are calculated using,

$$\begin{aligned} L_\nu(0) &= \epsilon_\nu B_\nu(T_s)\tau_\nu(p_s,0) \\ &+ \int_{p_s}^{0} B_\nu[T(p)]\frac{\partial \tau_\nu(p,0)}{\partial p}dp \\ &+ (1-\epsilon_\nu)[\tau_\nu(p_s,0)]^2 \int_{p_s}^{0} \frac{B_\nu[T(p)]}{[\tau_\nu(p,0)]^2}\frac{\partial \tau_\nu(p,0)}{\partial p}dp \\ &+ (1-\epsilon_\nu)[\tau_\nu(p_s,0)]^2 B_\nu(T_{space}). \end{aligned} \tag{5.1}$$

which is the microwave integrated radiative transfer equation derived in Chapter 2 (Equation 2.40). The Liebe Millimeter-wave Propagation Model (MPM) is used to calculate the atmospheric transmittances. The surface emittance, ϵ_ν, is estimated from the composite surface emittance values calculated in Chapter 4, and the surface skin temperature, T_s, is assigned the value of the surface air temperature from the CINDE CLASS soundings.

5.1.3 Determination of Cloud Top and Base

The cloud top pressure is assigned using the infrared temperature and relating it to pressure using the atmospheric temperature profile used in the atmospheric transmittance calculations. The cloud base is set at the atmospheric sounding's lowest lifted condensation level (LCL), which is the saturation level for an air parcel when lifted from some initial level. The lowest LCL from a number of initial levels is used since it is not necessary that the parcel comes from the surface level to form a cloud base. The cloud top and base form the vertical limits on the location the cloud liquid water which is to be added in the retrieval process. The cloud which is generated in the retrieval process is assumed to have uniform vertical distribution of cloud liquid water content. This is an over simplification since (as presented in Chapter 1) Warner's (1955) work shows a definite vertical structure to the cloud liquid water content. However, with the microwave imaging channels the atmospheric weighting function characteristics are such that little if any vertical resolution is possible. Additional sounding channels, which are more opaque, are necessary to provide adequate vertical resolution.

5.1.4 Iteration Procedure

Initially the liquid water content is set to zero and a theoretical brightness temperature is calculated using Equation 5.1. The difference between the observed brightness temperature, $\tilde{T}_B$, and the theoretical brightness temperature, T_B,

$$\Delta T_B = \tilde{T}_B - T_B \tag{5.2}$$

is used to increment the liquid water content in the atmosphere until ΔT_B is within the SSM/I instrument noise level of 0.5 K. Newton's method (Conte and de Boor, 1980) is used to increment the cloud liquid water content of the model cloud so that,

$$CLW_{i+1} = CLW_i - \frac{\Delta T_{B_i}(CLW_i - CLW_{i-1})}{(\Delta T_{B_i} - \Delta T_{B_{i-1}})}, \tag{5.3}$$

where CLW is the cloud liquid water content and the subscripts denote the iteration number. To initialize the method, CLW_1 is assumed to be small (0.005 kg·m^{-2}). The method converges in 2-4 iterations.

The integrated cloud liquid water is calculated using the retrieved cloud water content and the cloud top and base pressures which are converted to height coordinates assuming hydrostatic equilibrium. The retrieved cloud water content is integrated over the model's cloud depth to provide integrated cloud water in units of kg·m^{-2} which is also equivalent to depth units of mm·cm^{-2} (another commonly used unit is g·cm^{-2} which is equivalent to 10 kg·m^{-2}).

5.1.5 Summary of the Cloud Liquid Water Retrieval Method

Below is a brief outline of the cloud liquid water retrieval method.

- Check if $\tilde{T}_B(85.5\ GHz) > 255$ K and ϵ_ν is available.
- Initialize retrieval process.
    1. Calculate theoretical brightness temperature T_B for clear sky conditions (CLW_0) given an initial sounding profile, surface temperature, and estimated ϵ_ν (from Chapter 4).
    2. Calculate ΔT_{B_1}.
    3. Determine cloud top and cloud base pressure levels.
    4. Initialize CLW a small amount (0.005 kg·m^{-2}) within cloud vertical limits.

- Iteration procedure.
    1. Compute new theoretical brightness temperature, T_{B_i}.
    2. Calculate ΔT_{B_i} (if ΔT_{B_i} < min. error then exit loop).
    3. Use Equation 5.3 to find new CLW_{i+1}.
    4. Go to iteration procedure step 1.
- Sum cloud liquid water content throughout depth of cloud to compute integrated cloud liquid water.

5.2 RESULTS

Integrated cloud liquid water was retrieved for areas which had 85.5 GHz coverage and surface emittance retrieval estimates avaliable for the composite time period in Chapter 4. The cases with considerable cloudiness (cases 6 and 7) were selected for retrieval of integrated cloud liquid water. Black colored areas in the images of integrated cloud liquid water in Figures 5.2, 5.3, 5.4, and 5.5 are areas where the criterions of brightness temperatures above 255 K and available surface emittance estimates were not met. Areas which had 85.5 GHz brightness temperatures below 255 K are colored red.

Qualitatively the patterns of high cloud water content match the corresponding visible and infrared images from the GOES satellite in Figures 5.6, 5.7, 5.8, and 5.9. The convective nature of the cloud system in case 6 shows up well in Figures 5.2 and 5.3 with a large area in the Nebraska panhandle having brightness temperatures below 255 K at 85.5 GHz (denoted by red). The Nebraska storm movement to the northeast is detected in the comparison of the retrieved cloud water imagery to the GOES infrared and visible data. The microwave data was observed 27 minutes after the GOES data (see Table 3.1). The magnitudes of the cloud liquid water amounts are generally under 1.0 kg$\cdot$m^{-2} for over 90% of the SSM/I data points. This is reasonable since the FOV of the instrument is relatively large in comparison to many clouds which may contain higher cloud liquid water amounts and are averaged throughout the entire FOV. The spatial distribution compared to the infrared and visible imagery seems reasonable, with larger integrated cloud liquid water amounts closer to the areas of likely precipitation (areas where $T_B < 255$ K).

Case 7 has more stratiform cloudiness associated with the post-frontal upslope conditions. The retrieved integrated cloud liquid water in Figures 5.4 and 5.5 shows higher

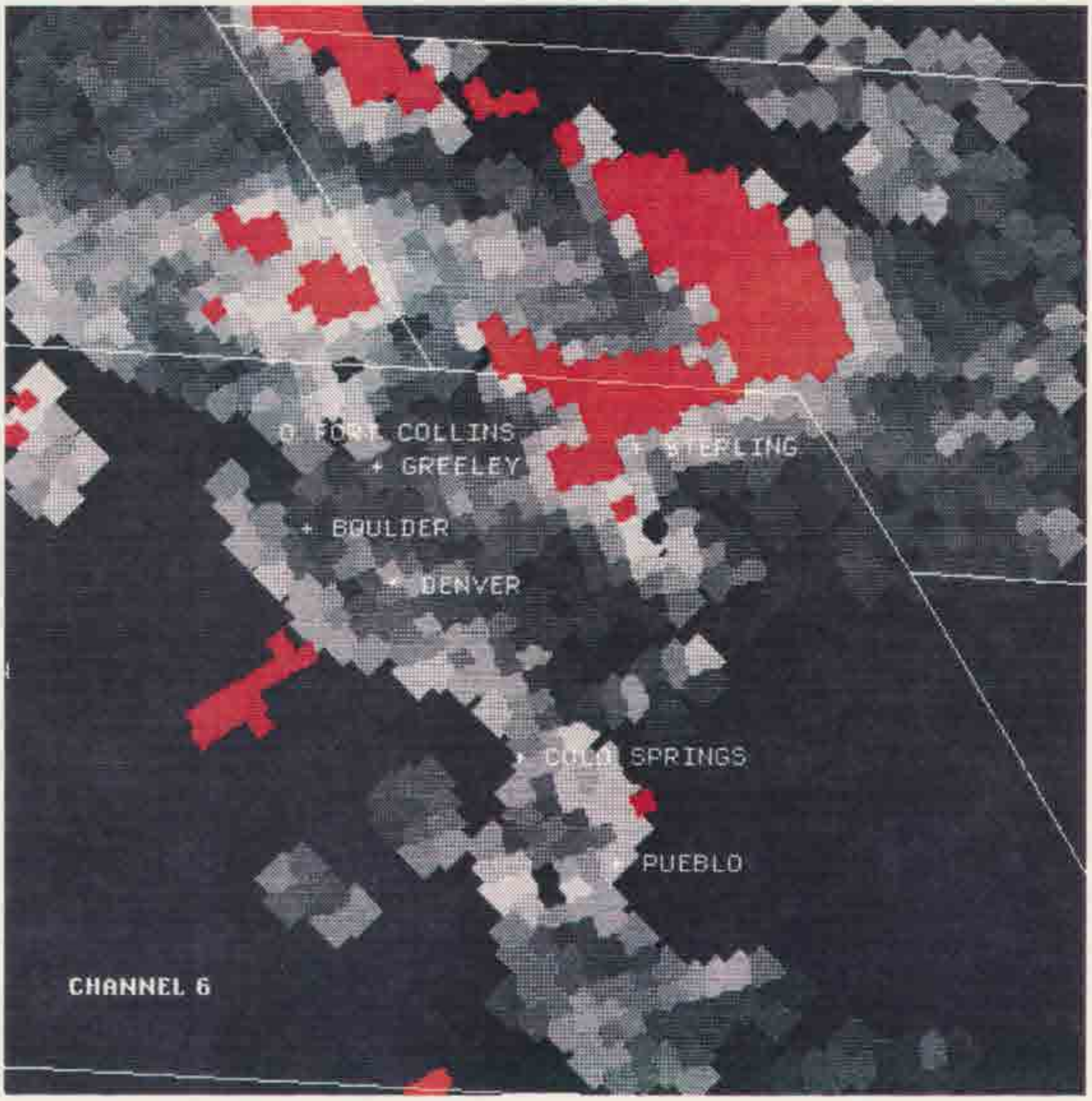

Figure 5.2: Integrated cloud liquid water imagery for case 6 from channel 6 data.

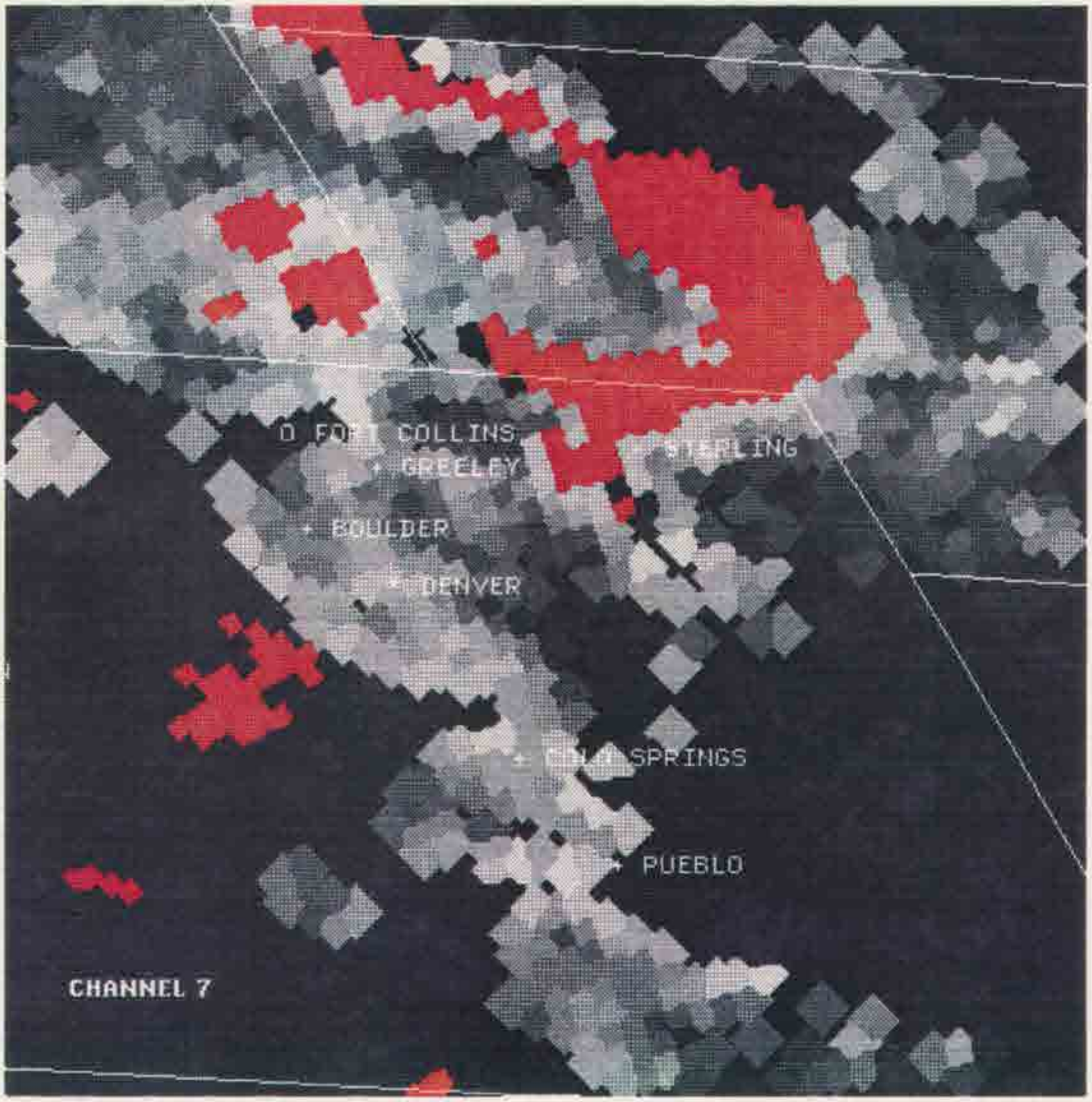

Figure 5.3: Integrated cloud liquid water imagery for case 6 from channel 7 data.

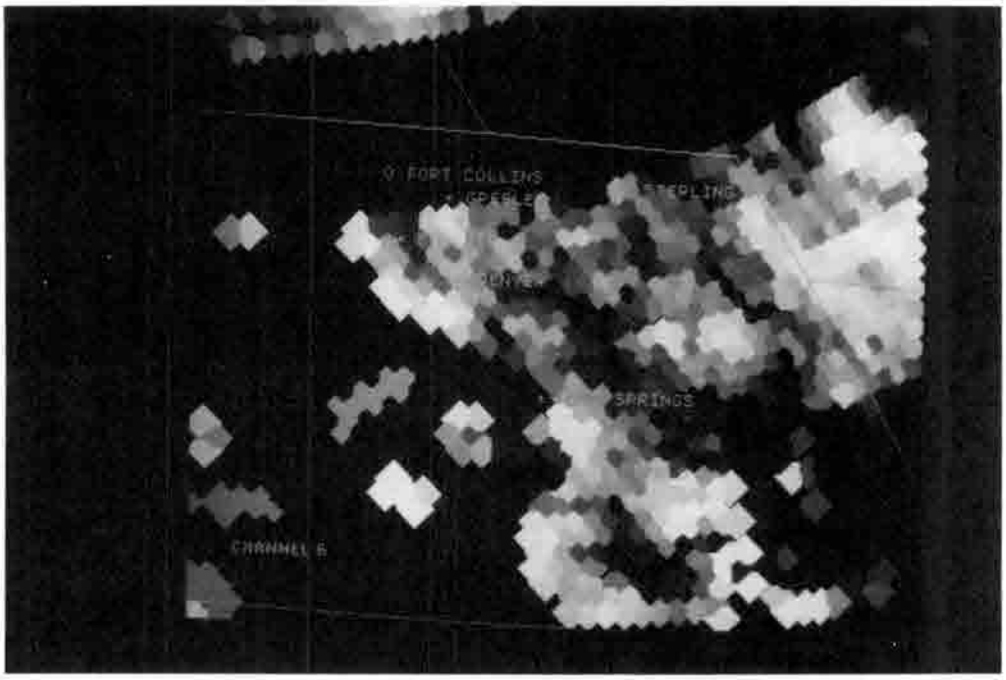

Figure 5.4: Integrated cloud liquid water for case 7 from channel 6 data.

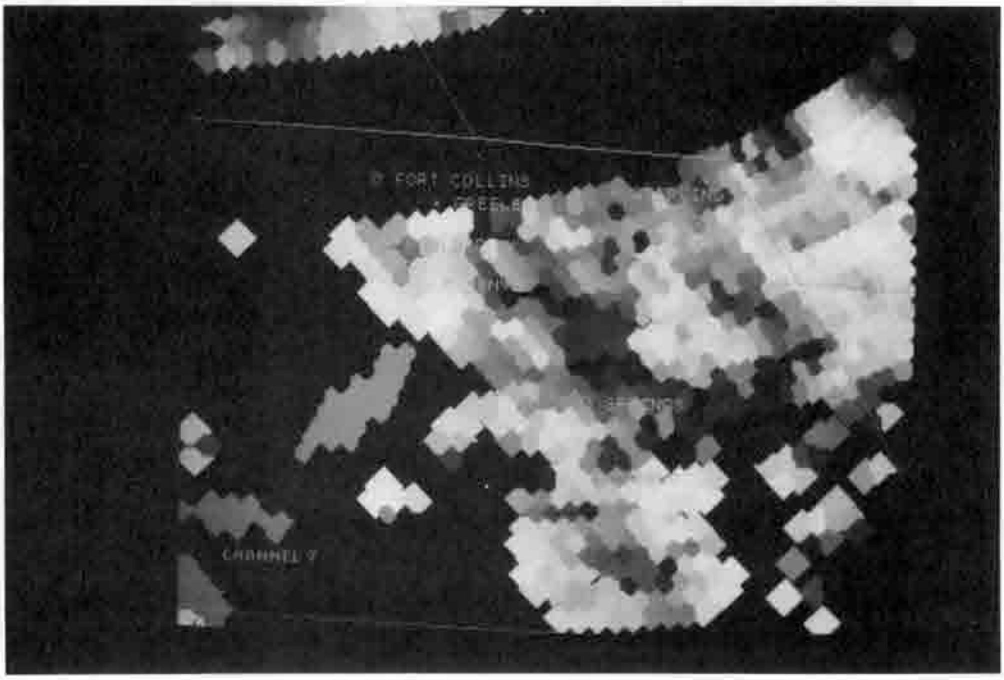

Figure 5.5: Integrated cloud liquid water for case 7 from channel 7 data.

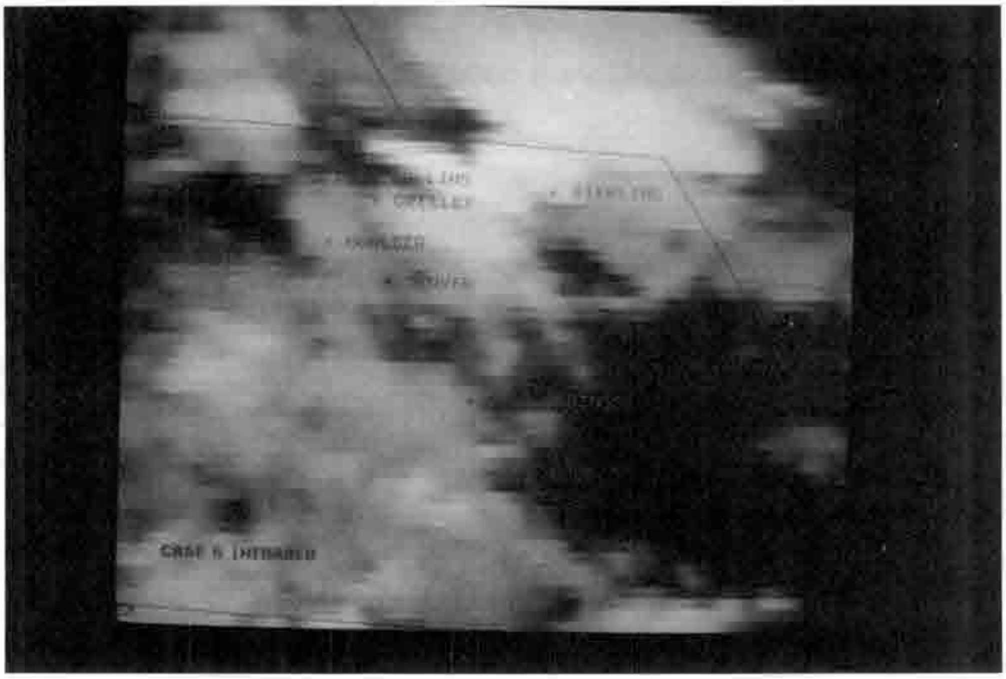

Figure 5.6: GOES VISSR infrared imagery (channel 8) for case 6.

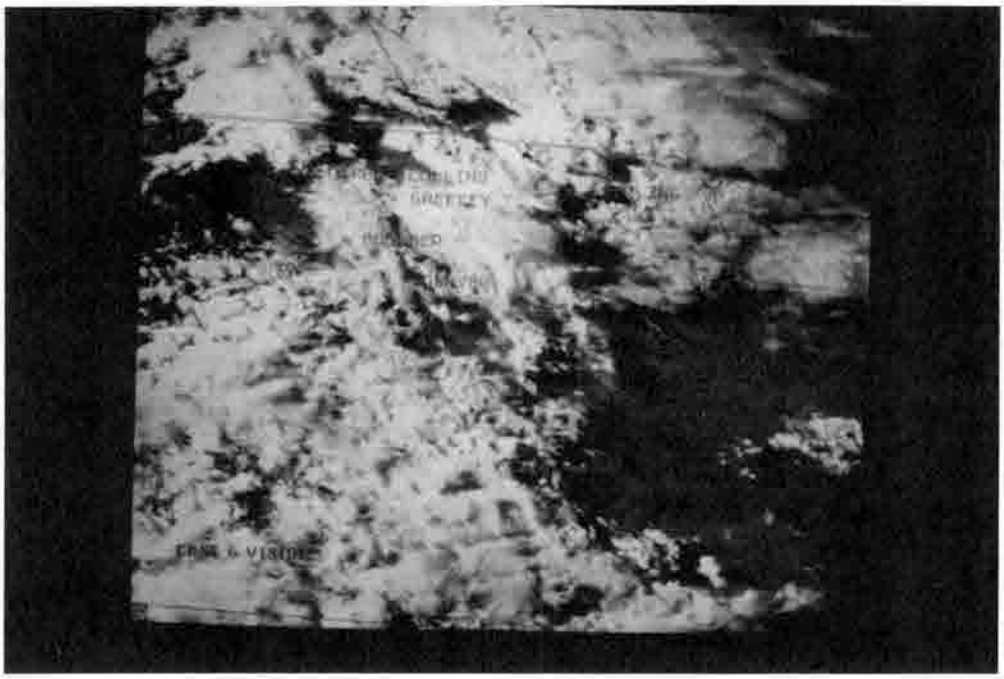

Figure 5.7: GOES VISSR visible imagery for case 6.

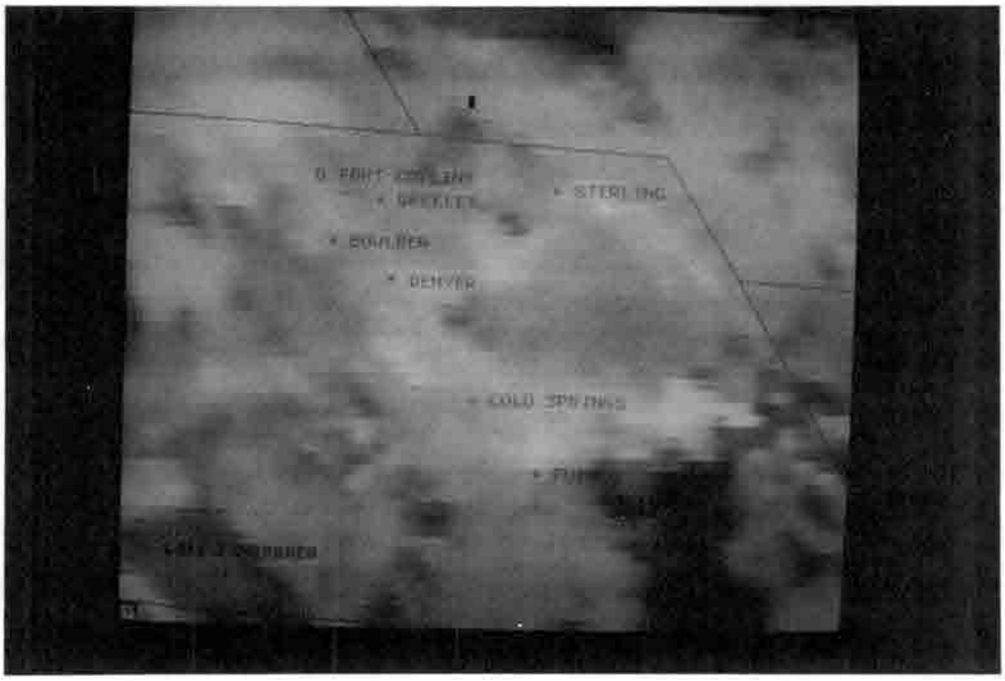

Figure 5.8: GOES VISSR infrared imagery (channel 8) for case 7.

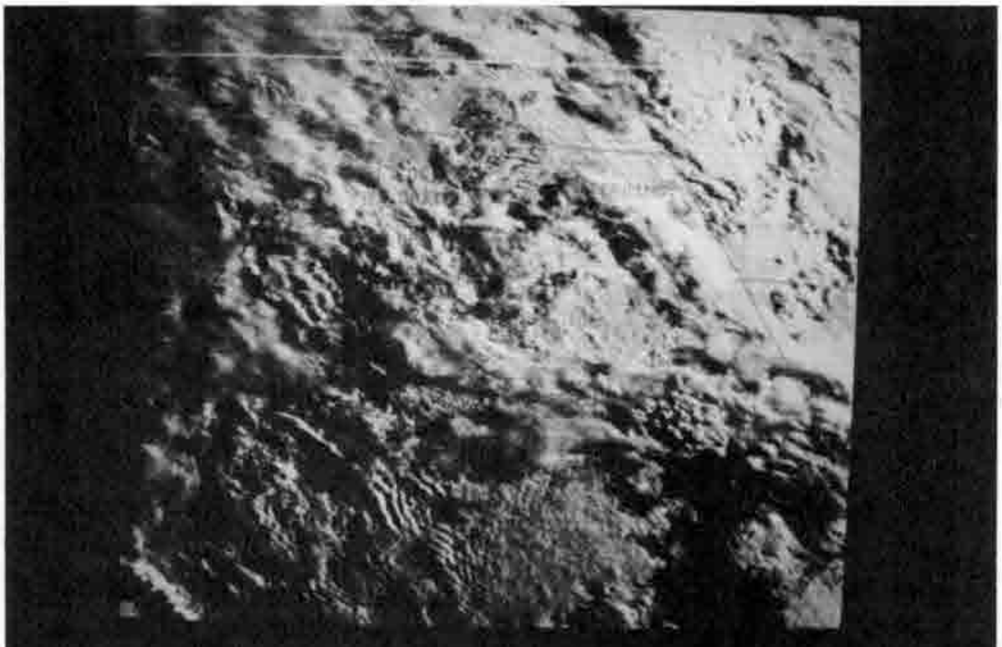

Figure 5.9: GOES VISSR visible imagery for case 7.

cloud water amounts over the eastern portion of the case study region in southwestern Nebraska which is also suggested from the more stratocumulus-like clouds observed in the visible imagery in Figure 5.9.

5.3 INTEGRATED CLOUD LIQUID WATER RETRIEVAL ERRORS

Unlike water vapor, temperature, and other commonly measured meteorological variables, cloud liquid water is not routinely measured. Cloud liquid water measurements over land are limited to instrumented aircraft and ground-based microwave radiometers. Aircraft studies are expensive and retrieve highly variable cloud liquid water contents which are not necessarily representative of the larger scale cloud liquid water seen by the satellite. Ground-based microwave radiometer measurements have the advantage of measuring integrated cloud liquid water amounts similar to the satellite, but lack the ability to determine the horizontal distribution of cloud liquid water. Thus, verification of cloud liquid water estimates is a difficult task. Numerical error analysis must suffice in the absence of quantitative measurements.

5.3.1 Numerical Error Analysis Results

Error sensitivity of the integrated cloud liquid water retrieval algorithm was calculated using numerical simulations which introduced random errors to the various input parameters. Several cloud heights and integrated cloud liquid water amounts were chosen to help determine a physical explanation of the retrieval error sensitivity. The error sensitivity calculations used the atmospheric water vapor and temperature profiles from case 7. The results of this analysis in Table 5.1 show smaller errors for clouds which have high cloud tops. The microwave brightness temperature is more sensitive to the cloud liquid water content at low cloud top pressures than at high cloud top pressures as shown by the wider separation of the curves in Figure 5.1. The curves become narrower as the cloud height decreases which reduces the ability of the satellite to detect integrated cloud liquid water accurately and produces the larger integrated cloud liquid water retrieval error sensitivity in Table 5.1. At lower cloud top pressures, the brightness temperature varies very little with changes in the cloud liquid water amount and any intial low value of cloud

Table 5.1

Table 5.1: Error sensitivity analysis for retrieved integrated cloud liquid water.

Integrated cloud liquid water ($kg{\cdot}m^{-2}$)	Cloud top pressure (hPa)					
	300		400		500	
	($kg{\cdot}m^{-2}$)	%	($kg{\cdot}m^{-2}$)	%	($kg{\cdot}m^{-2}$)	%
0.5	0.047	9.5	0.071	11.4	*	*
1.0	0.059	5.9	0.086	8.6	0.417	41.7
1.5	0.080	5.3	0.124	8.3	0.251	16.7
2.0	0.109	5.4	0.177	8.9	0.376	18.8
2.5	0.149	6.0	0.256	10.2	0.503	20.1

*large errors (results dependent on initial guess).

liquid water is within the instrument noise level and is therefore the retrieved integrated cloud liquid water amount. This makes the low level clouds with small amounts of cloud liquid water dependent on the initial guess of the algorithm.

The large percentage error for small integrated cloud liquid water amounts in Table 5.1 is due to the relatively large instrument noise affecting the small brightness temperature signal the low integrated cloud liquid water clouds have. The lowest percentage errors are found for medium amounts of integrated cloud liquid water. The percentage error increases again for large integrated cloud liquid water amounts as the radiometric signal becomes saturated due to the large amount of cloud liquid water which forces the brightness temperature to approach the ambient temperature of the cloud as the cloud becomes more opaque.

5.3.2 Comparison of Retrievals from Channels 6 and 7

Support of the numerical error analysis results is found when the retrieved integrated cloud liquid water from both 85.5 GHz channels (channel 6 and channel 7) at the same location are compared. A scatter plot of retrieved integrated cloud liquid water for case 6 for channels 6 and 7 in Figure 5.10 shows a distinct bias between the channels. A best least-squares line was fitted to the data and the slope of the line indicates a bias of approximately 0.6 with channel 7 retrieving higher integrated liquid water amounts. The linear correlation coefficient of the line for case 6 is 0.874. Similar results were found for

Table 5.2

Table 5.2: Comparison statistics of integrated cloud liquid water retrievals from channels 6 and 7.

Cloud top pressure range (hPa)	Slope	Intercept	Linear correlation coefficient	Standard deviation (channel 6)	Standard deviation (channel 7)
CASE 6					
0-900	0.586	0.054	0.874	0.142	0.243
0-500	0.688	0.026	0.936	0.104	0.151
500-900	0.369	0.111	0.734	0.175	0.473
CASE 7					
0-900	0.622	0.057	0.885	0.116	0.186
0-500	0.665	0.044	0.921	0.094	0.143
500-900	0.262	0.215	0.451	0.275	1.051

case 7 and are listed in Appendix C (see Table 5.2 for summaries of results from cases 6 and 7). If the retrieved integrated cloud liquid water for case 6 is separated into clouds with high cloud tops ($p_{\text{top}} < 500$ hPa) and low cloud tops (500 hPa $< p_{\text{top}} < p_{\text{bot}}$), it is noticed that the largest variability is in the lower level clouds (see Figures 5.11 and 5.12). This supports the numerical error analysis results.

Since channel 6 retrieved lower integrated cloud liquid water amounts than channel 7, this suggests that there may be a brightness temperature bias between the 85.5 GHz channels. The much larger variability of the channel 7 retrieved values in comparison to channel 6 is additional evidence of a brightness temperature bias. If the brightness temperatures were too cold in a channel, the retrieved integrated cloud liquid water amounts would be larger than retrievals using the unbiased brightness temperatures. The numerical error sensitivity results also show that the lower clouds would be much more influenced by a bias in the brightness temperatures which matches the observed comparison statistics in Table 5.2. Other physical factors which can cause differences in the observed brightness temperature polarization could also be occurring, but due to the broad nature of the integrated cloud liquid water retrieval bias for high and low cloud heights, a consistent instrument bias is more probable.

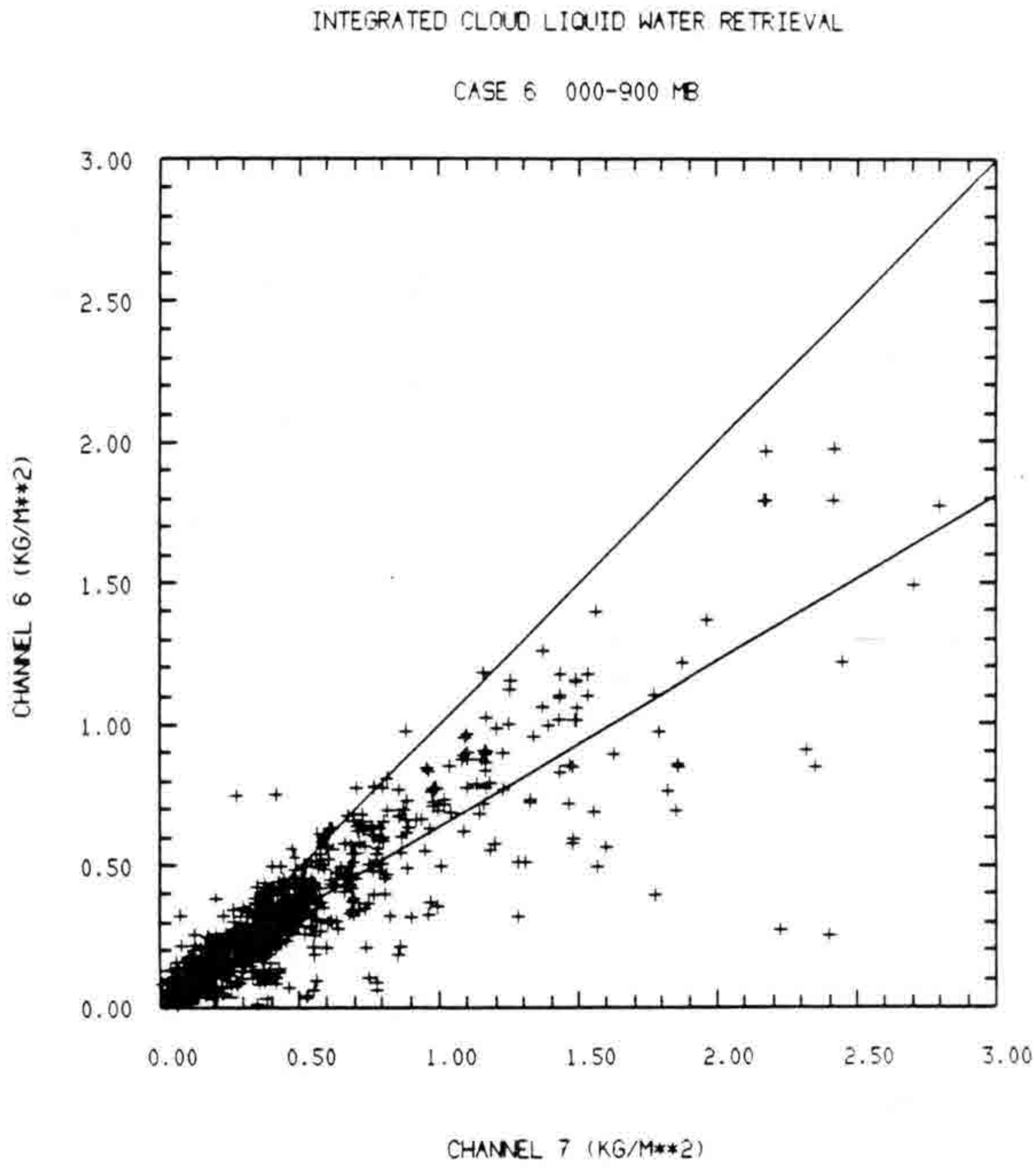

Figure 5.10: comparison of integrated cloud liquid water retrievals from channels 6 and 7 for case 6 ($p_{\text{top}} < p_{\text{bot}}$).

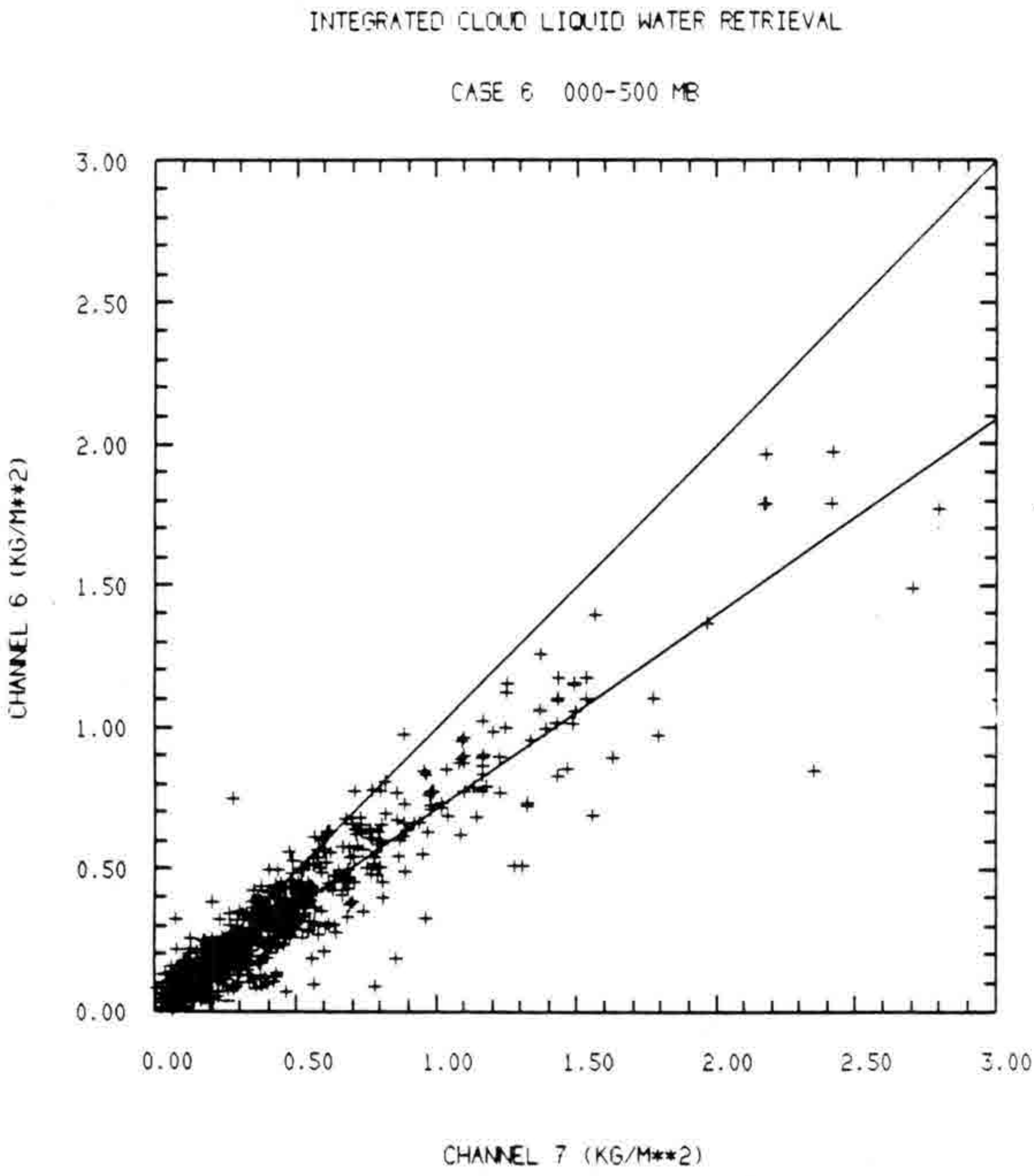

Figure 5.11: comparison of integrated cloud liquid water retrievals from channels 6 and 7 for case 6 ($p_{\rm top} < 500$ hPa).

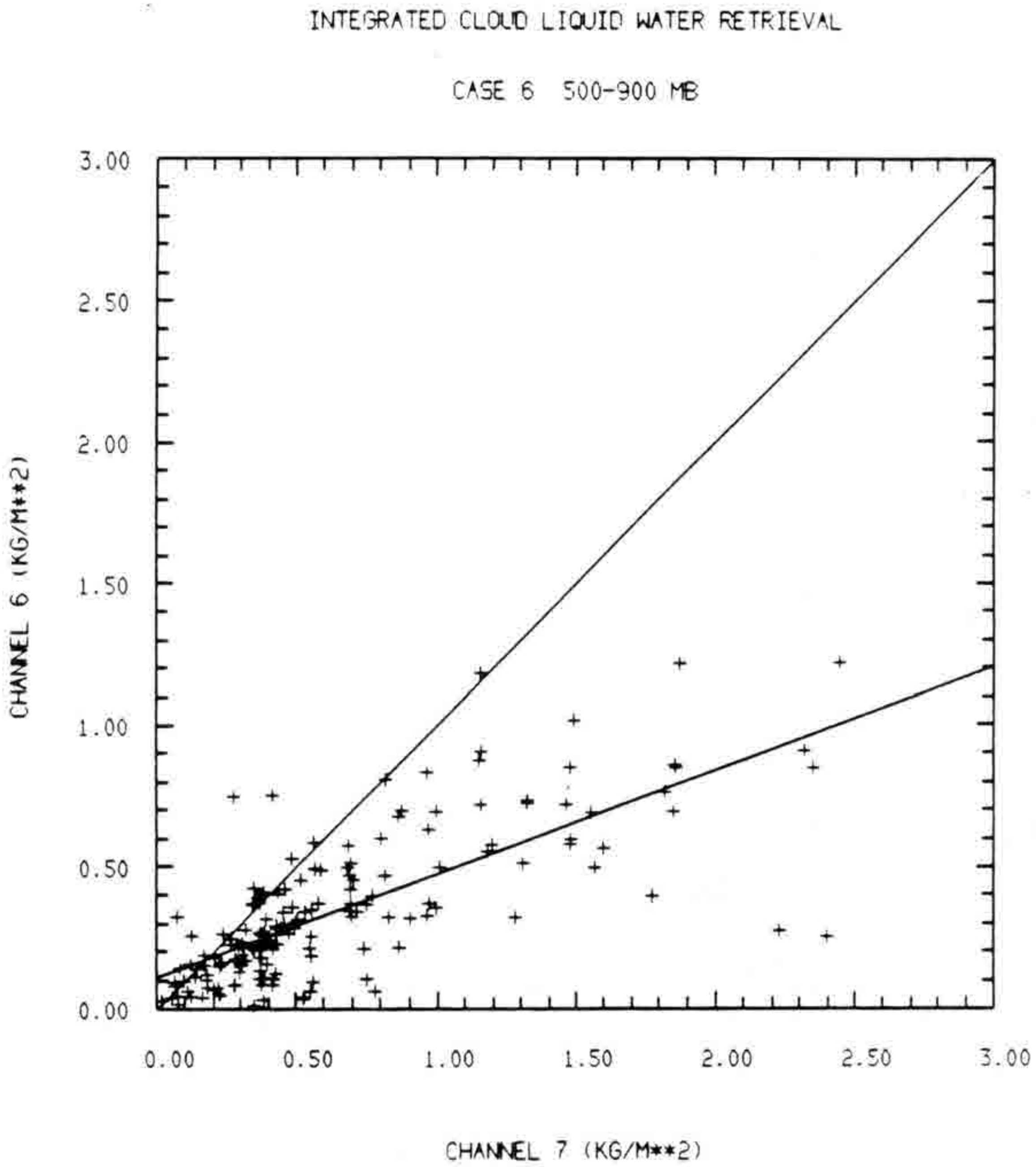

Figure 5.12: comparison of integrated cloud liquid water retrievals from channels 6 and 7 for case 6 (500 hPa $< p_{\text{top}} < p_{\text{bot}}$).

Table 5.3

Table 5.3: Comparison statistics of integrated cloud liquid water retrievals from channels 6 and 7 with bias correction.

Cloud top pressure range (hPa)	Slope	Intercept	Linear correlation coefficient	Standard deviation (channel 6)	Standard deviation (channel 7)
CASE 6					
0-900	0.850	0.068	0.9188	0.141	0.166
0-500	0.868	0.052	0.9429	0.117	0.135
500-900	0.665	0.192	0.8089	0.211	0.317
CASE 7					
0-900	0.901	0.076	0.9135	0.136	0.150
0-500	0.891	0.077	0.9321	0.110	0.124
500-900	0.773	0.261	0.7884	0.399	0.516

To estimate the possible maximum influence on the retrieved integrated cloud liquid water amounts, the brightness temperatures were biased the maximum absolute error of the instrument (1.5 K) and the surface emittances were offset 0.01 to take into account the effect the brightness temperature shift would have on the surface emittance retrievals. (The surface emittance change of 0.01 is an approximation from the error analysis results of the surface emittance retrieval algorithm. A more rigorous procedure would be to recalculate the surface emittances for each clear sky case assuming a brightness temperature bias of 1.5 K.) The new retrieved integrated cloud liquid water comparison for case 6 in Figure 5.13 shows only a slight bias in the same direction (similar results are obtained for case 7 which are shown in Appendix C). The correlation coefficients listed in Table 5.3 are also improved even though the surface emittances were not explicitly recalculated for each data point. As a function of cloud top pressure, the most improvement is seen in the low level clouds which have the highest variability due to brightness temperature noise (see Figures 5.14 and 5.15).

The intercept of the best-fitting line is slightly higher when the bias correction is applied. The original calculations of surface emittance calibrated the channels to a reference infrared derived surface skin temperature. When the clouds begin to obscure the surface and the transmittance of the atmosphere decreases, this calibration effect diminishes. The

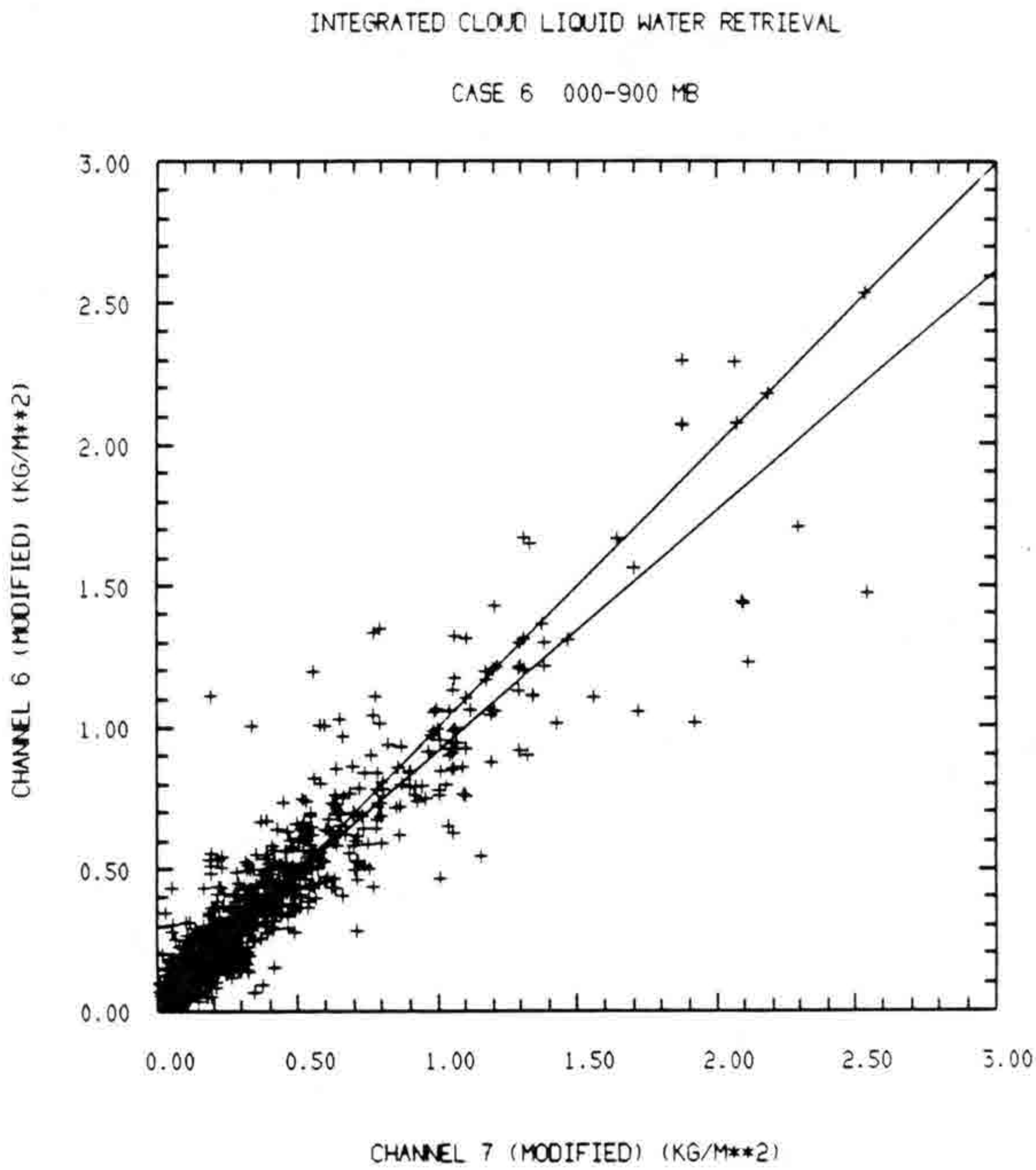

Figure 5.13: Comparison of integrated cloud liquid water retrievals using channels 6 and 7 with bias correction for case 6 ($p_{\text{top}} < p_{\text{bot}}$).

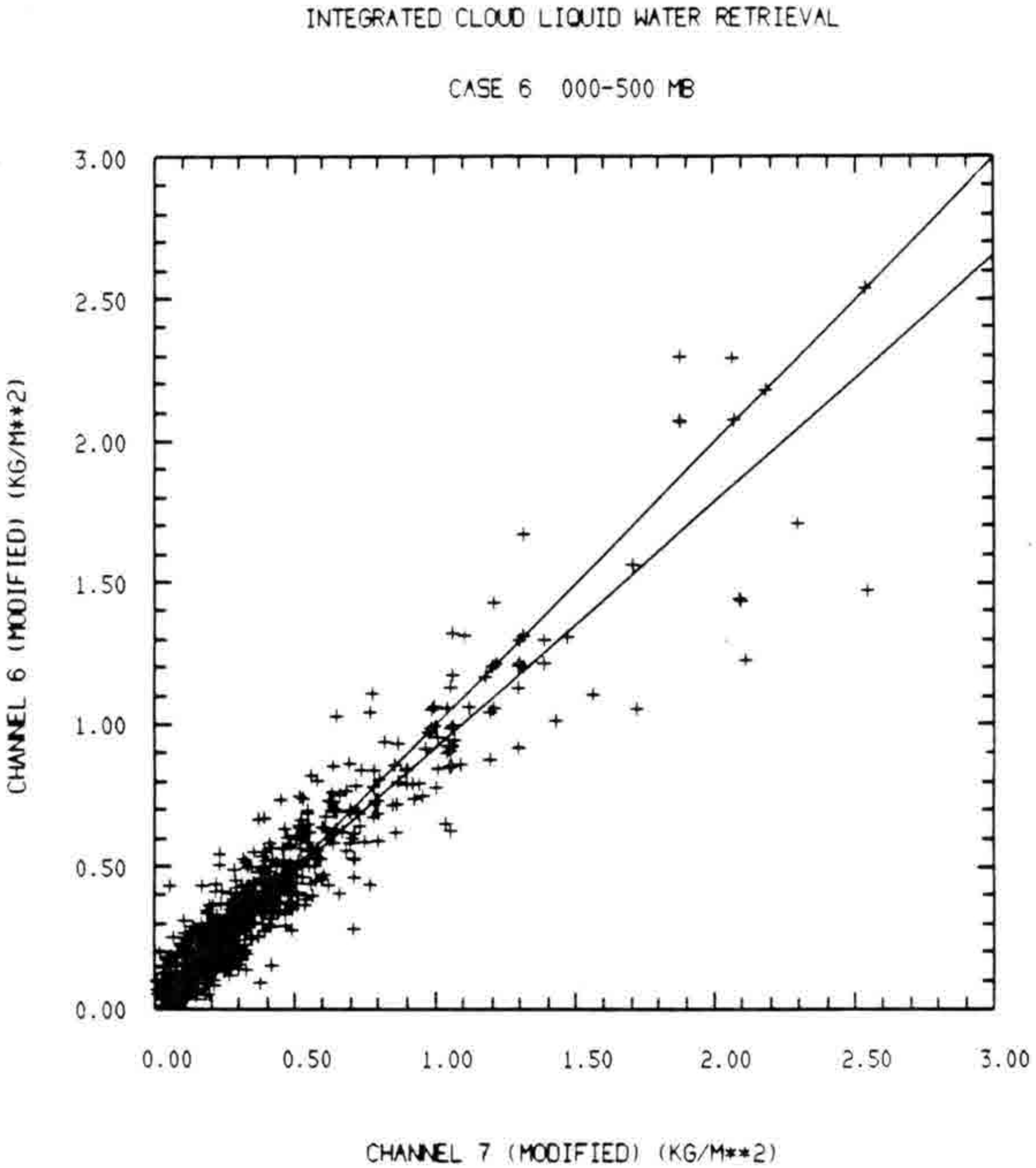

Figure 5.14: Comparison of integrated cloud liquid water retrievals using channels 6 and 7 with bias correction for case 6 ($p_{\text{top}} < 500$ hPa).

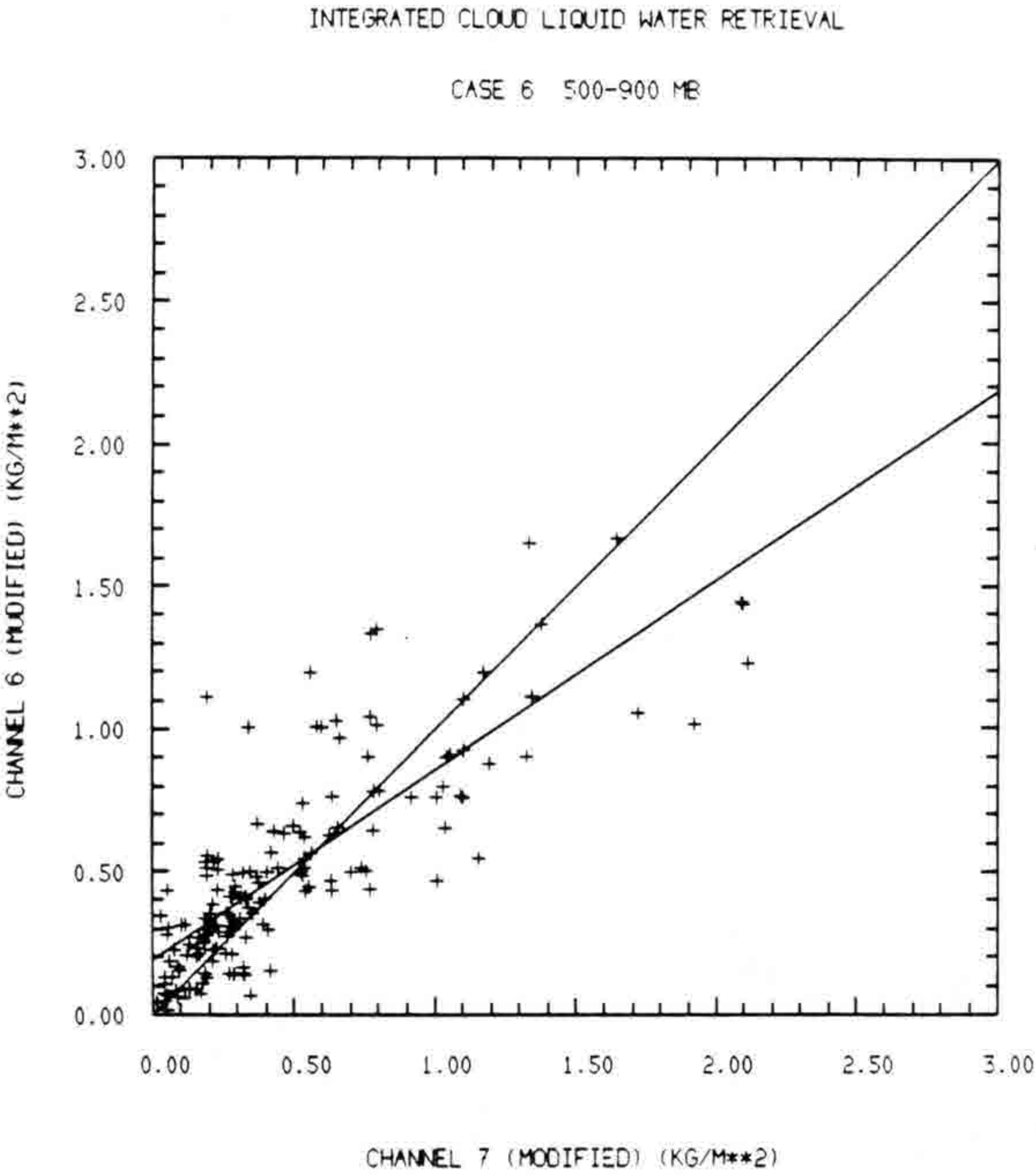

Figure 5.15: Comparison of integrated cloud liquid water retrievals using channels 6 and 7 with bias correction for case 6 (500 hPa $< p_{\text{top}} < p_{\text{bot}}$).

bias correction offset the surface calibration effect since the assumed surface emittance change of 0.01 is an approximation and small errors are likely to be introduced for the low integrated cloud liquid water conditions. The standard deviations of the retrieved integrated cloud liquid water from the best-fitting line are comparable to the estimated errors from the numerical error analysis. Both cases have standard deviations of approximately 0.15 $kg \cdot m^{-2}$ with the more stratiform case (case 7) having slightly less variability. The retrieval variability dependence on the cloud top pressure due to instrument noise is still present in the bias corrected data with values close to the numerically estimated noise levels. Comparison of the standard deviations from channels 6 and 7 also show a much closer relationship between the channels.

5.3.3 Other Sources of Retrieval Error

Not all of the bias between the 85.5 GHz vertical and horizontal polarization channels (channels 6 and 7) can be explained by instrument bias alone. The retrieved integrated cloud liquid water with the maximum bias correction applied still has a bias of 0.85 for the convective case (case 6) and 0.90 for the stratiform case (case 7). From the scatter plots it appears that the bias for the stratiform case is an artifact of the surface emittance change associated with the imposed brightness temperature correction since the large number of points in the 0.5 $kg \cdot m^{-2}$ region appear to be slightly shifted which would influence the slope of the best-fit line. The convective case (case 6) seems to be more influenced by the displacement of the larger integrated cloud liquid water amounts in the direction of the bias. Partially filled FOVs with precipitating clouds would have this effect. The results of Kummerow and Wienman (1988) using a finite cloud model which determines the microwave brightness temperatures for precipitating clouds indicate that polarization of the channels is possible due to aspherical hydrometeors. Little change is found in the microwave brightness temperatures for a very small FOV fraction filled with a precipitating cloud, but if larger amounts of the FOV are contaminated by precipitating clouds the brightness temperature can be polarized enough to influence the retrieval of cloud liquid water (see Table 5.4). (The lower brightness temperatures in Table 5.4 should be viewed with caution since they were calculated at a frequency of 37 GHz and are higher than the

Table 5.4

Table 5.4: Horizontal/Vertical polarized brightness temperatures at a zenith angle of 50° from precipitating clouds over land at 37 GHz (adapted from Kummerow and Wienman, 1988).

Rain rate	Fractional FOV coverage				
$\mathrm{mm \cdot h^{-1}}$	1/16	1/8	1/4	1/2	1
2	281.3/281.5	279.5/279.9	277.3/277.8	274.8/275.5	272.7/273.4
4	277.8/278.4	274.9/275.6	271.2/272.0	267.1/268.2	263.9/265.1
8	272.8/273.6	268.6/269.6	262.8/264.2	256.7/258.4	*
16	266.4/267.4	260.2/261.8	*	*	*
32	257.5/259.4	*	*	*	*

*Brightness temperatures below 255 K.

equivalent brightness temperatures would be at 85.5 GHz (Wu and Wienman, 1984). The instrument noise obscures what could be sub-FOV precipitating clouds in the integrated cloud liquid water retrievals, thus conclusions on the effect of small precipitating clouds within the microwave FOV are incomplete.

The vertical distribution of the cloud liquid water can play an important role in the accuracy of the retrieval method. It has been shown that the microwave brightness temperatures are more sensitive to the higher level cloud liquid water due to their colder temperature. Another concern is the level at which the cloud becomes mostly ice. For higher clouds the method over estimates the integrated cloud liquid water since ice is present in the upper portions of the cloud which is modeled as liquid water which has a stronger attenuation. A retrieval of both ice and liquid water in the cloud is necessary to resolve this problem.

5.3.4 Summary of Cloud Liquid Water Retrieval Results

The method presented shows some degree of skill in measuring integrated cloud liquid water amounts over land surfaces. Qualitatively, the spatial distribution of retrieved integrated cloud liquid water seems in good agreement with other available data sources. Since no conventional absolute measurements of cloud liquid water content were taken it is difficult to estimate the absolute accuracy of the retrieval algorithm, but numerical error analysis and comparisons of channels 6 and 7 show an approximate retrieval accuracy of 0.15 kg$\cdot$m^{-2}. This compares favorably to the previous methods of Liou and Duff (1979) and Yeh and Liou (1983) discussed in Chapter 1. The error estimate of 0.15 kg$\cdot$m^{-2} includes instrument brightness temperature noise but excludes brightness temperature biases which affect the absolute accuracy of the method. Effects of instrumental brightness temperature noise was shown to impact the statistical method of Yeh and Liou in a detrimental way by imposing large biases on the results.

The sensitivity to instrument noise was shown to increase with lower cloud top pressure. This is a physical limitation of the microwave brightness temperature behavior over land surfaces. A lower region in the atmosphere exists which is lower in temperature than the physical temperature of the surface but is the *same* brightness temperature due to the non-unity surface emittance. The error analysis suggests that the retrieval algorithm would be more accurate in areas where a large surface-cloud temperature contrast exists. The regions of higher surface emittance are also preferred areas since a higher surface emittance increases the microwave radiation emitted by the surface which makes the surface-cloud brightness temperature contrast larger just as a higher surface skin temperature would.

A brightness temperature bias in the 85.5 GHz channels was shown to be a probable cause of the bias in the retrieved integrated cloud liquid water amounts. Indications of sub-FOV precipitation within the microwave FOV are suggested from the comparison of the polarization data from a convective case and a more stratiform case. Instrument noise levels were too high to determine quantitative sub-FOV precipitation effects. The vertical distribution of the liquid water in the cloud needs to be determined more accurately especially with regards to the higher cloud levels where the brightness temperature sensitivity is highest.

Chapter 6

SUMMARY AND CONCLUSIONS

6.1 SURFACE EMITTANCE RETRIEVAL

6.1.1 Summary and Conclusions

Using co-located infrared and microwave data it has been shown that surface emittance values can be estimated at 85.5 GHz with a relative error of ± 0.005 and an absolute error of ± 0.012 when the atmospheric effects (which are significant at higher frequencies) have been theoretically accounted for using a radiative transfer model. The emittance in the lower frequency channels, which have less atmospheric attenuation, can be retrieved more accurately. The microwave surface emittances vary considerably over small spatial distances. Wetting of the surface by precipitation and irrigation, which exhibits a large influence over the depression of surface emittance values, are strongly suspected of being responsible for this spatial variation.

6.1.2 Applications and Further Work

Further work is needed to determine microwave surface effects and their effect on remote sensing at millimeter wavelengths over various surface types such as snow cover, mountainous terrain, heavy vegetation, etc. The variability of these effects and their relationship to the various geophysical parameters are important to the use of present and future microwave radiometers which have many current and potential surface sensing applications. Quantification of the relation of surface soil moisture and vegetation to surface emittance for applications to hydrologic and mesoscale modeling is an area of current need. Retrieval of surface soil moisture seems to be possible if the atmospheric variables which also influence the microwave brightness temperature are properly handled. Retrieval of surface soil moisture has implications for hydrologic and atmospheric mesoscale modeling efforts which need reliable high density surface data to estimate surface soil moisture conditions and surface energy fluxes which impact the hydrologic cycle and mesoscale atmospheric circulations.

High surface emittances in the 22.235 GHz channel over some areas of Nebraska suggest that improvements to the horizontal homogeneity assumption are necessary. This could be done by using multiple soundings (radiosonde or satellite-derived) to generate more accurate water vapor and temperature fields to be used in the transmittance calculations. A data set from a longer time period would be better suited to a soil moisture study. Variations due to gradual drying of the surface or surface emittance depressions caused by precipitation would be more noticeable if a surface emittance climatology could be developed. Diurnal surface emittance variability due to wetting by morning dew and fog, especially along the east coast, could further improve our understanding of the physical mechanisms which cause surface emittance variability. A combination of infrared methods which use diurnal surface skin temperature changes (Wetzel *et al.*, 1984; Wetzel and Woodward, 1987) and microwave methods would create an optimal soil moisture sensing method.

6.2 CLOUD LIQUID WATER RETRIEVAL

6.2.1 Summary and Conclusions

An integrated cloud liquid water retrieval method over land surfaces has been developed and used to derive cloud liquid water over semi-arid conditions centered over northeast Colorado during the first week of August 1987. The 85.5 GHz channels on the SSM/I instrument used in the study have higher sensitivity to cloud liquid water in the atmosphere which allows for the ability to determine cloud liquid water over land surfaces. The magnitudes and distribution of the retrieved integrated cloud liquid water fields appear consistent with other available data sources.

Integrated cloud liquid water can be retrieved within 0.15 kg$\cdot$m^{-2} with this method including instrument noise. The method is quite sensitive to biases in the brightness temperatures and needs an absolute calibration method to verify the actual retrieval values.

The error sensitivity was found to highest in low level clouds where the brightness temperature of the surface is approximately the same as the ambient cloud temperature thus any additional cloud liquid water at that level has no influence on the satellite observed brightness temperature. A bias in the retrieved integrated cloud liquid water from the horizontal and vertical polarizations was observed. A brightness temperature correction of 1.5 K improves the results, with the new retrieval results having a statistical variability which agrees with the numerically derived error estimates. Thus, some instrument bias is probable between the 85.5 GHz channels. Small sub-FOV precipitating clouds were also noted as a possible contributor to the channel bias for isolated cases, but due to the broad nature of the original biased results it is more likely that this effect was not the major source of the apparent bias. The comparison of the convective and more stratiform cloud cases show higher variability for the convective case, which is consistent with the effects that the sub-FOV nonhomogeneities would have in the convective case.

The integrated cloud liquid water retrieval method performs best for conditions in which supercooled cloud liquid water exists. The optimum cloud temperature range is approximately $-20°C < T_c < 5°C$ (for $\epsilon_\nu \approx 0.95$) with extension to warmer clouds possible if the microwave surface emittance is higher. There are still some unexplained retrieval output which requires further work and verification.

6.2.2 Applications and Further Work

The study of liquid water and its variability have been largely limited to areas over ocean surfaces. Methods such as the one developed in this study offers new opportunities for climatological studies over land as well. This would complete the overall view of global liquid water distribution. Areas of liquid water development and decay in relation to the continental land mass distribution would provide an element missing from current studies. In addition, detection of clouds likely to contain supercooled cloud liquid water has implications for the aviation industry with regards to aircraft icing. Forecasts of icing conditions could be updated periodically using results from the satellite cloud liquid water retrievals. Supercooled liquid water is also important in cloud precipitation processes and offers the possibility of separating clouds which are apparently similar in the visible and infrared imagery into life stages.

Developing cloud systems require much higher temporal sampling than presently available with polar-orbiting spacecraft. Sampling periods of less than one hour are necessary for study of cloud liquid water content in the life cycle of cloud systems. Coverage of surface emittance retrievals would also improve with multiple time period samples increasing the probability that clear skies are available for analysis. Geostationary platforms for microwave radiometers such as GOES-NEXT (Vonder Haar *et al.*, 1986) will be key to continuing progress in developing understanding of mesoscale processes which have time scales too small to be adequately studied using polar satellite data.

Improvements to the method's accuracy could be made by combining ground-based microwave radiometer systems into the retrieval process as a ground truth measurement which would calibrate the satellite-derived data thereby minimizing biases in the retrievals. Inclusion of data from the other SSM/I channels and infrared data such as the VAS sounding data in a multichannel retrieval algorithm similar to the method used by Olson (1986) to determine rainfall rates might also help alleviate problems such as the higher retrieval errors at low cloud height, effects of unknown cloud liquid water vertical distribution, and the precipitating sub-FOV clouds encountered in this study.

This study is one step in understanding the atmospheric-hydrologic cycle for mesoscale volumes over land. Precipitation was neglected in the present study, but work by Spencer *et al.* (1988), Simpson *et al.* (1988), and others show promise of high frequency microwave radiometers detecting if not quantifying rainfall from space-based sensors. The Tropical Rainfall Measuring Mission (TRMM) with a desired launch by 1994, will open new doors for remote sensing of water in the atmosphere with a satellite dedicated to the requirements of sensing rainfall from space (Theon, 1988). Extension of the surface emittance and cloud liquid water retrieval methods developed in this study will be possible with instruments onboard TRMM. Future studies utilizing radar, ground-based microwave radiometers, multi-channel infrared sensors and microwave instruments such as the SSM/I and instruments onboard TRMM should enable further improvements of remote sensing of water in the atmosphere.

REFERENCES

Allen, K. C., and H. J. Liebe, 1983: Tropospheric absorption and dispersion of millimeter and submillimeter waves. *IEEE Trans. Antennas Propag.*, **AP-31**, 221–223.

Becker, F., and B. J. Choudhury, 1988: Relative sensitivity of Normalized Difference Vegetation Index (NDVI) and Microwave Polarization Difference Index (MPDI) for vegetation and desertification monitoring. *Remote Sensing of Environ.*, **24**, 297–311.

Beers, Y., 1957: *Introduction to the Theory of Error.* Addison-Wesley Publishing Co., Reading, Mass., 66 pp.

Benoit, A. 1968: Signal attenuation due to neutral oxygen and water vapor, rain, and clouds. *Microwave J.*, **11**, 73–80.

Blanchard, B. J., M. J. McFarland, T. J. Schmugge, and E. Rhoades, 1981: Estimation of soil moisture with API algorithms. *Water Res. Bull.*, **17**, 767–774.

Carrier, L. W., G. A. Cato, and K. J. von Essen, 1967: The backscattering and extinction of visible and infrared radiation by selected major cloud models. *Applied Optics*, **6**, 1207–1216.

Center-pivot Irrigation Systems in Nebraska, 1985: Conservation and Survey Division Institute of Agriculture and Natural Resources, The University of Nebraska-Lincoln.

Chandrasekhar, S., 1960: *Radiative Transfer.* Dover Publications Inc., New York, 393 pp.

Chang, A. T., and T. T. Wilheit, 1979: Remote sensing of atmospheric water vapor, liquid water, and wind speed at the ocean surface by passive microwave techniques from the Nimbus 5 satellite. *Radio Sci.*, **14**, 793–802.

Chesters, D., and W. D. Robinson, 1983: Performance appraisal of VAS radiometry for GOES-4,-5,and -6. *NASA Tech. Memo.*, 85125 (NTIS Ref: N84-18781), 55 pp.

Choudhury, B. J., T. J. Schmugge, R. W., Newton, and A. Chang, 1979: Effect of surface roughness on the microwave emission from soils. *J. Geophys. Res.*, **84**, 5699–5706.

Clark, J. D., 1983: *GOES User's Guide*, U.S. Department of Commerce, NOAA-NESDIS.

Comiso, J. C., 1985: Remote sensing of sea ice using multispectral microwave satellite data. *Advances in Remote Sensing Retrieval Methods*, A. Deepak, Ed., Academic Press, 349–369.

Conte, S. D., and C. de Boor, 1980: *Elementary Numerical Analysis.* McGraw-Hill, Inc., New York, 432 pp.

Deirmendjian, D., 1963: Complete microwave scattering and extinction properties of polydispersed cloud and rain elements. Rand Corp. Rep. 12-422-PR, Santa Monica, California, 54 pp.

Deirmendjian, D., 1969: *Electromagnetic Scattering on Spherical Polydispersions.* American Elsevier Publishing Co., Inc., New York.

Elgered, G., B. O. Rönnäng, and J. I. H. Askne, 1982: Measurements of atmospheric water vapor with microwave radiometry, *Radio Sci.*, **17**, 1258–1264.

Feddes, R. G., and K. Liou, 1978: Atmospheric ice and water content derived from parameterization of Nimbus 6 High-resolution Infrared Sounder data. *J. Applied Meteor.*, **17**, 536–551.

Fleming, H. E., and L. M. McMillin, 1977: Atmospheric transmittance of an absorbing gas. 2: A computationally fast and accurate transmittance model for slant paths at different zenith angles. *Applied Optics*, **16**, 1366–1370.

Fletcher, N., 1963: *The Physics of Rainclouds.* Cambridge University Press, Cambridge, 390 pp.

Fraser, K. S., N. E. Gaut, E. C. Reifenstein, II, and H. Sievering, 1975: Interaction mechanisms — within the atmosphere. *Manual of Remote Sensing, I*, R. G. Reeves, ed., American Society of Photogrammetry, Falls Church, Virginia, Chapter 5, 207–210.

Gaikovich, K. P., N. N. Markina, A. P. Naumov, V. M. Plechkov, and M. I. Sumin, 1983: Investigation of remote sensing possibilities of the lower atmosphere in the microwave range and some aspects of statistical data use. *Int. J. Remote Sensing*, **4**, 419–431.

Gorelik, A. G., V. V. Kalashnikov, L. S. Raykova, and Yu. A. Frolov, 1973: Radiothermal measurements of atmospheric humidity and the integral water content of clouds. *Atmos. Oceanic Phys.*, **9**, 527–530.

Grody, N. C., 1976: Remote sensing of atmospheric water content from satellites using microwave radiometry. *IEEE Trans. on Antennas and Propag.*, **AP-24**, 155–162.

Grody, N. C., A. Gruber, and W. C. Shen, 1980: Atmospheric water content over the tropical pacific derived from the Nimbus-6 Scanning Microwave Spectrometer. *J. Applied Meteor.*, **19**, 986–996.

Grody, N. C., 1983: Severe storm observations using the Microwave Sounding Unit. *J. Climate and Applied Meteor.*, **22**, 609–625.

Guiraud, F. O., J. Howard, and D. C. Hogg, 1979: A dual-channel microwave radiometer for measurement of precipitable water vapor and liquid. *IEEE Trans. Geosci. Electron.*, **GE-17**, 129–136.

Gunn, K. L. S., and T. W. R. East, 1954: The microwave properties of precipitation particles. *Quart. J. Royal Meteor. Soc.*, **80**, 522–545.

Gurvich, A. S., and V. V. Demin, 1970: Determination of the total moisture content in the atmosphere from measurements on the Cosmos 243 satellite. *Atmos. Oceanic Phys.*, **6**, 453–457.

Heggli, M. F., 1985: The role of microwave radiometry in weather modification research. *Fourth WMO Scientific Conf. on Wea. Mod.*, Honolulu, Hawaii, WMO, 157–162.

Heggli, M. F., and D. Reynolds, 1985: Radiometric observations of supercooled liquid water within a split front over the Sierra Nevada. *J. Climate and Applied Meteor.*, **24**, 1258–1261.

Heggli, M. F., R. M. Rauber, and J. B. Snider, 1987: Field evaluation of a dual-channel microwave radiometer designed for measurements of integrated water vapor and cloud liquid water in the atmosphere. *J. Atmos. Sci.*, **4**, 204–213.

Herzburg, G., 1950: *Molecular Spectra and Molecular Structure, I. Spectra of Diatomic Molecules.* D. Van Nostrand Co., Princeton, New Jersey.

Hogg, D. C., F. O. Guiraud, J. B. Snider, M. T. Decker, and E. R. Westwater, 1983: A steerable dual-channel microwave radiometer for measurement of water vapor and liquid water in the troposphere. *J. Applied Meteor.*, **22**, 789–806.

Hollinger, J., R. Lo, G. Poe, R. Savage, and J. Peirce, 1987: *Special Sensor Microwave/Imager user's guide.* Naval Research Laboratory, Washington, D. C., 120 pp.

Holton, J. R., 1979: *An Introduction to Dynamic Meteorology.* Academic Press, New York, 391 pp.

Important Farmlands of Colorado., 1980: USDA-Soil Conservation Service and CSU Experiment Station.

International Association of Meteorology and Atmospheric Physics (IAMAP) Radiation Commission, 1978: Terminology and units of radiation quantities and measurements, Boulder, Colorado, 17 pp.

Irrigated Acres: Kansas, 1986: USDA-Soil Conservation Service.

Jones, A. S., D. W. Hillger, J. F. W. Purdom, and T. H. Vonder Haar, 1988: Enhanced image products by limb-correction and smoothing of VAS radiance measurements. *Preprint Volume, Third Conference on Satellite Meteorology and Oceanography*, 31 January - 5 February, Anaheim, California (AMS), 105–108.

Kakar, R. K., 1983: Retrieval of clear sky moisture profiles using the 183 GHz water vapor line. *J. Climate and Applied Meteor.*, **22**, 1282–1289.

Kessinger, C. J. (editor), 1987: Operations plan for the Convection Initiation and Downburst Experiment (CINDE) near Denver, Colorado 22 June to 7 August, 1987. 154 pp.

Kessinger, C. J. (editor), 1988: Operation and Data Summary for the Convection Initiation and Downburst Experiment (CINDE) near Denver, Colorado 22 June to 7 August, 1987. 131 pp.

Kidder, S. Q., 1979: Determination of tropical cyclone surface pressure and winds from satellite microwave data. Atmos. Sci. Paper 307, Colorado State University, Fort Collins, Colorado, 87 pp.

Kummerow, C., and J. A. Weinman, 1988: Determining microwave brightness temperatures from precipitating horizontally finite and vertically structured clouds. *J. Geophysical Res.*, **93**, 3720–3728.

Liebe, H. J., G. G. Gimmestad, and J. D. Hopponen, 1977: Atmospheric oxygen microwave spectrum — experiment versus theory. *IEEE Trans. Antennas Propag.*, **AP-25**, 327–355.

Liebe, H. J., and G. G. Gimmestad, 1978: Calculation of clear air EHF refractivity. *Radio Sci.*, **13**, 245–251.

Liebe, H. J., 1981: Modeling attenuation and phase of radio waves in air at frequencies below 1000 GHz. *Radio Sci.*, **16**, 1183–1199.

Liebe, H. J., 1985: An updated model for millimeter wave propagation in moist air. *Radio Sci.*, **20**, 1069–1089.

Liou, K., and A. D. Duff, 1979: Atmospheric liquid water content derived from parameterization of Nimbus 6 Scanning Microwave Spectrometer data. *J. Applied Meteor.*, **18**, 99–103.

Liou, K., 1980: *An Introduction to Atmospheric Radiation.* Academic Press, Inc., Orlando, Florida, 392 pp.

Lovejoy, S., D. Schertzer, and A. A. Tsonis, 1987: Functional box-counting and multiple elliptical dimensions in rain. *Science*, **235**, 1036–1038.

Lovejoy, S., and D. Schertzer, 1988: Meeting Reports: Scaling, fractals, and nonlinear variability in geophysics. *Eos*, **69**, 143–145.

Marshall, J. S., and W. M. Palmer, 1948: The distribution of raindrops with size. *J. Meteor.*, **5**, 165–166.

McFarland, M. J., P. H. Harder III, G. D. Wilke, and G. L. Huebner, Jr., 1984: Crop moisture estimation over the southern Great Plains with dual polarization 1.66 centimeter passive microwave data from Nimbus 7. Final Rep. RSC-4854. Remote Sensing Center, Texas A&M University, 142 pp.

McMillin, L. M., and H. E. Fleming, 1976: Atmospheric transmittance of an absorbing gas: a computationally fast and accurate transmittance model for absorbing gases with constant mixing ratios in inhomogeneous atmospheres. *Applied Optics*, **15**, 358–363.

Meeks, M. L., and A. E. Lilley, 1963: The microwave spectrum of oxygen in the earth's atmosphere. *J. Geophys. Res.*, **68**, 1683–1703.

Mie, G., 1908: Beitrage zur optik truber median, speziell kolloidaler metallosungen. *Annalen der Physik*, **25**, 377–445.

Montgomery, H. E., and L. W. Uccellini (editors), 1985: VAS Demonstration: (VISSR Atmospheric Sounder) Description and Final Report. NASA Ref. Publication 1151, (NTIS Ref: 86N13867), 170 pp.

NASA, 1987: High-resolution multifrequency microwave radiometer (HMMR) earth observing system (EOS) instrument panel report. **IIe**, 59 pp.

Newton, R. W., 1977: Microwave remote sensing and its application to soil moisture detection. *Tech. Rep. RSC-81*, Remote Sensing Center, Texas A&M University, College Station, 500 pp.

Newton, R. W., Q. R. Black, S. Makanvand, A. J. Blanchard, and B. R. Jean, 1982: Soil moisture information and thermal microwave emission. *IEEE Trans. Geosci. Remote Sensing*, **GE-20**, 275–281.

Njoku, E. G., 1980: Antenna pattern correction procedure for the scanning multichannel microwave radiometer (SMMR). *Boundary-Layer Meteor.*, **18**, 79–98.

Njoku, E. G., 1982: Microwave remote sensing of the earth from space – a review. *Proceedings of the IEEE*, **70**, 728–750.

Olson, W. S., 1986: Model-based retrieval of tropical cyclone rainfall rates using the NIMBUS-7 SMMR. *Preprint Volume, Second Conference on Satellite Meteorology and Remote Sensing Applications*, 13 - 16 May, Williamsburg, Virginia (AMS), 438–443.

Owe, M., A. Chang, and R. E. Golus, 1988: Estimating surface soil moisture from satellite microwave measurements and a satellite derived vegetation index. *Remote Sens. Environment*, **24**, 331–345.

Peake, W. H., 1959: Interaction of electromagnetic waves with some natural surfaces. *IRE Trans.*, **AP-7**, 5342.

Perry, J., and A. Straiton, 1973: Revision of the "dielectric constant" of ice in the millimeter-wave spectrum. *J. Applied Phys.*, **44**, 5180.

Prabhakara, C., H. D. Chang, and A. T. C. Chang, 1982: Remote sensing of precipitable water over the oceans from Nimbus 7 microwave measurements. *J. Applied Meteor.*, **21**, 59-68.

Prabhakara, C., I. Wang, A. T. C. Chang, and P. Gloersen, 1983: A statistical examination of Nimbus-7 SMMR data and remote sensing of sea surface temperature, liquid water content in the atmosphere and surface wind speed. *J. Climate and Applied Meteor.*, **22**, 2023–2037.

Prabhakara, C., D. A. Short, and B. E. Vollmer, 1985: El Niño and atmospheric water vapor: observations from Nimbus 7 SMMR. *J. Climate and Applied Meteor.*, **24**, 1311–1324.

Prabhakara, C., D. A. Short, W. Wiscombe, R. S.Fraser, and B. E. Vollmer 1986: Rainfall over oceans inferred from the Nimbus 7 SMMR: Application to 1982-83 El Niño. *J. Climate and Applied Meteor.*, **25**, 1464–1474.

Pruppacher, H. R., and J. D. Klett, 1980: *Microphysics of Clouds and Precipitation*. D. Reidel Publishing Co., Dordrecht, Holland, 714 pp.

Rauber, R. M., D. Feng, L. O. Grant, and J. B. Snider. 1986: The characteristics and distribution of cloud liquid water over the mountains of northern Colorado during wintertime storms. Part I: Temporal variations. *J. Climate and Applied Meteor.*, **25**, 468–488.

Rauber, R. M., and L. O. Grant, 1986: The characteristics and distribution of cloud water over the mountains of northern Colorado during wintertime storms. Part II: Spatial distribution and microphysical characteristics. *J. Climate and Applied Meteor.*, **25**, 489–504.

Ray, P. S., 1972: Broadband complex refractive indices of ice and water. *Applied Optics*, **11**, 1836–1843.

Reitz, J. R., F. J. Milford, and R. W. Christy, 1979: *Foundations of Electromagnetic Theory*, Addison-Wesley Publishing Co., 534 pp.

Rodgers, R. R., 1979: *A Short Course in Cloud Physics*. Pergamon Press, Great Britain, 235 pp.

Rosenkranz, P. W., 1975: Shape of the 5 mm oxygen band in the atmosphere. *IEEE Trans. Antennas Propag.*, **AP-23**, 498–506.

Schmugge, T. J., T. J. Jackson, and H. L. McKim, 1980: Survey of methods for soil moisture determination. *Water Resources Res.*, **16**, 961–979.

Schmugge, T. J., and B. J. Choudhury, 1981: A comparison of radiative transfer models for predicting the microwave emission from soils. *Radio Sci.*, **16**, 927–938.

Schmugge, T. J., 1983: Remote sensing of soil moisture: recent advances. *IEEE Trans. Geosci. and Remote Sensing*, **GE-21**, 336–344.

Schmugge, T. J., 1985: Remote Sensing of soil moisture. *Hydrological Forecasting*, M. G. Anderson and T. P. Burt, Eds., Wiley, New York.

Segal, M., R. Avissar, M. C. McMcumber, R. A. Pielke, 1988a: Evaluation of vegetation effects on the generation and modification of mesoscale circulations. *J. Atmos. Sci.*, (In press).

Segal, M., W. E. Schreiber, G. Kallos, J. R. Garratt, A. Rodi, J. Weaver, and R. A. Pielke, 1988: The impact of crop areas in northeast Colorado on mid-summer mesoscale thermal circulations. *submitted to Mon. Wea. Rev.*

Shih, S. F., and E. Chen, 1984: On the use of GOES thermal data to study effects of land use on diurnal temperature fluctuation. *J. Climate and Applied Meteor.*, **23**, 426–433.

Simpson, J., R. F. Adler, and G. R. North, 1988: A proposed tropical rainfall measuring mission (TRMM) satellite. *Bull. Amer. Meteor. Soc.*, **69**, 278–295.

Slobin, S. D., 1982: Microwave noise temperature and attenuation of clouds: Statistics of these effects at various sites in the United States, Alaska, and Hawaii. *Radio Sci.*, **17**, 1443–1454.

Snider, J. B., F. O. Guiraud, and D. C. Hogg, 1980a: Comparison of cloud liquid content measured by two independent ground-based systems. *J. Applied Meteor.*, **19**, 577–579.

Snider, J. B., J. M. Burdick, and D. C. Hogg, 1980b: Cloud liquid measurement with a ground-based microwave instrument. *Radio Sci.*, **15**, 683–693.

Spencer, R. D., W. S. Olson, W. Rongzhang, D. W. Martin, J. A. Weinman, and D. A. Santek, 1983: Heavy thunderstorms observed over land by the NIMBUS 7 Scanning Multichannel Microwave Radiometer. *J. Climate and Applied Meteor.*, **22**, 1041–1046.

Spencer, R. D., 1986: A satellite passive 37-GHz scattering-based method for measuring oceanic rain rates. *J. Climate and Applied Meteor.*, **25**, 754–766.

Spencer, R. D., H. M. Goodman, and R. E. Hood, 1988: Precipitation retrieval over land and ocean with the SSM/I, Part 1: identification and characteristics of the scattering signal. *submitted to J. Atmos. and Oceanic Tech.*

Staelin, D. H., K. F. Kunzi, R. L. Pettyjohn, K. L. Poon, R. W. Wilcox, and J. W. Waters, 1976: Remote sensing of atmospheric water vapor and liquid water with the Nimbus 5 Microwave Spectrometer. *J. Applied Meteor.*, **15**, 1204–1214.

Stephens, G. L., 1980: Radiative properties of cirrus clouds in the infrared region. *J. Atmos. Sci.*, **37**, 435–446.

Theon, J. S., 1988: The Tropical Rainfall Measuring Mission (TRMM). *Preprint Volume, Third Conference on Satellite Meteorology and Oceanography*, 31 January - 5 February, Anaheim, California (AMS), 287–289.

Tsang, L., J. A. Kong, E. Njoku, D. H. Staelin, and J. W. Waters, 1977: Theory for microwave thermal emission from a layer of cloud or rain. *IEEE Trans. Antennas and Propag.*, **AP-25**, 650–657.

Ulaby, F. T., R. K. Moore, and A. K. Fung, 1981: *Microwave Remote Sensing Active and Passive, Vol. I Microwave Remote Sensing Fundamentals and Radiometry.* Addison-Wesley Publishing Co., Reading, Mass., 456 pp.

Ulaby, F. T., R. K. Moore, and A. K. Fung, 1986: *Microwave Remote Sensing Active and Passive, Vol. III From Theory to Applications.* Addison-Wesley Publishing Co., Reading, Mass., 1097 pp.

Valley, S. L. Ed., 1965: *Handbook of Geophysics and Space Environment.* Office of Aerospace Research, USAF, Cambridge Res. Labs.

van de Hulst, H. C., 1957: *Light Scattering by Small Particles.* Wiley, 470 pp.

Van Vleck, J. H. 1947a: Absorption of microwaves by oxygen. *Phys. Rev.* **71**, 413–424.

Van Vleck, J. H. 1947b: Absorption of microwaves by water vapor. *Phys. Rev.* **71**, 425–433.

Vant, M. R., R. B. Gray, R. O. Ramseier, and V. Makios, 1974: Dielectric properties of fresh sea ice at 10 and 35 GHz. *J. Appl. Phys.*, **45**, 4712–4717.

Vonder Haar, T. H., W. E. Shenk, and D. W. Graul, 1986: Passive microwave radiometer experiment for GOES-NEXT. *Preprint Volume, Second Conference on Satellite Meteorology and Remote Sensing Applications*, 13 - 16 May, Williamsburg, Virginia (AMS), 514–518.

Wang, J. R., and T. J. Schmugge, 1980: An empirical model for the complex dielectric permittivity of soils as a function of water content. *IEEE Trans. Geosci. and Remote Sensing* **GE-18**, 288–295.

Warner, 1955: *Tellus*, **7**, 449.

Warren, S. G., 1984: Optical constants of ice from the ultraviolet to the microwave. *Applied Optics*, **23**, 1206–1225.

Waters, J. R., 1976: Absorption and emission by atmospheric gases. *Methods of Experimental Physics*, **12B**, M. L. Meeks, Ed., Academic Press, New York.

Weekly Weather and Crop Bulletin, 1987: **74**, Numbers 28-32. U.S. Department of Commerce, DOA, Washington, D.C.

Westwater, E. R., 1965: Ground-based passive probing using the microwave spectrum of oxygen. *Radio Sci.*, **69D**, 1201–1211.

Westwater, E. R., 1972: Microwave emission from clouds. *NOAA Tech. Rep. 219-WPL 18*, Boulder, Colorado, 43 pp.

Westwater, E. R., 1978: The accuracy of water vapor and cloud liquid determination by dual-frequency ground-based microwave radiometry. *Radio Sci.*, **13**, 677–685.

Wetzel, P. J., D. Atlas, and R. H. Woodward, 1984: Determining soil moisture from geosynchronous satellite infrared data: A feasibility study. *J. Climate and Applied Meteor.*, **23**, 375–391.

Wetzel, P. J., and R. H. Woodward, 1987: Soil moisture estimation using GOES-VISSR Infrared data: A case study with a simple statistical model. *J. Climate and Applied Meteor.*, **26**, 107–117.

Wilheit, T. T., A. T. C. Chang, M. S. V. Rao, E. B. Rodgers, and J. S. Theon, 1977: A satellite technique for quantitatively mapping rainfall rates over the oceans. *J. Appl. Meteor.*, **16**, 551–559.

Wilheit, T. T., 1978a: A review of applications of microwave radiometry to oceanography. *Boundary-Layer Meteor.*, **13**, 277–293.

Wilheit, T. T., 1978b: Radiative transfer in a plane stratified dielectric. *IEEE Trans. Geosci. Electron.*, **GE-16**, 138-143.

Wilheit, T. T., and A. T. C. Chang, 1980: An algorithm for retrieval of ocean surface and atmospheric parameters from the observations of the scanning multichannel microwave radiometer. *Radio Sci.*, **15**, 525–544.

Wilke, G. D., and M. J. McFarland, 1986: Correlations between Nimbus-7 Scanning Multichannel Microwave Radiometer data and an antecedent precipitation index. *J. Climate and Applied Meteor.*, **25**, 227–238.

Wu, M. C., 1988: Determination of cloud ice water content and geometrical thickness using microwave and infrared radiometric measurements. *J. Climate and Applied Meteor.*, **26**, 878–884.

Wu, R., and J. A. Weinman, 1984: Microwave radiances from precipitating clouds containing aspherical ice, combined phase, and liquid hydrometeors. *J. Geophysical Res.*, **89**, 7170–7178.

Yeh, H., and K. Liou, 1983: Remote sounding of cloud parameters from a combination of infrared and microwave channels. *J. Climate and Applied Meteor.*, **22**, 201–213.

Appendix A

THE LIEBE MILLIMETER-WAVE PROPAGATION MODEL (MPM)

The millimeter-wave Propagation Model (MPM) by Dr. Hans J. Liebe at the Institute for Telecommunication Sciences in Boulder, Colorado, is a limited line model which uses an 80 line data base and is valid for a frequency range of 1 - 1000 GHz. It was originally described in Liebe *et al.* (1977) and has been revised several times since (Liebe *et al.*, 1978; Liebe, 1981; Allen and Liebe, 1983; Liebe, 1985). Allen and Liebe (1983) provides a concise overview of the model and the line parameterizations used in the model. The version described in Liebe (1985) is the basis for the transmittance model used in this paper.

Several modifications were made to the Liebe MPM model for use in this study. The model was adjusted so that the vertical coordinate is pressure rather than height, and 40 discrete pressure levels are used in the vertical integration of the model. The vertical coordinate transformation, assuming hydrostatic equilibrium, is made by using the hypsometric equation (Holton, 1979),

$$\Delta Z \equiv \frac{R_d}{g} \int_{p_2}^{p_1} T_v \, d(\ln p), \tag{A.1}$$

where $R_d = 287\ \mathrm{J{\cdot}kg^{-1}{\cdot}K^{-1}}$ is the gas constant for dry air, $g = 9.81\ \mathrm{m{\cdot}s^{-2}}$ is the global average of gravity at mean sea level and T_v is virtual temperature which is used to account for moisture effects. The model output is in terms of attenuation, $\mathcal{A}$, in units of dB, which is converted to transmittance by,

$$\tau = \exp\left(\frac{-\mathcal{A}}{10 \log_{10} e}\right). \tag{A.2}$$

The transmittance model is designed to be easy to use. A fortran call statement with frequency and various meteorological profile arrays as the argument of the call is used which returns an array containing the integrated transmittances, $\tau(0, p_i)$, $(i = 1, 40)$, where p_i is one of the discrete pressure levels in the model.

The meteorological variables used as input in the algorithm are pressure, temperature, water vapor mixing ratio, and liquid water. For oxygen and water vapor absorption, the algorithm uses a modified Van Vleck-Weisskopf line shape developed by Rosenkranz (1975) which includes a line overlap correction parameter to fit observed measurements in moist air. Continuum absorption terms are necessary to correctly explain the attenuation in the window regions between the absorption lines. The dry air and water vapor continuum absorption becomes larger with increasing frequency. An uncertainty exists in predicting the continuum absorption since it is derived empirically by fitting experimental data (Waters, 1976). Cloud liquid water attenuation is calculated using the Rayleigh approximation of Mie scattering theory and is proportional to the liquid water content. The dielectric constant of water for the cloud water attenuation calculation is calculated with the Debye model as described by Chang and Wilheit (1979). The verification of the MPM is within the 4 percent experimental uncertainties of the observations (Liebe and Gimmestad, 1978).

Appendix B

SSM/I SURFACE EMITTANCE IMAGERY AND HISTOGRAMS

This appendix contains the retrieved composite surface emittances for channels 1-5 (19.35 GHz V,H; 22.235 GHz V; 37.0 GHz V,H) in image form and in histogram form for the case study area and time period. The composites are of cases 2, 3, 4, 6, and 8. No infrared data was available for case 1. Case 5 was not included due to a bias in the retrieved surface temperatures since the GOES data was taken approximately 2 hours later. Case 7 was completely overcast so no surface emittance retrieval was possible for that case. Figures B.1 through B.5 are the composite surface emittance histograms for SSM/I channels 1-5. Figures B.6 through B.10 are images of surface emittance for the case study area. The color table used represents the low surface emittance areas as dark and the higher surface emittance values as lighter shades of grey, where white represents a surface emittance of 1.0. Black colored areas are locations where cloud contamination was present throughout the composite time period and no surface emittance retrievals were possible.

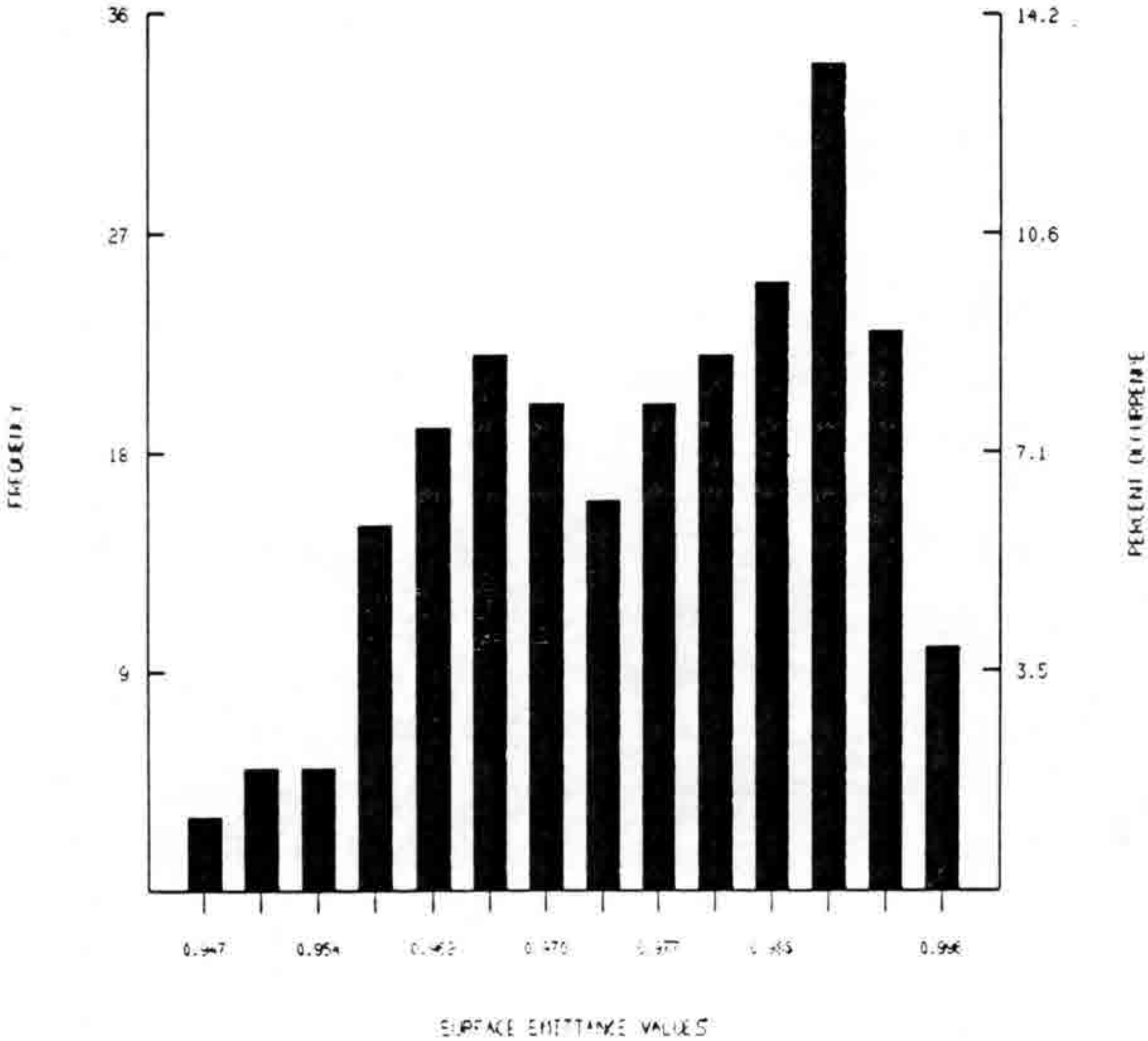

Figure B.1: Composite surface emittance values for SSM/I channel 1 (19.35 GHz vertical polarization).

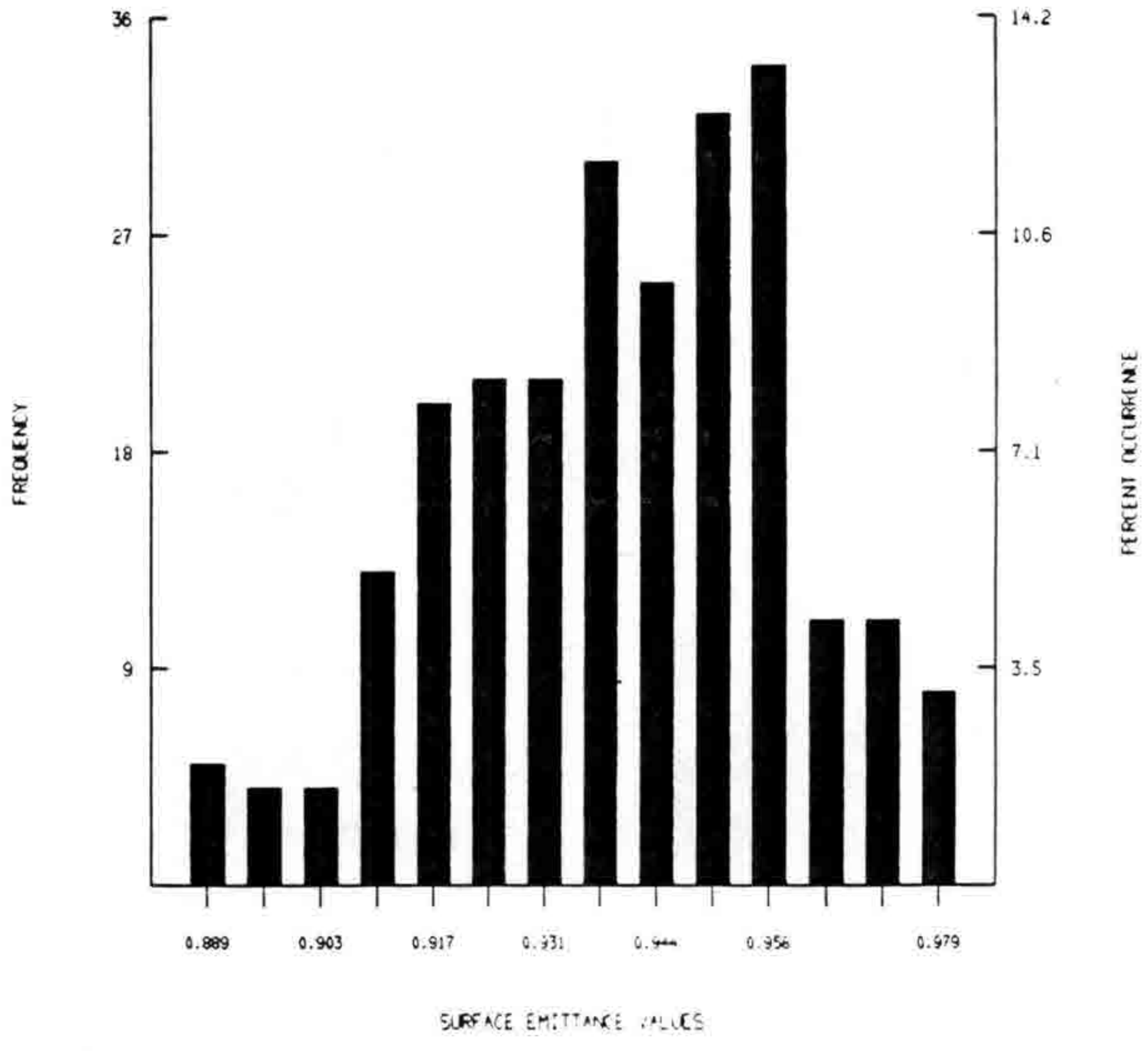

Figure B.2: Composite surface emittance values for SSM/I channel 2 (19.35 GHz horizontal polarization).

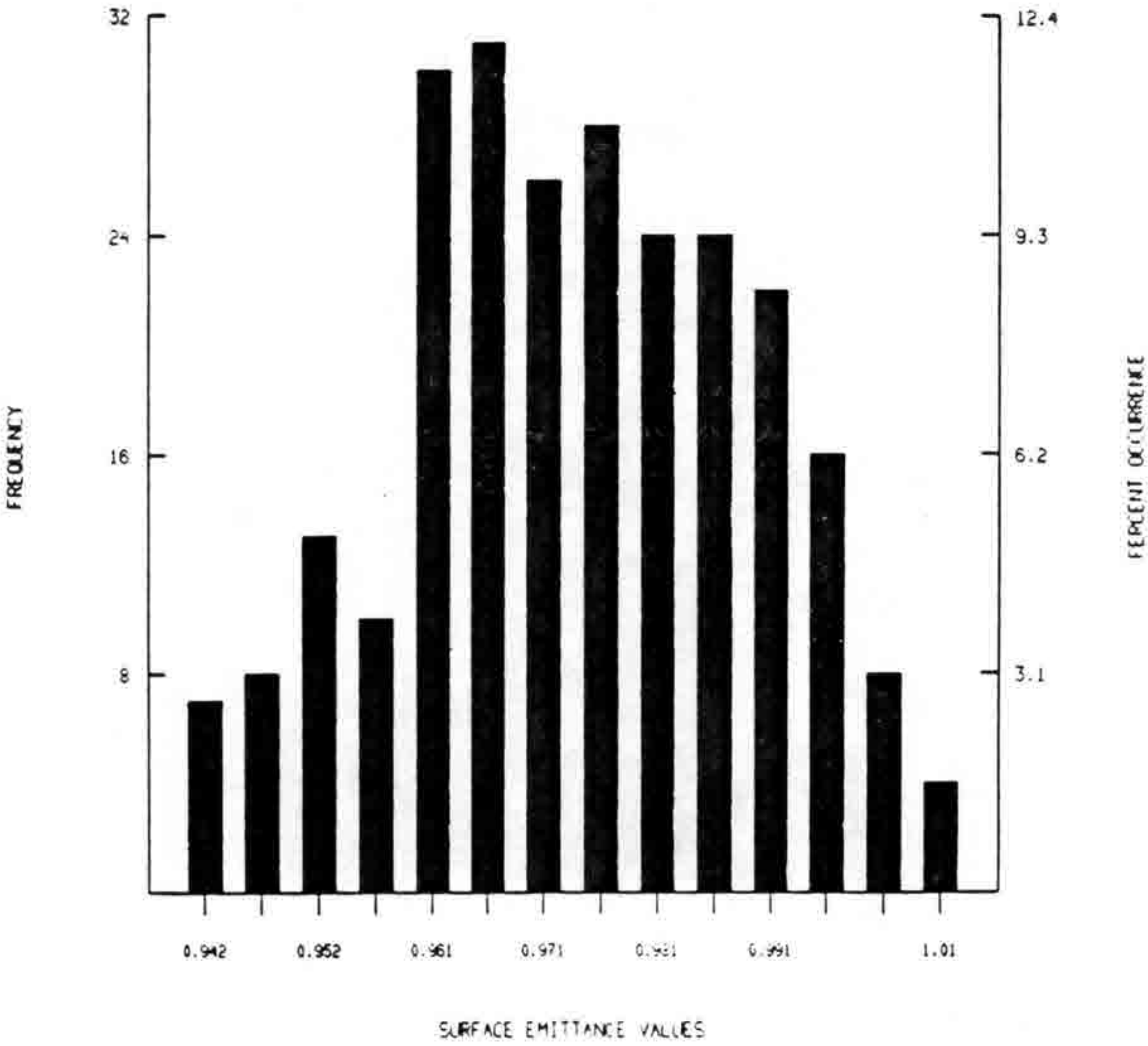

Figure B.3: Composite surface emittance values for SSM/I channel 3 (22.235 GHz vertical polarization).

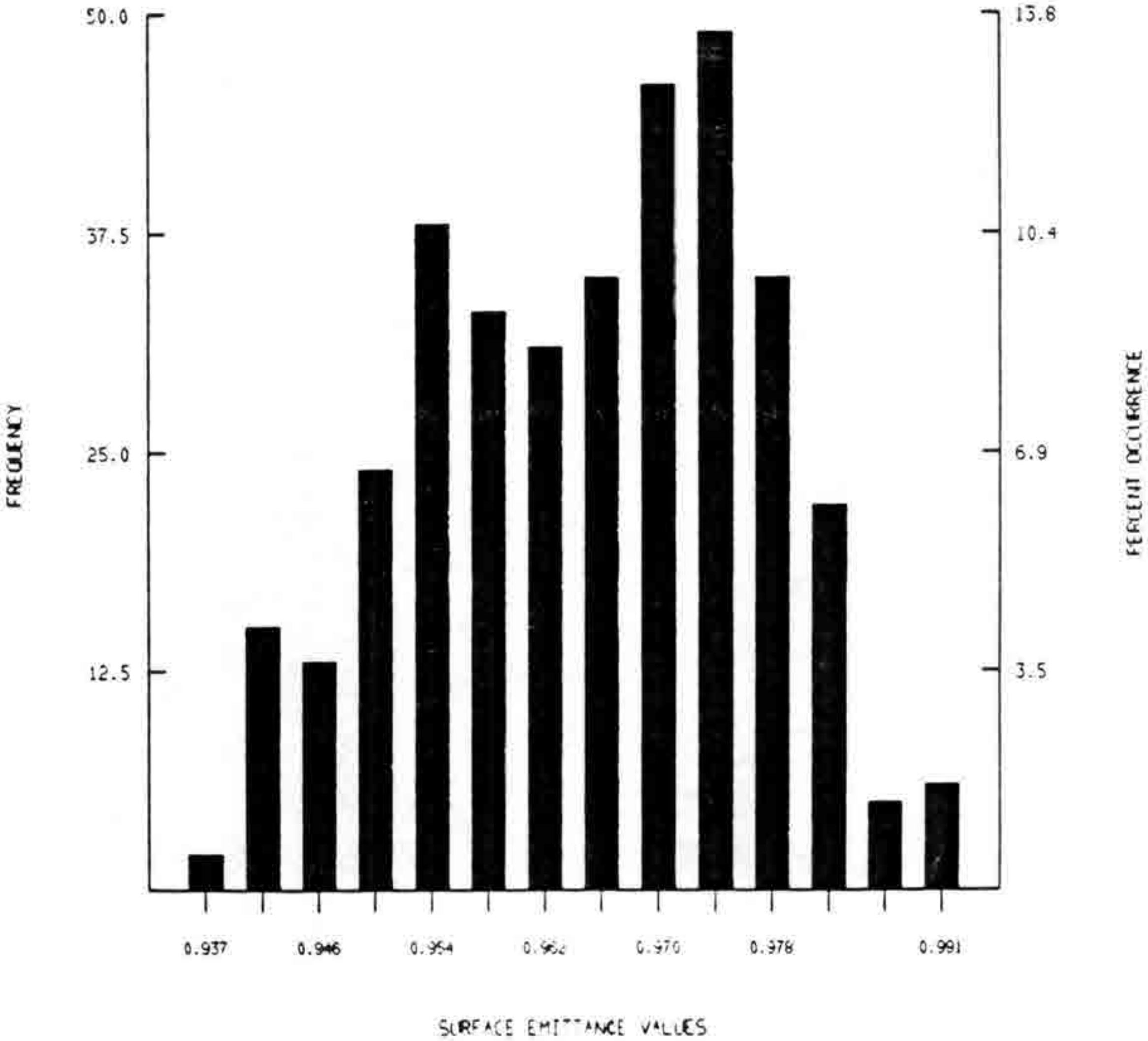

Figure B.4: Composite surface emittance values for SSM/I channel 4 (37.0 GHz vertical polarization).

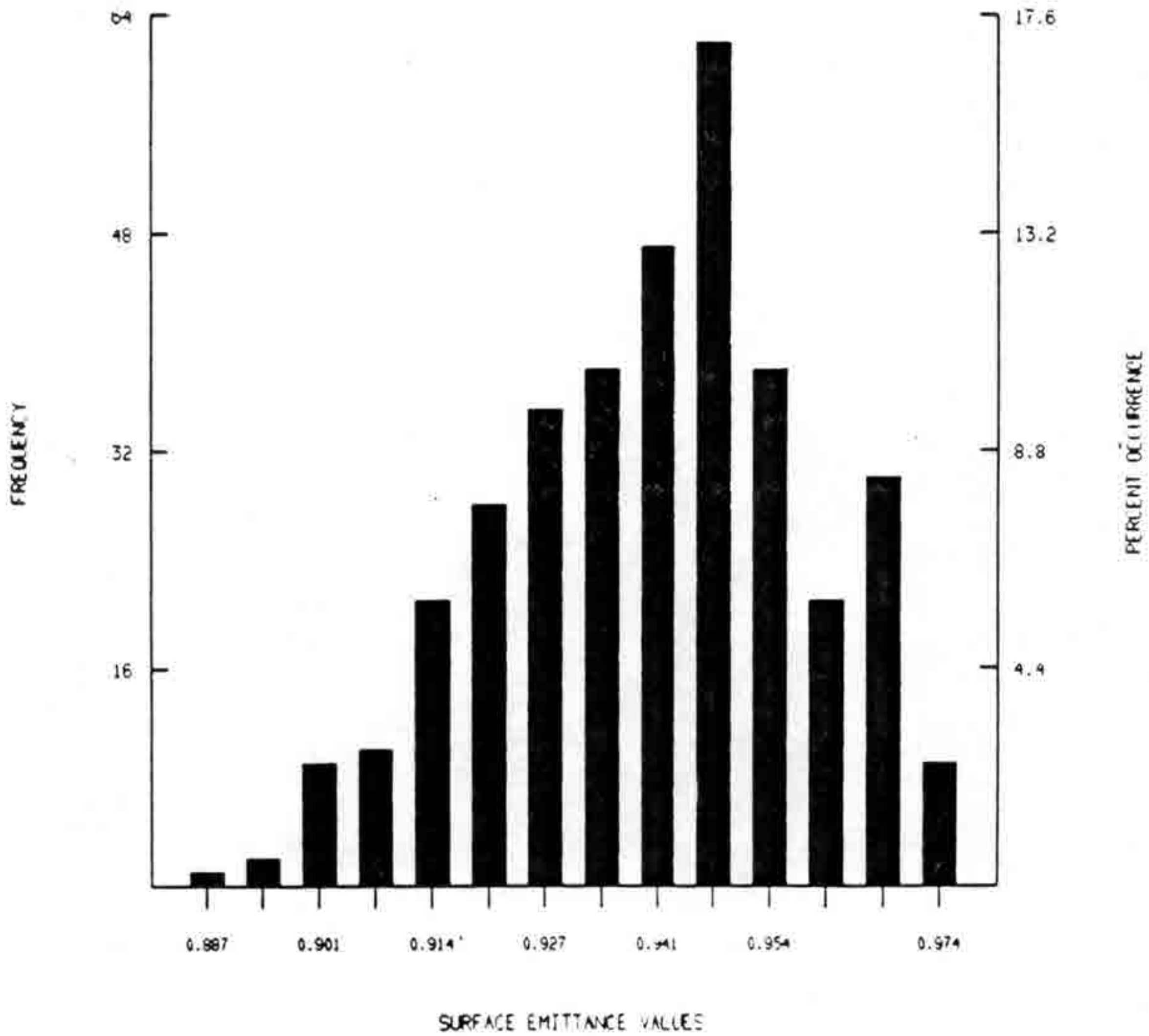

Figure B.5: Composite surface emittance values for SSM/I channel 5 (37.0 GHz horizontal polarization).

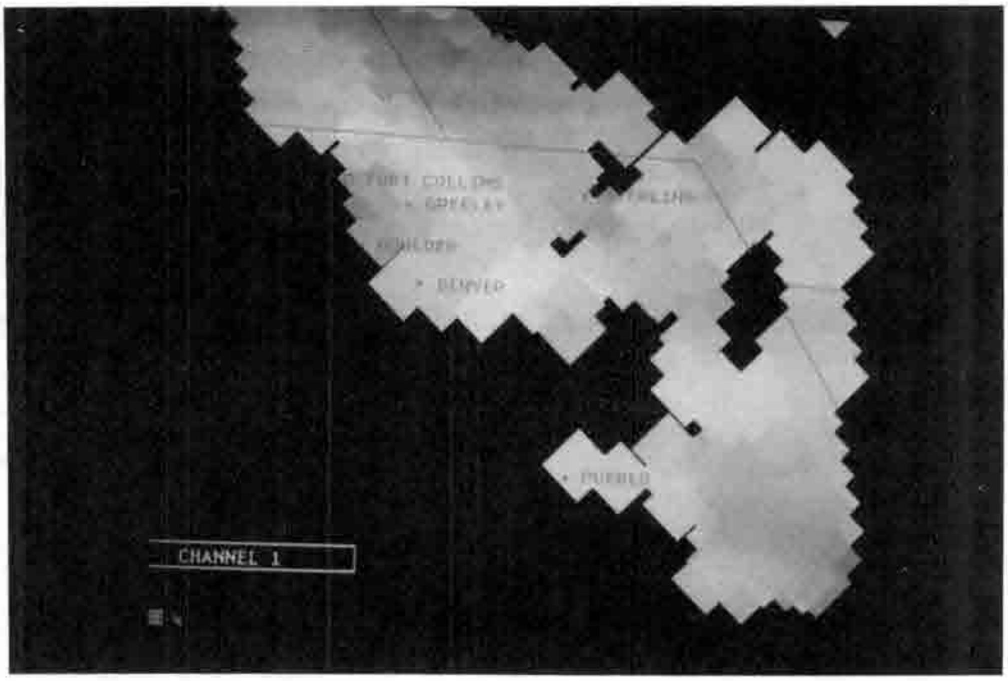

Figure B.6: Composite surface emittance imagery for SSM/I channel 1 (19.35 GHz vertical polarization).

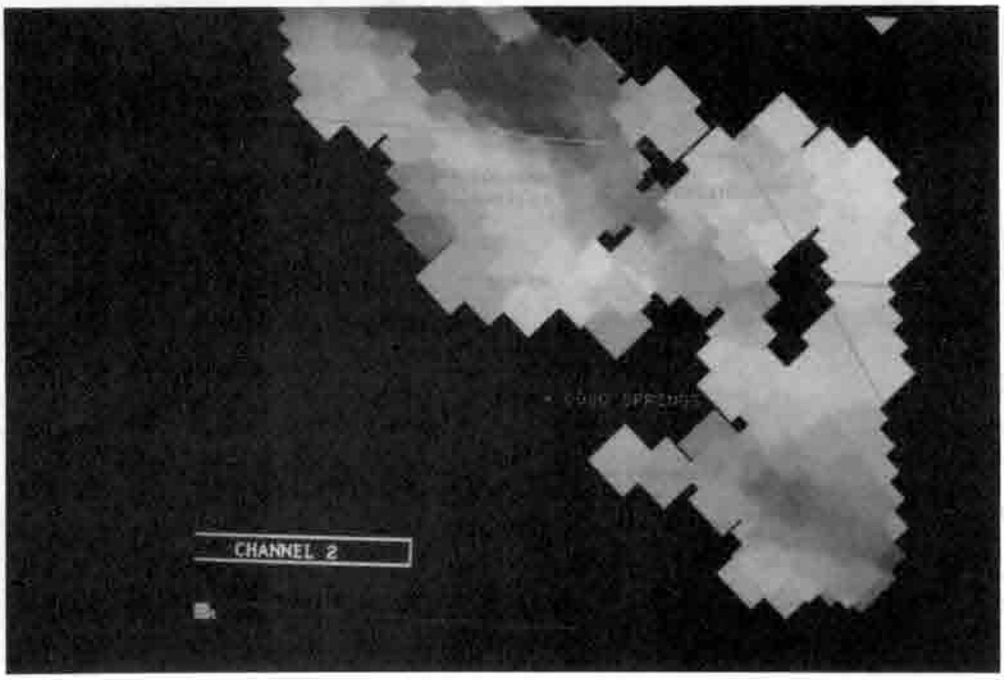

Figure B.7: Composite surface emittance imagery for SSM/I channel 2 (19.35 GHz horizontal polarization).

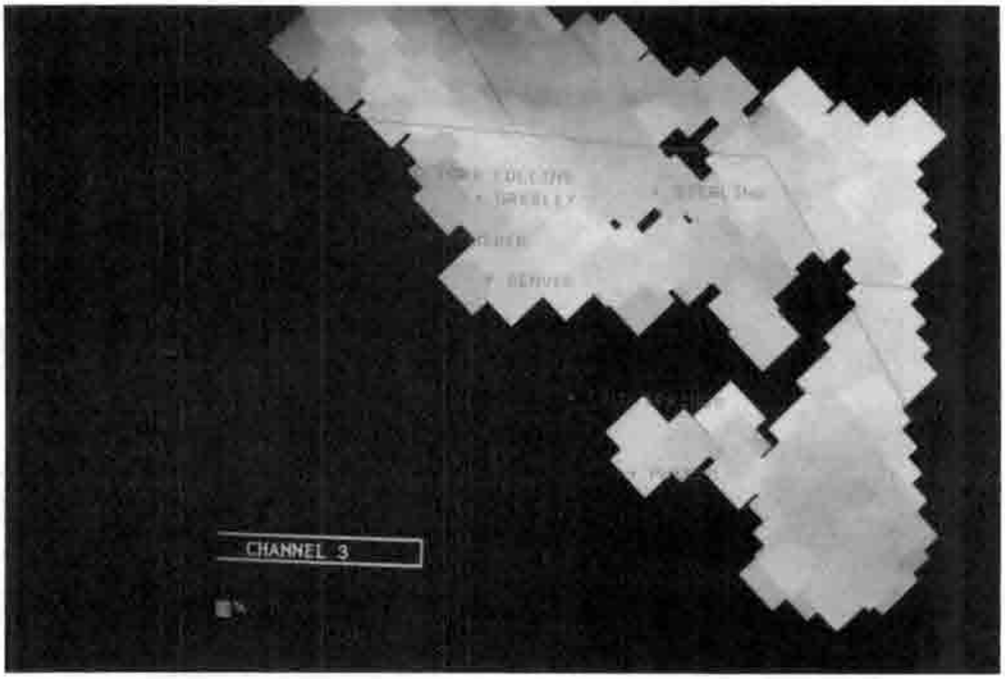

Figure B.8: Composite surface emittance imagery for SSM/I channel 3 (22.235 GHz vertical polarization).

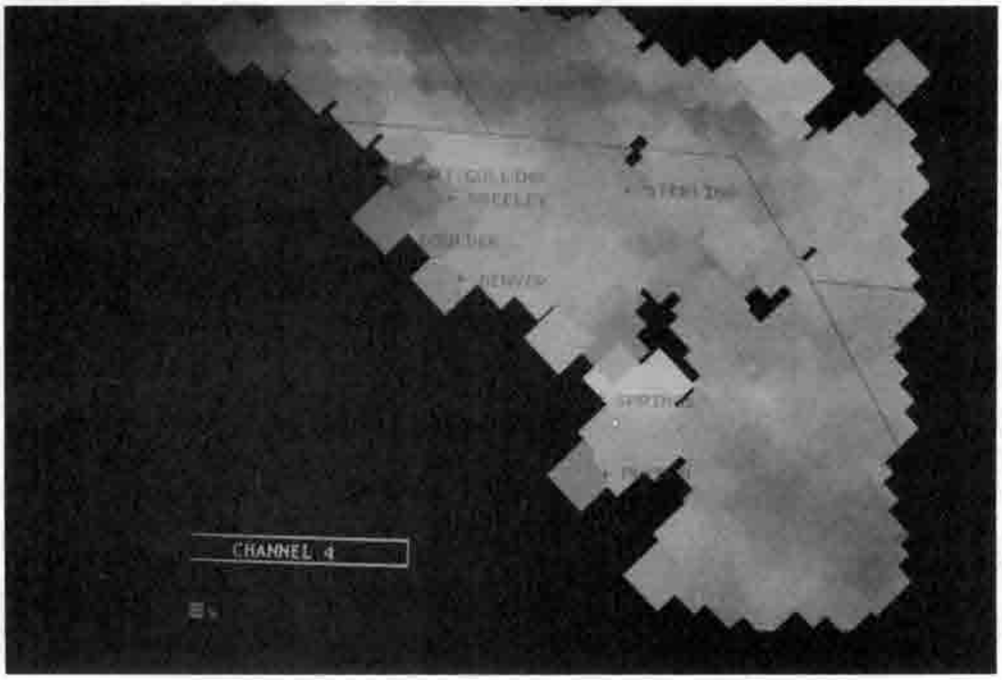

Figure B.9: Composite surface emittance imagery for SSM/I channel 4 (37.0 GHz vertical polarization).

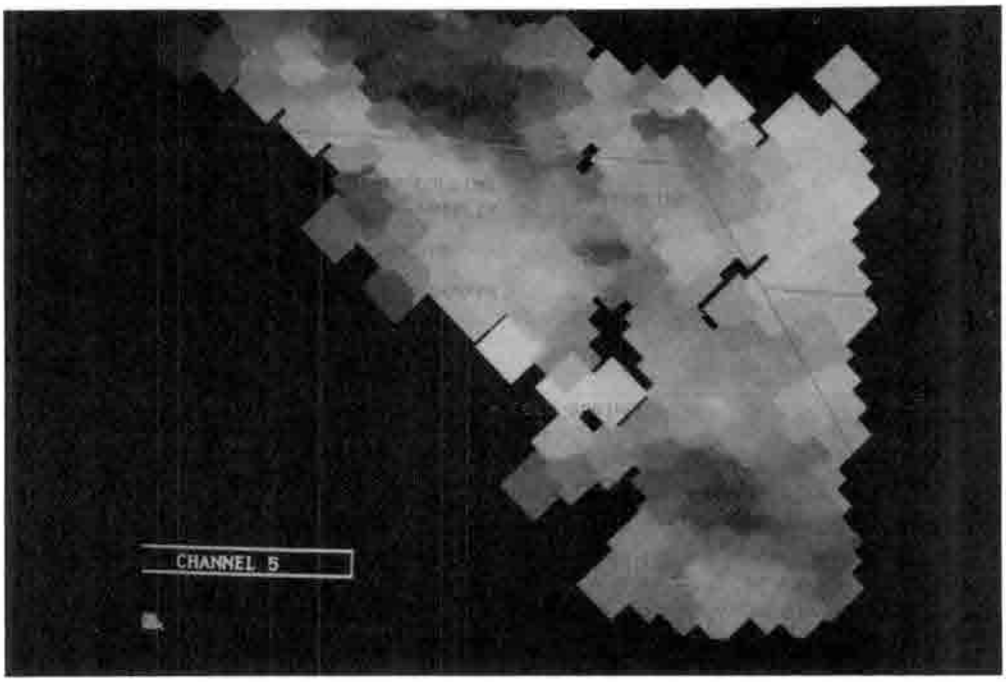

Figure B.10: Composite surface emittance imagery for SSM/I channel 5 (37.0 GHz horizontal polarization).

Appendix C

COMPARISON OF INTEGRATED CLOUD LIQUID WATER RETRIEVALS FROM CHANNEL 6 AND CHANNEL 7 FOR CASE 7

This appendix contains the scatter plots of the integrated cloud liquid water retrieval channel comparisons for case 7 (7 August 1245 UTC). Case 7 had more stratiform-like cloudiness which resulted in a slightly smaller cloud liquid water variability. This may be due to the physical aspects of the clouds or to the validity of the assumption of homogeneous cloud conditions within the microwave FOV. The original integrated cloud liquid water retrieval comparisons for three different height intervals are shown in Figures C.1 through C.3. Retrieval results with a 1.5 K brightness temperature correction applied to the vertical and horizontal polarizations at 85.5 GHz are shown in Figures C.4 through C.6.

This is page 139.
It is a right hand page.
Beginning here odd number
pages go back to right and
even number pages go back to
left.

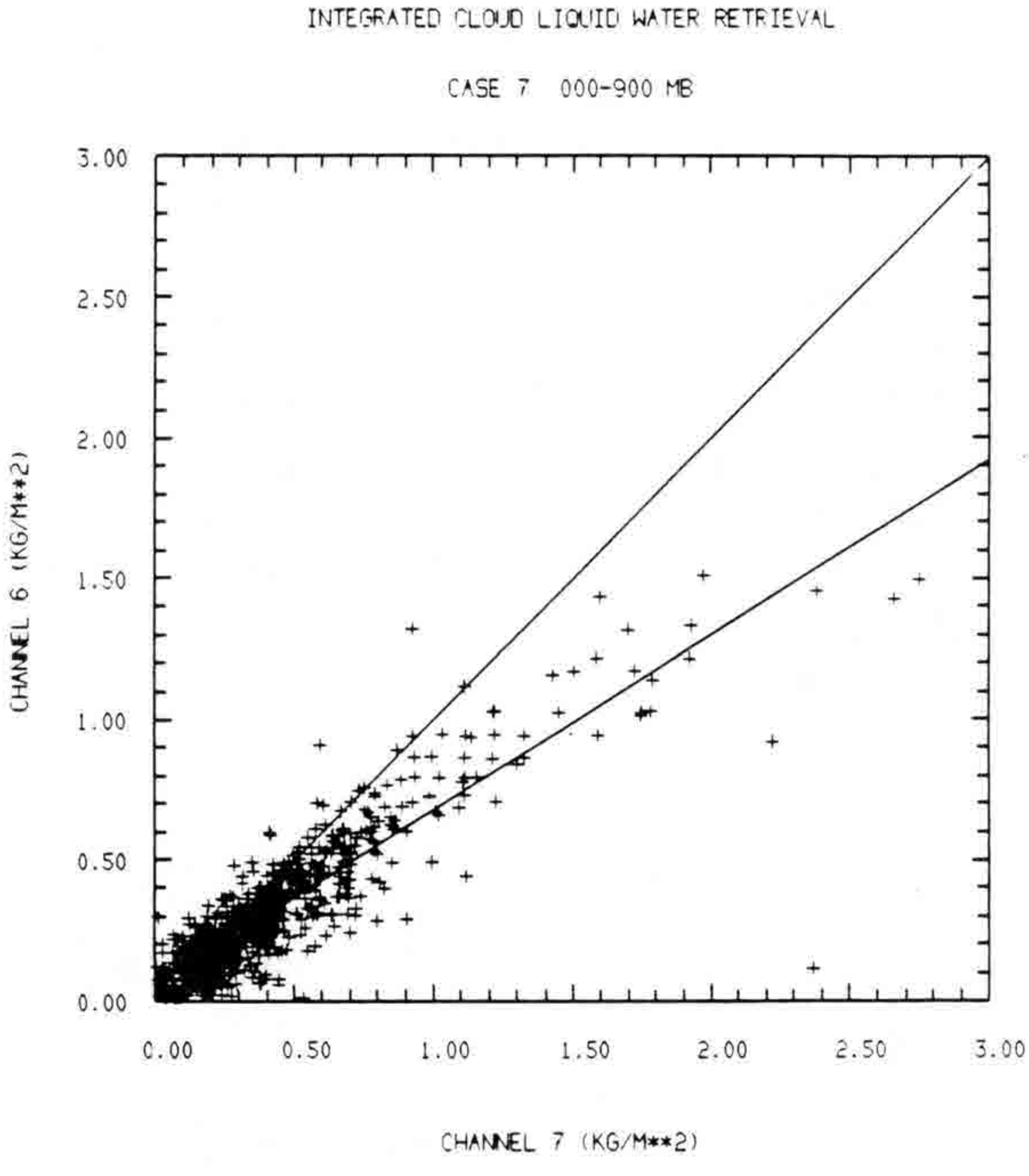

Figure C.1: Comparison of integrated cloud liquid water retrievals from channels 6 and 7 for case 7 ($p_{\rm top} < p_{\rm bot}$).

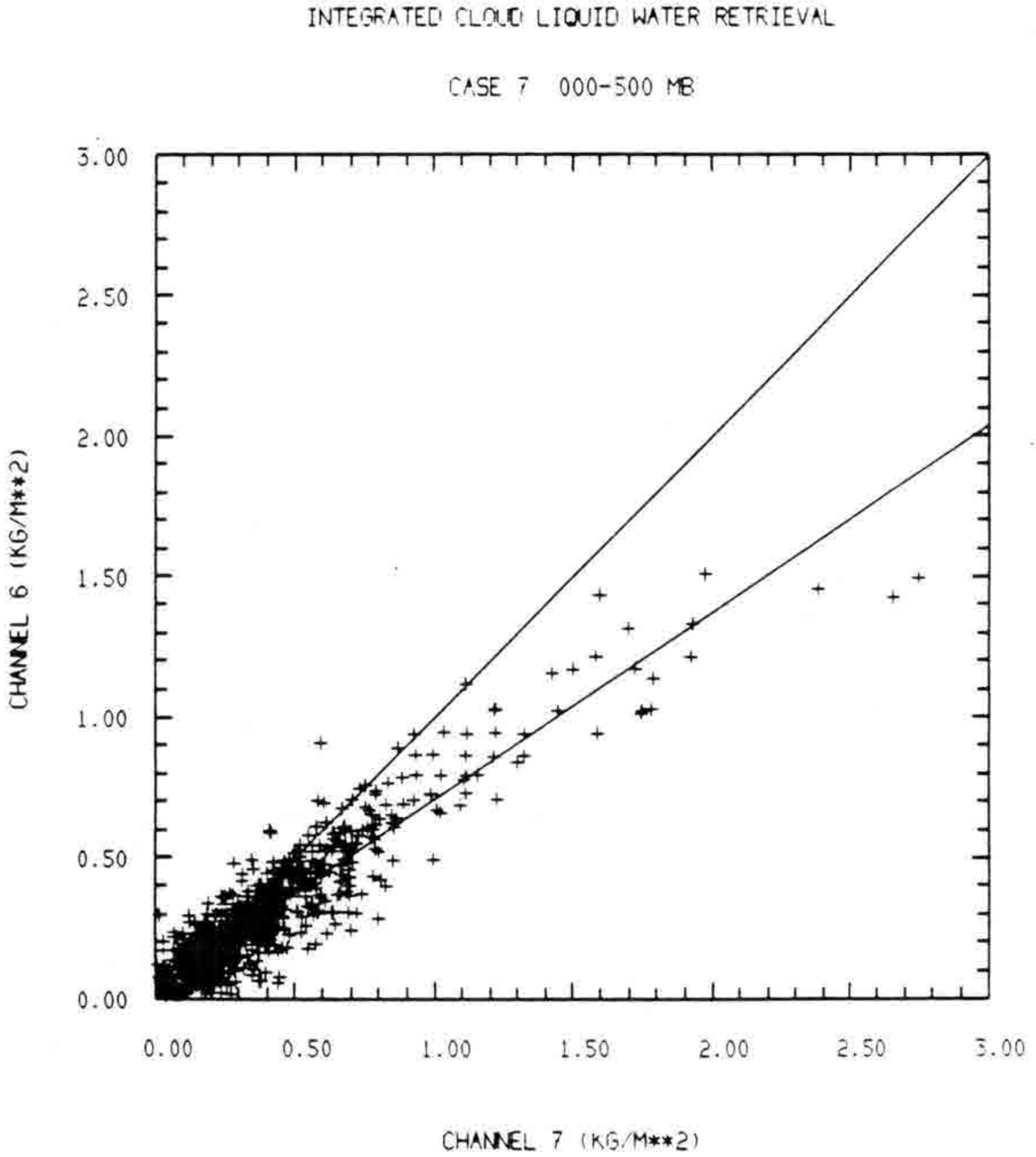

Figure C.2: comparison of integrated cloud liquid water retrievals from channels 6 and 7 for case 7 ($p_{\text{top}} < 500$ hPa).

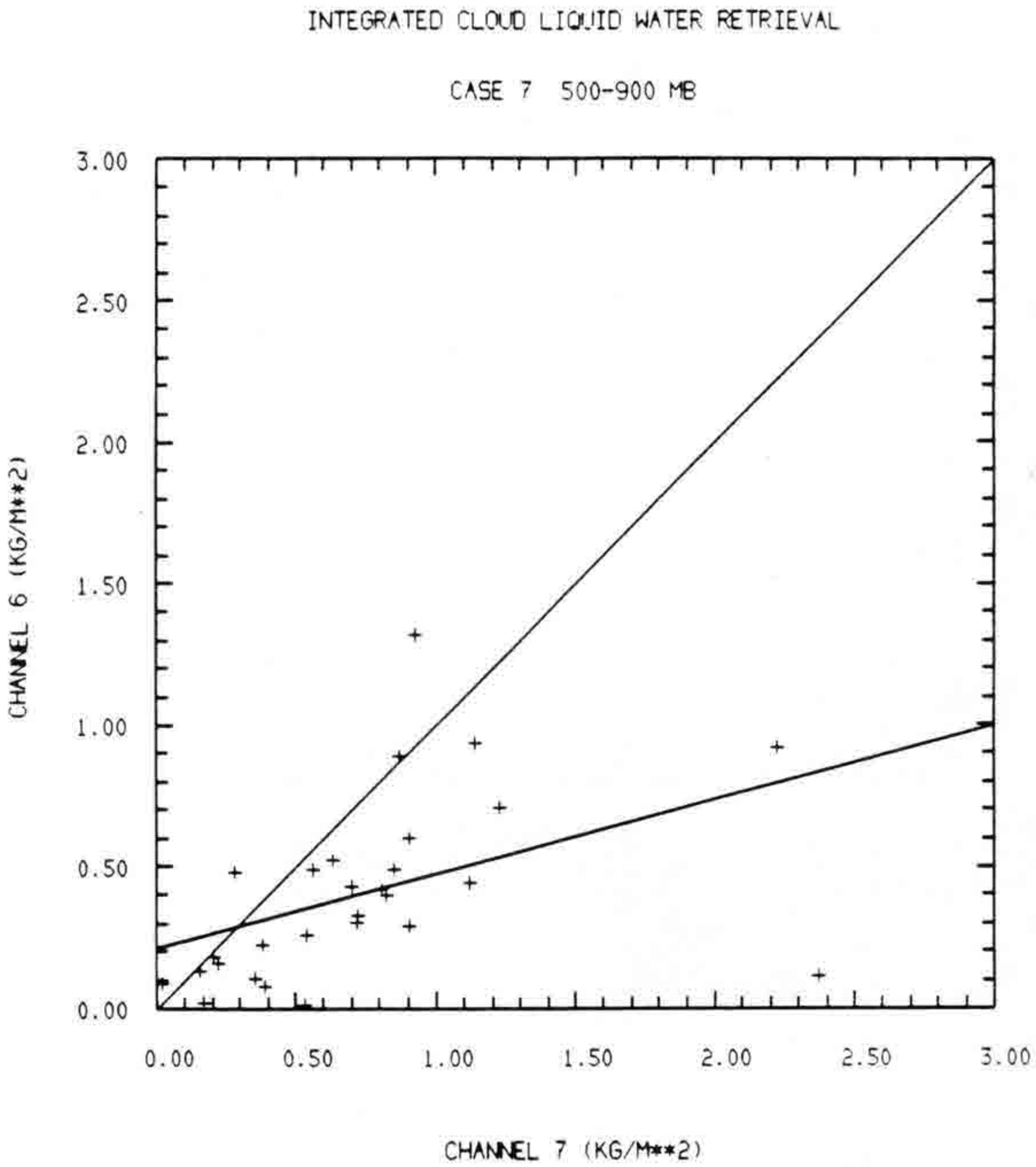

Figure C.3: comparison of integrated cloud liquid water retrievals from channels 6 and 7 for case 7 (500 hPa $< p_{\rm top} < p_{\rm bot}$).

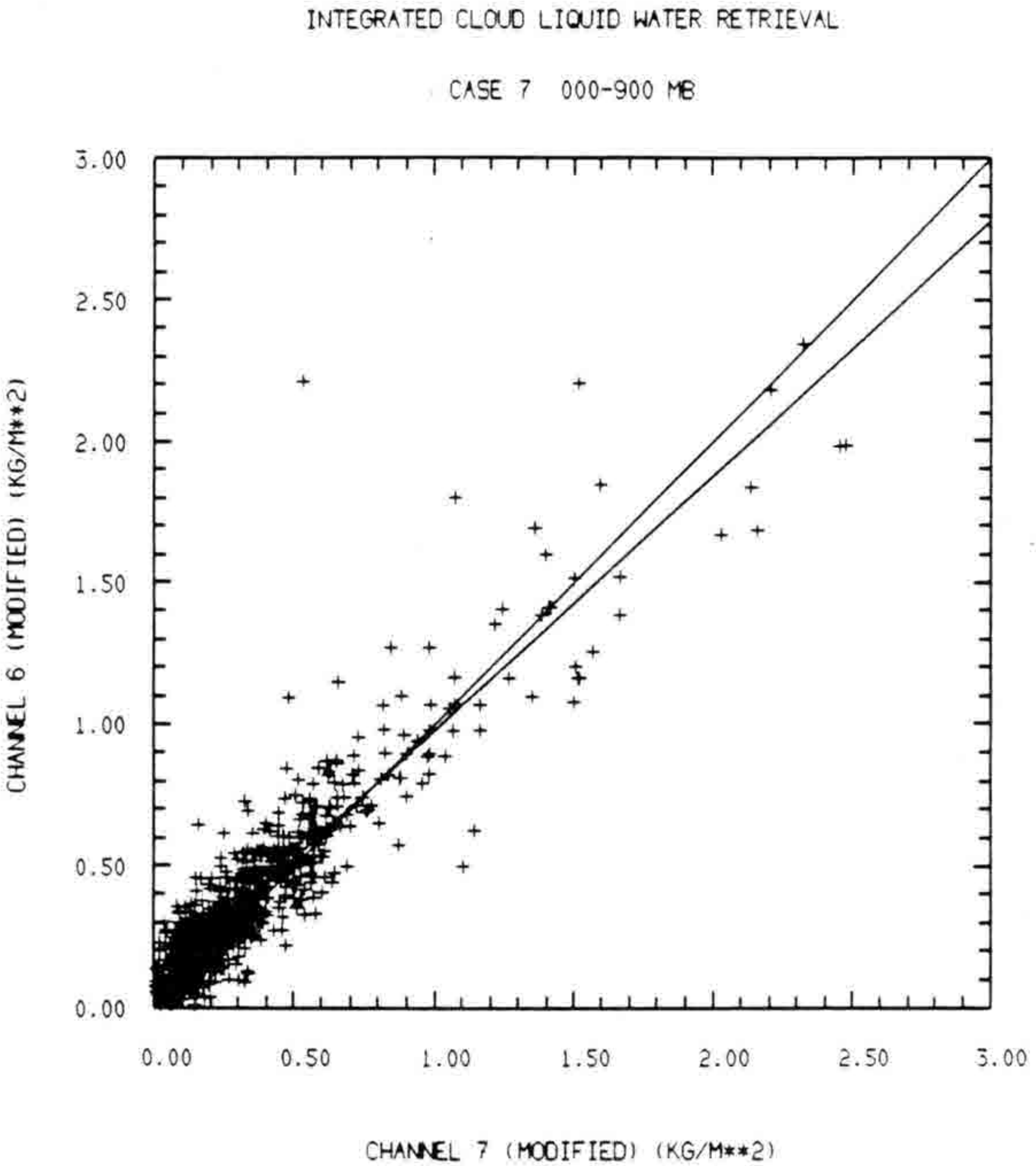

Figure C.4: Comparison of integrated cloud liquid water retrievals using channels 6 and 7 with bias correction for case 7 ($p_{\rm top} < p_{\rm bot}$).

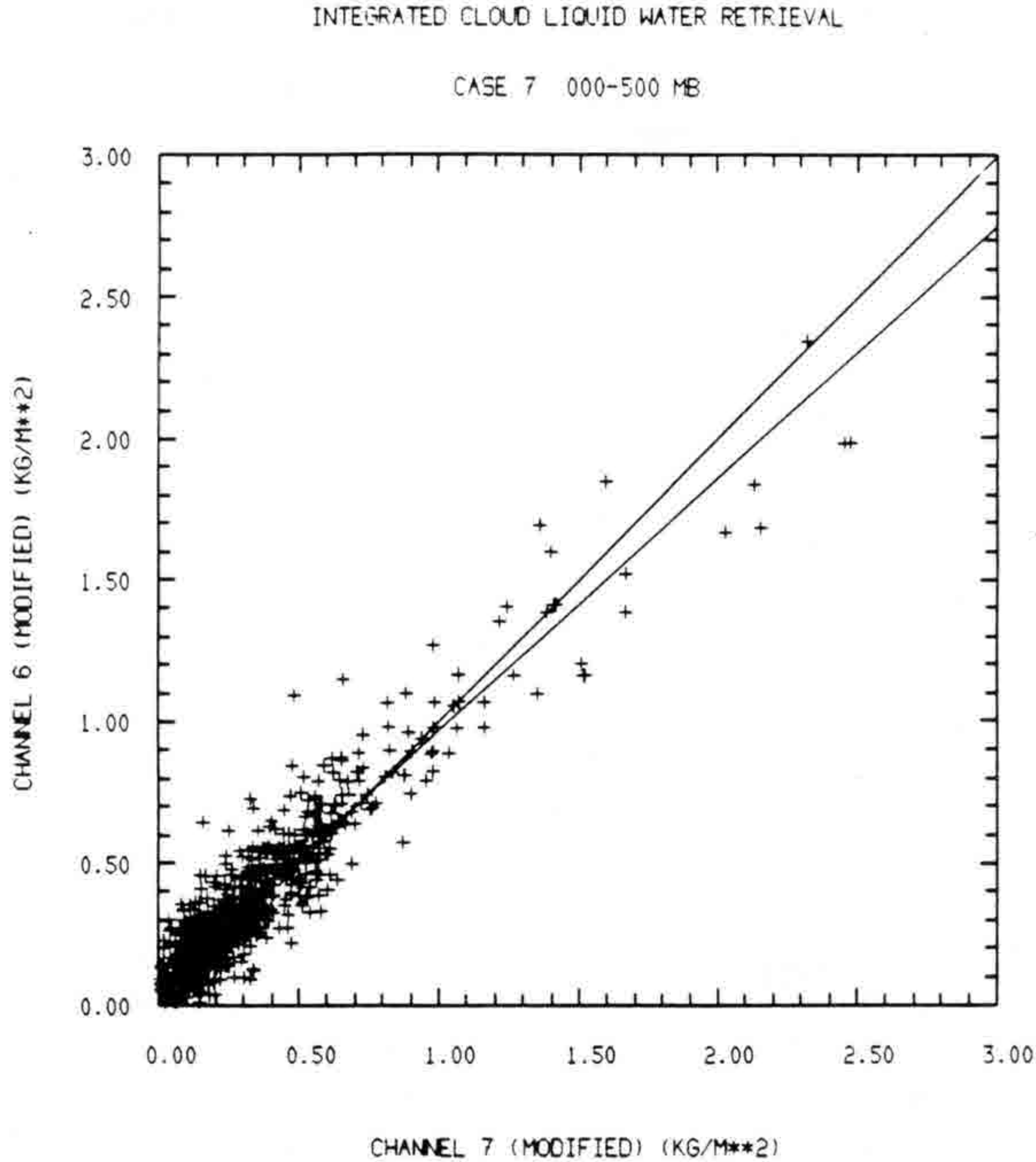

Figure C.5: Comparison of integrated cloud liquid water retrievals using channels 6 and 7 with bias correction for case 7 ($p_{\text{top}} < 500$ hPa).

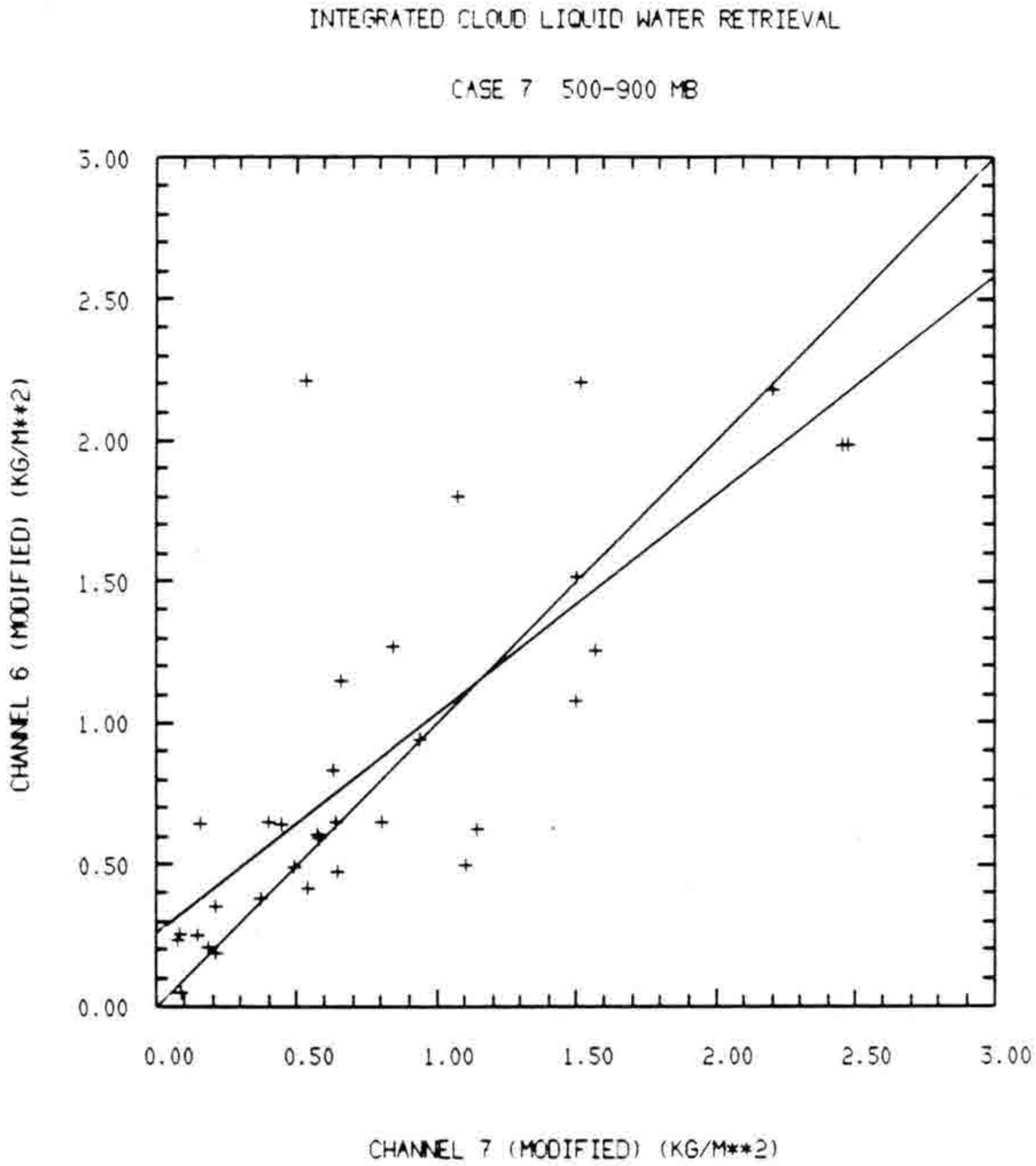

Figure C.6: Comparison of integrated cloud liquid water retrievals using channels 6 and 7 with bias correction for case 7 (500 hPa $< p_{\text{top}} < p_{\text{bot}}$).